Spring 2016

Detecting and Screening of the Prostate Cancer by Using an Optical Nanoporous Thin-Film Sensor

Salah Eldeen Mofleh Alzghoul

DETECTING AND SCREENING OF THE PROSTATE CANCER

BY USING AN OPTICAL NANOPOROUS

THIN-FILM SENSOR

by

Salah Eldeen Mofleh Alzghoul, B.S., M.S.

A Dissertation Presented in Partial Fulfillment
of the Requirements of the Degree
Doctor of Philosophy

COLLEGE OF ENGINEERING AND SCIENCE
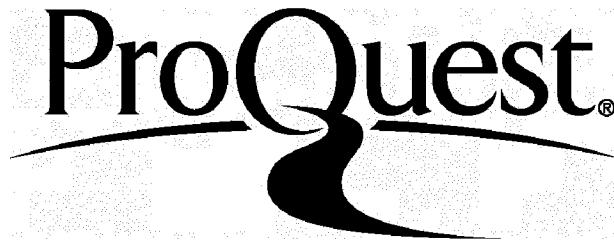LOUISIANA TECH UNIVERSITY

May 2016

ProQuest Number: 10301328

ProQuest 10301328

LOUISIANA TECH UNIVERSITY

THE GRADUATE SCHOOL

_____**MARCH 30, 2016**_____
Date

We hereby recommend that the dissertation prepared under our supervision by

Salah Eldeen Mofleh Alzghoul, B.S., M.S.

entitled   **Detecting and screening of the prostate cancer by using an optical**

nanoporous thin-film sensor.

be accepted in partial fulfillment of the requirements for the Degree of

Doctor of Philosophy in Engineering

Sandra Zivanovic
_____
Supervisor of Dissertation Research
_____
Head of Department
Biomedical Engineering
_____
Department

Recommendation concurred in:

S. Zivanovic for Long Que

Advisory Committee

Approved:
_____
Director of Graduate Studies

_____
Dean of the College

Approved:
_____
Dean of the Graduate School

ABSTRACT

Prostate cancer (PC) affects elderly men more than young men. The currently

used cancer biomarker, prostate-specific antigen (PSA), highly overestimates PC

population. Men with high PSA levels often have to go through unnecessary, but

physically painful, and expensive prosesses, such as prostate biopsies. Finding a prostate

cancer marker that is produced selectively by cancer, but not by normal prostate cells will

increase the reliability of PC test. In 2006, our collaborator (Dr. Girish Shah) discovered

a novel protein, referred as neuroendocrine marker (NEM), secreted only by malignant

prostate cells and released in blood circulation.

To examine whether the combined NEM-PSA test can improve the reliability for

early PC detection, we have developed a nanoporous thin film sensor that can reliably

detect PSA and NEM in patient samples. The thin film sensor is fabricated from

nanoporous anodic aluminum oxide and uses an optical Fabry-Perot intereferometric

technique. This optical sensor has been tested for several assay paradigms, including non-

specific binding, reliability, accuracy, precision, and sensitivity. The results demonstrate

that the optical nanoporous thin film sensor is reliable and extremely sensitive when used

with only 0.5 μl of patient serum (or even less) to measure levels of the PSA and NEM,

even in a non-cancer individual. When compared with the traditional ELISA test for

PSA, the nanosensor assay is several-fold more sensitive, and it elimnates the need for

labeled antigen, sample processing, complex equipment, and highly experienced

individuals. These benefits, along with the low cost, should make the technology suitable for Point-of-Care application to accurately screen elderly male populations for PC and to monitor the progress of patients undergoing PC treatment. Nanoporous thin-film sensor was able to detect prostate cancer markers concentrations as low as 1 pg/ml for NEM and 20 pg/ml for PSA.

APPROVAL FOR SCHOLARLY DISSEMINATION

The author grants to the Prescott Memorial Library of Louisiana Tech University the right to reproduce, by appropriate methods, upon request, any or all portions of this Dissertation. It is understood that "proper request" consists of the agreement, on the part of the requesting party, that said reproduction is for his personal use and that subsequent reproduction will not occur without written approval of the author of this Dissertation. Further, any portions of the Dissertation used in books, papers, and other works must be appropriately referenced to this Dissertation.

Finally, the author of this Dissertation reserves the right to publish freely, in the literature, at any time, any or all portions of this Dissertation.

Author _____

Date ___05/03/2016_____

DEDICATION

To my father, Mofleh Falah Alzghoul, my mother, Muna Abdulsalam, and all my sisters; Faten, Ruba, Zain, Ala'a, and Shifa. Thank you for being there for me, and for your support all the time.

With my love and appreciation.

Salah.

TABLE OF CONTENTS

LIST OF TABLES

LIST OF FIGURES

ACKNOWLEDGMENTS

CHAPTER 1

INTRODUCTION

1.1 Overview of Nanosensors for Biodetection

Technology is growing rapidly, and this affects our lifestyle. As a result, we need to keep pace with developments that accrued in our world. Biomedical engineering is an engineering field that concerns engineering methods such as electrical, optical, mechanical, and chemical to medical and biological applications [1].

Biomedical engineering has many aims and goals, such as to develop amended kinds of animals and plants for food manufacturing, to design new diagnostic tests methods for diseases, to improve drug release devices, to improve the safety and the efficiency of medical devices, to improve diagnostic imaging systems, to give better solutions for neuro system defects, as well as many other goals [1].

Also, Biomedical engineers are working on connecting new technologies to medical and biological fields in many ways like innovating new diagnostic and treatment methods and improving existing biosensing capabilities. Reliable solutions are needed to reduce the cost and the demand on the health care system and to minimize the number of deaths.

In general, biosensors consists of four major components (Figure 1-1) [2]. The first component is the analyte, which is a biological or chemical compound that will be

easured and/or monitored. The receptor is the second component of the biosensor. It has a

crucial role in immobilizing the component that will be detected (analyte) over the sensor

surface. To make sure that the sensor is accurate and reliable, the receptor should only

bound to the analyte. Antigens, which can be defined as foreign substances that catalyze

the body to produce antibodies [3], are examples of analytes. Antigens have a significant

part to which antibody attached to; this part is called an epitope.
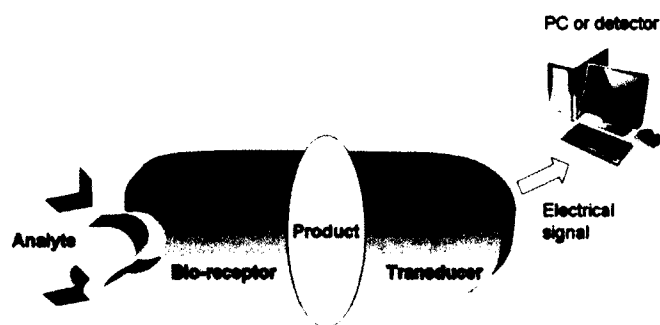
Figure 1-1. Schematic of biosensor four major components (analyte, receptor, transducer, and detector) [4].

Antibodies are an excellent example of bioreceptors. An antibody is a large

protein that is generated by plasma cells. It has a Y-shape, with the two upper arms called

fragment antigen binding (F_{ab}) regions, which make contact with, and bind to, the

antigen.

By knowing that each antibody antigen binding site (paratope) is specific to each

antigen epitope, we can consider that the binding relation between paratope and epitope is

like a lock-key relation. The antibody base region is called fragment crystallizable region

(F_c), and its primary function is to make and provide an extra binding with the antigen.

Since enzymes have specific binding properties, they could also be used as a

receptor for biosensing applications, especially for the DNA detection.

The transducer is the third component of the biosensor. It transforms signals from one form to another. For example, a Quartz Crystal Microbalance (QCM) device converts the pressure applied over a quartz surface into a change in frequency [5]. The fourth component of the biosensor is the detector, which is the part that identifies the stimulus [6].

Biological analytes are often small in size, ranging from a few nanometers to a few micrometers, and they are often low-weight. As a result, there is a significant need for sensors that can work at micro or nanoscale. Microscale and nanoscale biosensors include nanoparticle-based biosensors [7], acoustic wave biosensors [6], magneto-nanosensor biosensors [8], electrochemical biosensors [9], carbon nanotube-based sensors [10], nanowire based sensors [11], surface enhanced Raman spectroscopy [12], and fluorescence and light scattering [13].

Biomolecules can be detected through two methods, attached to a tag or a label like epitope tags, radioisotopes, fluorescent dyes [14-16], or not attached to a tag (label-free). However, the labels could affect the properties of the analyte; they can be expensive or toxic and require a skilled person to work with them. On the other hand, label-free biosensing technique will reduce the cost of the experiment, and analyte specifications will not be affected since it has no connection to any external compound.

The label-free technologies are currently used for biological, environmental and biomedical applications [5, 6, 17-19]. Label-free biosensors are grouped into three classes: optical, mechanical, and electrical [20-23].

1.1.1   Electrical Label-Free Biosensors

Carbon nanotubes and nanowires are good examples of electrical label-free biosensors [10, 11, 24]. An amperometric carbon nanotube (CNT)-based sensor is

illustrated in Figure 1-2 [24]. In general, electrochemical amperometric sensors have

three electrodes [25]: a working electrode, a reference electrode, and a counter electrode.

This method is sufficient for detecting proteins or DNA, does not consuming much

energy, and is cost-effective.

By applying voltage bias between working and counter electrodes, an oxidation-

reduction reaction took place in a solution that contains biomolecules. As a result,

electron transfer reactions take place over the surface of a working electrode. Since CNTs

encourage electron transfer reactions more effectively than traditional metals [26], CNTs

were incorporated to a Platinum (Pt) working electrode by using thermal chemical vapor

deposition method.

Maehashi et al. used this type of sensor to detect prostate specific antigen (PSA);

he immobilized PSA monoclonal antibodies (mAb) over CNTs via crosslinkers, and he

recorded the electrochemical signal by using differential pulse voltammetry (DPV).

After the PSA marker was immobilized, DPV showed a significant increase in

electrochemical signal and thus indicated the formation of the antigen-antibody complex.
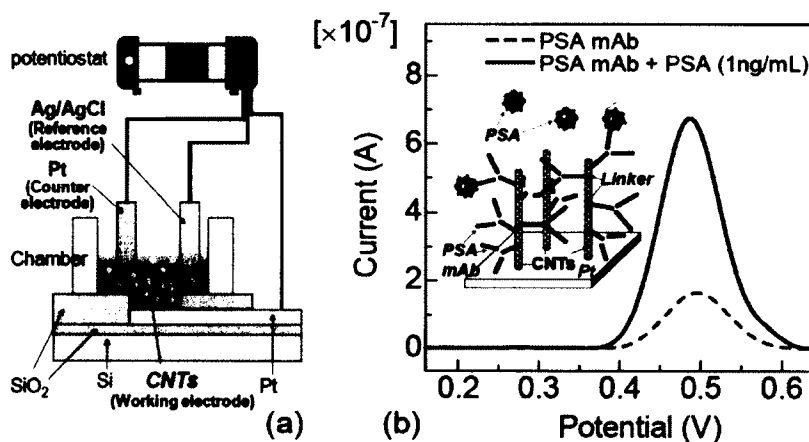
Figure 1-2. Amperometric carbon nanotube (CNT) Based sensor. (a) Device setup. (b)
The electrochemical signal measured by using DPV. The red dashed line represents the
signal measured when only PSA-mAb immobilized over CNTs; the blue line is the signal
after PSA is attached to PSA mAb and forming the antigen-antibody complex [24].

1.1.2 Mechanical Label-Free Biosensors

Mechanical label-free biosensors provide a sensitive method for detecting the accumulated analyte mass over receptor. QCM is a mechanical label-free biosensor that can measure the change in mass even in µg or ng level.

The operating principle of QCM is based on measuring the changes in quartz piezoelectric resonant frequency. When a small mass of matter binds to the surface of the quartz, the resonant piezoelectric frequency decreases according to the following relation:

$$\Delta f = -C_f \, \Delta m, \qquad\qquad \textbf{Eq. 1-1}$$

where Δf is change in resonant piezoelectric frequency, C_f is crystal sensitivity factor, and Δm is a change in mass over quartz piezoelectric sensor [5].

QCM has a wide range application, such as biosensors, gas sensors, environmental monitoring, and the interactions of surface molecule.

A surface-stress mechanical biosensor with a cantilever is another type of the mechanical label-free biosensors [27]. The weight of a biomolecule attached to the surface of the sensor and band biomolecules to functional groups on the surface of the device lead to stress on cantilever, which causes a deflection of a cantilever. (Figure 1-3).
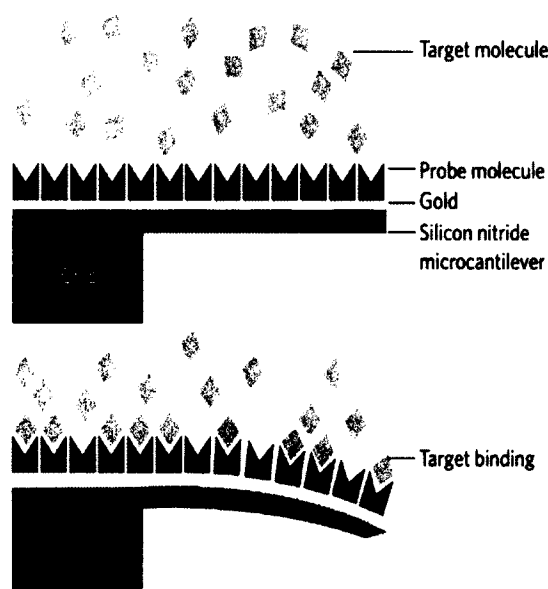
Figure 1-3. Schematic of cantilever surface-stress biosensor [27].

1.1.3   Optical Label-Free Biosensors

Optical biosensors have many features such as high sensitivity and accuracy, ability to provide a real-time monitoring, negligible environmental noise, electrical passiveness, multiplexing capability, and minimum electromagnetic interference. These properties enable a wide sensing range, high resolution, and resistance to high temperatures, as well as a chemically reactive environment.

The constant improvements of the quality and functionality of optical components such as light probes, optical lenses, and mirrors, and advancements in the area of the signal processing, make the optical sensing methods attractive for environmental and biomedical applications, especially in molecular studies and early biomarker detections, because of the high sensitivity. Optical sensing is also compatible with micro and nano thin-film devices that are based on silicon or anodic aluminum oxide [28, 29].

Optical sensors can measure and sense many physical, chemical and biological components such as pressure, temperature, strain, liquid level, vibration, acceleration,

rotation, PH level, magnetic field, flow rate, liquid level, displacement, radiation level, humidity level, velocity, electric field, acoustic field, or force, or distinguish between chemical species, proteins, or biomolecules, [30-34].

Change in beam intensity for one or multiple light beams, or interacting and interfacing between light beams, which cause changes in signal phase, are two principal optical sensing methods. All optical sensors have two principal parts: an emitter for emitting and transmitting light beams, and a receiver for collecting and receiving signal.

Fabry-Perot Interferometer (FPI) is an optical device that was invented in 1899 and worked on the principle of multiple-beam interference (Figure 1-4). As shown in Figure 1-4, the incident light I_i is the input signal, the reflected light signal is I_r, while the transmitted signal is I_t.

Fiber probe is used to emit and collect the reflected light. The same fiber probe sends the signal to the spectrometer. As a result of a light interference, fringes can be observed in different shapes such as rings, strips, and curves.

The path differences between two sequential beams is $\delta = 2nd\cos\theta$, where θ is the angle of incidence. The ratio between the reflected light intensity and the incident light intensity can be expressed as:

$$\frac{I_r}{I_i} = \frac{4R\sin^2\frac{\delta}{2}}{(1-R)^2 + 4R\sin^2\frac{\delta}{2}} , \qquad \textbf{Eq. 1-2}$$

where R is the surface reflectance, I_r is the intensity of the reflected light, and I_i is the intensity of the incident light [35].
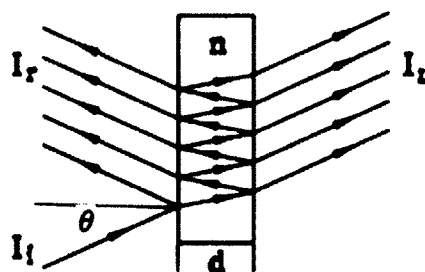
Figure 1-4. Schematic of FPI operating principle [35].

Porous silicon can be used as an FPI sensing platform to sense biomolecules. The sensor detects the change in optical thickness ($2nd$) of the same biological thin film layers.

$$2nd = m\lambda, \qquad \textbf{Eq. 1-3}$$

where n is the effective refractive index of the porous silicon with all other attached biological layers, d is the physical thickness of the porous silicon with all other attached biological layers, m is the spectral order of the optical fringes and λ is the light wavelength [36, 37] in vacuum. Fringes are produced by the interference of light reflected from multi interfaces accrued in the structures [37].

Finesse (F) is an important parameter of FPI that reflects FPI resolution. This parameter is defined as a numerical value that describes the sharpness of the wave maxima. Mathematically, finesse is the ratio between peaks distance $\Delta\lambda$, to the full width half maximum (FWHM) $\delta\lambda$.

$$F = \frac{\pi\sqrt{R}}{1 - R}, \qquad \textbf{Eq. 1-4}$$

Using nanopore platform in FPI sensor (Figure 1-5) has many advantages, such as an increased sensing surface area, extended penetration depth of the excited light, and amplified optical transducing signal [38]. Nanopore platform in FPI sensor, with specific

characteristics like nanopore diameter of 50 nm and a gap size of FPI cavity of 50 μm,

provides 20 times improvement in a free spectral range, which is the frequency or

wavelength spacing between two sequential transmitted or reflected optical intensity

maxima, and two times improvement in finesse [38].
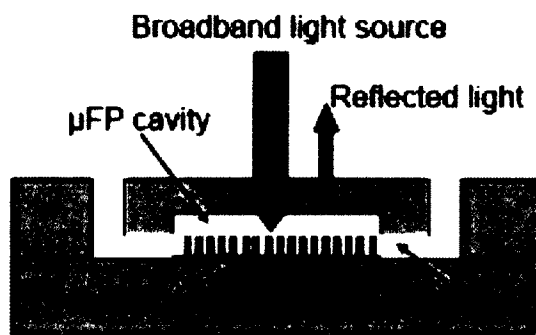
Figure 1-5. FPI device cross-section with a microfluidic channel [39].

1.2　Prostate Cancer Biomarkers

1.2.1　Prostate-Specific Antigen (PSA)

Prostate cancer (PC) is the second most common cause of cancer deaths in the US

men [40]. According to the American Cancer Society, 233,000 new prostate cancer cases

appeared in the year 2015, and the mortality rate will be around 13% (30,000 people)

[41].

There are three options to reduce the number of prostate cancer fatalities and the

demands on the healthcare system of such disease: 1) decrease the incidence of illness, 2)

better treatment, and 3) early detection [40].

Modern surgical processes and radiation methods have been improved lately, but

since PC is a hormonal metastatic disease, the improvement of therapeutic techniques did

not reduce the mortality of PC.

The third method to minimize the number of deaths is to improve early prostate cancer detection. In order to detect PC early, the most common used method is the serum screening of prostate-specific antigen (PSA), followed by the transrectal ultrasound guided biopsy. Since these existing methods are not efficient to detect the PC early enough, new methods for early detection are needed.

The PSA is a blood serum tumor marker and is the most widely used marker for the PC. The PSA was introduced for the first time in the 80's of the second millennium at Roswell Park Cancer Institute in Buffalo, NY by Wang and associates. The PSA is classified as one of the most important tumor markers, since it has a substantial role in managing men's lifestyle [40].

The normal level of PSA is less than 2n g/ml. The threshold value for cancer detection is ≤ 4.0 ng/ml of PSA in serum, and the gray zone is between 4.1-10 ng/ml (meaning that the patient may have a prostate inflammation or a benign prostatic hyperplasia (BPH), which increase serum PSA levels of up to 10 ng/ml [42, 43], or prostate cancer). The PSA is not an ideal marker for PC since it is secreted by normal as well as malignant prostates, and PSA levels reflect the size of the prostate rather than cancer. An elevated level of PSA might be due to PC or benign diseases, such as BPH [40, 44, 45]. Also, the PSA screening test gives too many false positive or negative results. The false-positive results lead to an additional test called transrectal ultrasound (TRUS)-guided biopsy procedure, and this procedure is invasive, repetitive, and costly.

A man of age 40-50 years has a 34% chance of early occult PC [46], but after repeated screening, only one eighth of men will be diagnosed with cancer during his life

period. The chance of detecting PC clinically for a man who is younger than 50 years old is less than 0.3% [44, 47].

Although PSA screening is the standard method to detect PC, debate continues as to whether to perform the test, at what age a man should have it performed, the recommended threshold for the PSA levels, and at what age to stop the screening [45].

In order to improve and enhance the PSA test in the diagnostic of PC, some hidden features of the PSA, called PSA derivatives tests, are added to the traditional PSA screening. The common PSA derivatives are: PSA velocity, PSA density, age-specific PSA, and the ratio of total to free PSA [40].

PSA circulates in the blood in two different forms, freeform and complex form. When PSA is attached to proteins, it is called complex PSA, if PSA is not attached to any other proteins, it is called free PSA. Total PSA is the amount of free PSA and complex PSA combined.

PSA velocity is a method that measures the changing of PSA levels over time. The PSA levels rise slowly in healthy men and rapidly in PC patients. This method can be applied to both PSA and free PSA serum levels. When PSA levels increased at a rate more than 0.75 ng/ml per year, it indicates that this person is at higher risk of having prostate cancer. Other researchers suggested that the increasing rate threshold of PSA levels must be around 25% increment in PSA concentration compared to their previous test. For free PSA, any change over 36% in their previous test ratio must be considered dangerous [40, 48].

PSA doubling time (PSADT) is defined as the time needed for levels of PSA in the blood to have the double amount. A PSADT less than ten months could indicate metastatic disease [49-52].

PSA density is the second concept that can help in enhancing PSA prostate cancer screening. PSA density is calculated by dividing the PSA level by the volume of the prostate. For example, if a person has 80 cm^3 prostate volume with 8 ng/ml PSA level, the calculated density will be 0.1 ng/(ml·cm^3), and if another person has 40 cm^3 prostate volume with 8 ng/ml PSA level, the calculated density will be 0.2 ng/(ml·cm^3). As a result, the individual who has larger PSA density will have more chance to have PC, and the person with larger the prostate volume (lower PSA density) will show benign histology (see Figure 1-6).

Age-specific PSA is also known as an age-adjusted PSA. It is a concept that determines the threshold level of PSA that will indicate that the man of a certain age has prostate cancer.

This cutoff level will change over years. According to an age-specific PSA concept, a man who is younger than 50 years old should have PSA screening level less than 2.5ng/ml, but after 30 years, average levels could be between 0 to 6.5 ng/ml.

PSA: 8.0 ng/ml
Volume: 80 cc
PSA Density: 0.1

PSA: 8.0 ng/ml
Volume: 40 cc
PSA Density: 0.2
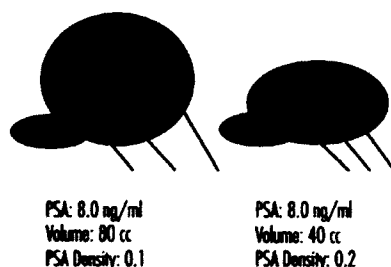
Figure 1-6. PSA density. The right prostate has a volume of 40 cm3 with PSA level 8ng/ml, and the one on the left has a volume of 80 cm3 and PSA level of 8ng/ml. The prostate with higher density might have cancer, while the prostate on the left showed benign histology [40].

PSA circulates in the blood in two different forms, freeform and complex form with protein, such as alpha-1 antichymotrypsin and alpha-2 macroglobulin, most of the blood PSA is bound to alpha-1 antichymotrypsin [40, 53]. When PSA is attached to alpha-1 antichymotrypsin, it can be detected by immunoassays (a method used for detecting proteins, for example enzyme-linked immunosorbent assay (ELISA)) because two epitopes are remaining free, when PSA is attached to alpha-2 macroglobulin, all epitopes will be attached, and available assays cannot detect this form of complex PSA. Free PSA levels are higher in men who do not have prostate cancer [40, 54, 55].

The PSA test is significantly enhanced when the PSA and the free PSA (f-PSA) levels are combined together, and the ratio of the free to the total PSA, or the free to the complex PSA, is calculated [40]. This test is helpful for men that have PSA levels in the gray zone (4.0 to 10 ng/ml) and a negative result from ultrasound biopsy. Catalona et al. tested the ratio of free to a total of 773 men who had PSA levels in the gray zone and negative ultrasound biopsy, 49% of which had prostate cancer [40, 56].

An important analytical problem appears in calculating the free PSA to total PSA ratio because of the difference between PSA manufactured arrays. Some manufactured PSA arrays show lower PSA levels than the other, but this issue did not hinder the fact that the f-PSA level, combined with the PSA levels, improves the PSA traditional test by calculating the probability that a patient has cancer (see Tables 1-1, 1-2) [40, 57]. Although PSA screening is the common test for prostate cancer, it is a controversial tumor marker. PSA levels are not controlled only by cancer, but it can also change in a non-malignant disease like BHP. The patient's age and race also influence the PSA levels in a patient's blood [44].

Table 1-1. The relation between PSA blood serum levels and the probability of having PC [40].

PSA blood serum concentration (ng/ml)	Probability of having PC (%)
≤ 2ng/ml	1%
2-4 ng/ml	15%
4-10 ng/ml	25%
>10 ng/ml	>50%

Table 1-2. The relation between free to total PSA ratio for men who have PSA blood serum levels in the gray zone (4-10 ng/ml) and the probability of having PC [40].

Ratio of free to total PSA (%)	Likelihood of having PC (%)
0-10%	56%
10-15%	28%
15-20%	20%
20-25%	16%
>25%	8%

Moreover, highly aggressive cases of PC, which often have neuroendocrine features and do not display a significant increase in serum PSA levels, cannot be detected by the PSA test. As many as ~15% of PC patients exhibit PSA levels below the adopted threshold 4 ng/ml [45].

Because of the poor reliability of the PSA blood test, some new reliable prostate cancer markers are needed. The markers should clearly discriminate PC from other prostate diseases, predict tumor formation at a very early, preferably premalignant, stage, and distinguish aggressive tumors from indolent ones at an early stage [58].

As a result, the disadvantages of the PSA test are:

1. The PSA test does not give a good idea about progression cancer levels.

2. The PSA test does not reflect the aggressiveness of prostate cancer.

3. The PSA test does not predict the clinical nature of cancer. [59].

1.2.2 Neuroendocrine Marker (NEM)

Neuroendocrine Marker (NEM) is a novel transcript and was recently identified from the prostate cancer complimentary DNA (c-DNA) library in our collaborator's (Dr. Shah) laboratory at the University of Louisiana at Monroe (ULM) [60]. NEM produced by sub-cloning the complementary DNA in a vector. Then, the genetic structure containing NEM c-DNA was applied to a prostate cancer cell line, and after incubation and culturing, affinity chromatography obtained the expressed protein [59, 60].

In situ hybridization and immunohistochemistry studies suggest that NEM is selectively localized in malignant, but not benign, prostate epithelium [60]. The expression of NEM is increased with cancer progression. NEM immunoreactivity (NEM-ir) detected in sera of elderly men; serum NEM-ir level in PC patients was three-fold greater than those in non-cancer individuals [60-62], suggesting that NEM, either alone or in tandem with PSA or other markers, can serve as a valuable tool to reliably diagnose populations at risk, and monitor the patients undergoing anticancer therapy. Immunohistochemistry of primary prostate tumors has revealed that 47-100% of PCs demonstrate foci of neuroendocrine differentiation [59].

Secretory products of neuroendocrine (NE) cells may support growth or increase the survival of neighboring tumor cell populations because the cells adjacent to NE cells have been shown to display increased expression of mitogenic markers, such as proliferating cell nuclear antigen [59] (Figure 1-7).
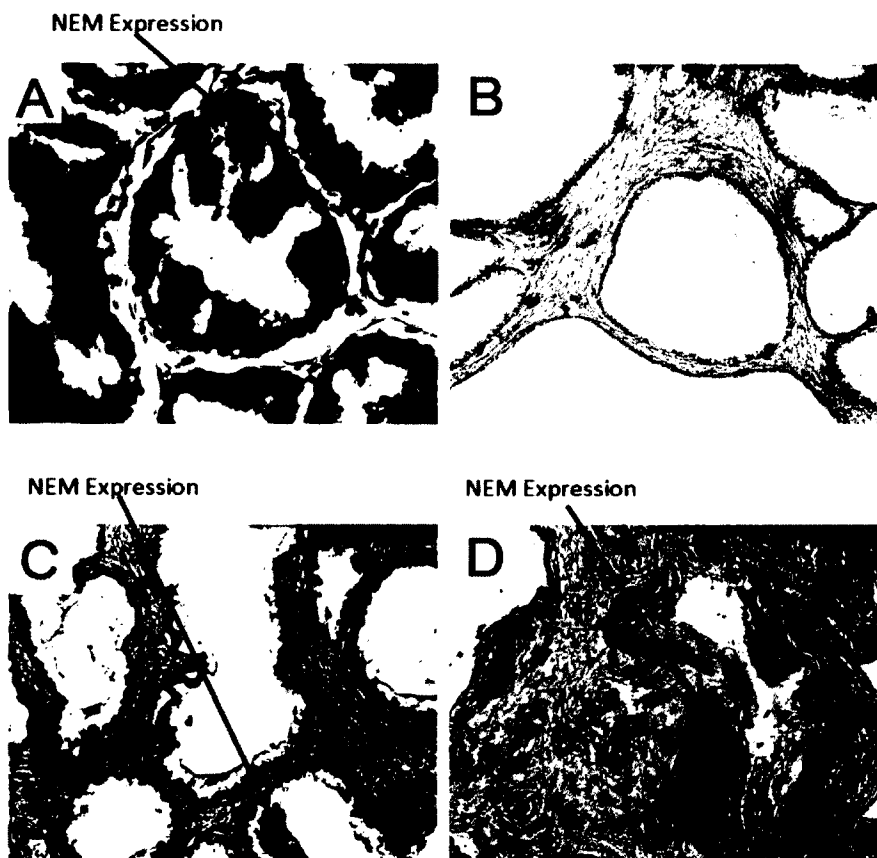
Figure 1-7. NEM Immunohistochemistry (IHC) in biopsy samples. (A) Prostate Cancer is an epithelial cancer, and NEM Expression is also epithelial. (B) NEM expression is not detected in the benign epithelium. (C) NEM expression is detected in early stages of the disease. (D) NEM expression increases with tumor progression [59].

To detect NEM, antibodies were prepared in rabbits by injecting them with antigens. After immune response took place, blood samples were removed from the rabbits and the immunoglobulin fraction of blood sample serum were filtered and used as antiserum [59, 60].

Polyclonal and monoclonal antibodies help in NEM detection in both blood and tissue, and they give useful information about the cancer grade, whether the cancer is metastatic or not, especially for patients with low PSA serum levels [60].

Current evidence also suggests that the tumors of PC patients with "low or normal" serum PSA levels usually display high NEM secretions and aggressive growth,

raising a possibility that the genes associated with neuroendocrine features of the prostate may be useful in detecting PC and may also stratify aggressive tumors from the indolent ones. In addition, NEM is working as a cancer growth factor too; when NEM binds to its receptors located in prostate tissue, cancer will grow and overrun. Blocking the linkage between the NEM and its receptors by using an antibody directed against the NEM or its receptor would reduce the growth of cancer cells and give some therapeutic benefits [59, 60, 63, 64] (see Figure 1-8).
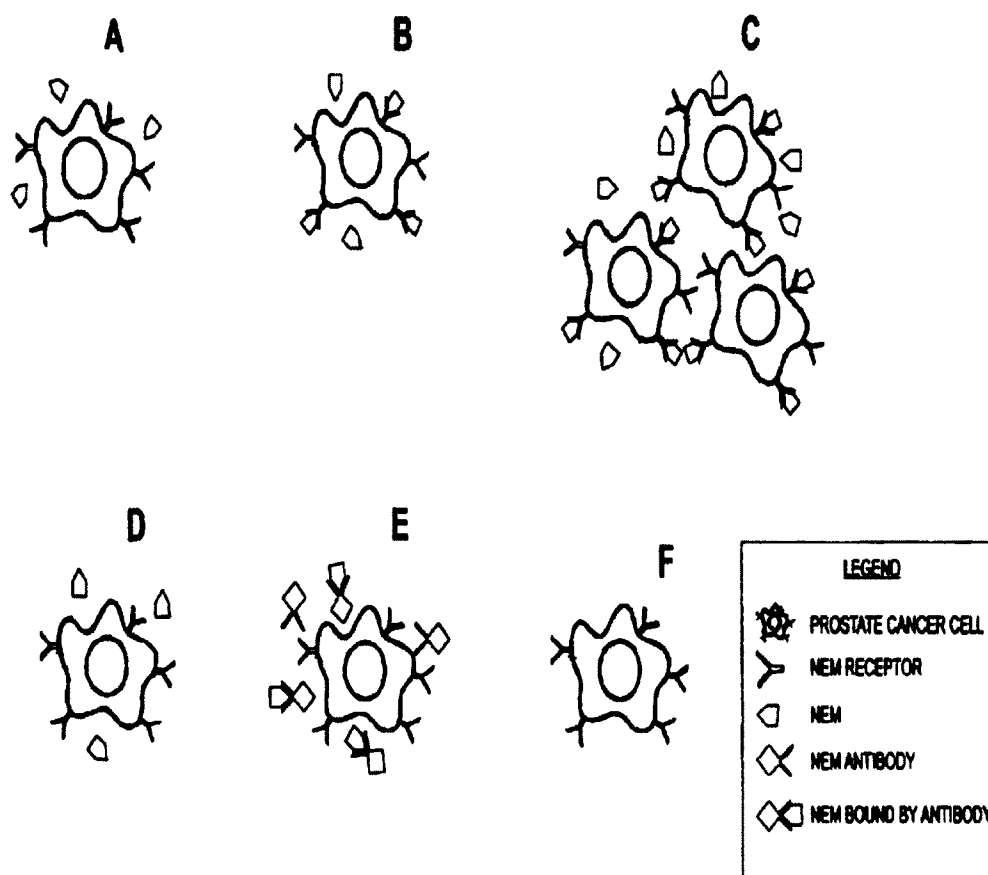
Figure 1-8. The prostate cancer therapy by using NEM. (A) Prostate cancer cell surrounded by NEM. (B) NEM bounded to its receptors. (C) Cancer cells, growth and proliferation. (D) Prostate cancer cell surrounded by NEM. (E) NEM is blocked by an antibody directed against. (F) Cancer cell did not grow or proliferate [59].

The NEM is detected by several methods such as radioimmunoassay, enzyme-linked immunosorbent assay (ELISA), fluoroimmunoassay, immunohistochemistry, sandwich ELISA, and any other peptide detection techniques [59, 60].

NEM has been found in relatively high levels in blood serum samples from prostate cancer patients. NEM novel biomarker can detect cancer in early stages as well as high-grade tumors, NEM also may help at the beginning of PC detection, and it could reduce additional biopsy procedure (up to 75%). A study sample that consists of 69 samples from PC and non-cancer patients exposed that NEM levels of PC serum samples are three times higher than in non-cancer patients [65].

NEM also proposed as more reliable PC marker than PSA incorrectly detecting PC with less false positive and negative diagnostic. The larger sample size consists of more than 500 patients investigated, and the results showed that prostate cancer patients have higher NEM levels in blood serum than men who do not have PC [66].

There is a correlation with high PSA levels and NEM levels in the prostate cancer patients' serum. Some prostate cancer patients have low PSA serum levels and higher NEM levels. Therefore, NEM could be useful in cancer detection in parallel with a PSA test and could help in detecting PSA false positive or negative results.

1.2.3 Other Prostate Cancer Biomarkers

Several novel biomarkers to detect and screen prostate cancer have been discovered and tested lately. Those biomarkers are classified according to the source of the biomarker: serum biomarkers, tissue biomarkers, and urine biomarkers [49].

1.2.3.1 *Blood Serum Biomarkers*

Human prostatic acid phosphatase (PAP) is one of the oldest serum biomarkers for PC. PAP was discovered in the 1930's; researchers showed that high levels of PAP

could indicate the metastatic PC [49]. Other studies concluded that PAP levels are related to lymph node disease and metastases. Once the PSA was discovered, the PAP screening was stopped.

Early prostate cancer antigen (EPCA) is a series of proteins in blood serum that promotes PC in its early stages. These proteins reflect the relation between PC and the changes that occur in the nuclear matrix of the prostate. The levels of EPCA proteins are higher in adjacent areas of a prostate tumor and exist only in PC patients [49].

In 2005, EPCA had proven to have a high detection sensitivity and selectivity, as shown in a Kagawa University study, in which 50 men with PC and ten controls with bladder cancer but not prostate cancer. The EPCA method detected malignancy in 94% of PC patients and was negative in all controls [49, 67]. Two years later [49, 68], another set of proteins that is related to nuclear changes due to the PC were discovered and called EPCA-2. The newly discovered proteins were able to detect aggressive PC, as well as differentiate men with the organ-confined disease.

Prostate-specific membrane antigen (PSMA) is a 750 amino acid Type 2 trance membrane that has three dimensions: intracellular, transmembrane, and extensive extracellular sequence [69].

The PSMA is present in very aggressive cancers, and it can better detect high-grade tumors than PSA. After several studies on PSMA, assays for that protein were developed, such as immunoassays and Western block assays [40].

Pro-PSA is another prostate cancer biomarker. It is similar to PSA in 80% of DNA sequences and can have several forms [40]. One form is the enzymatically inactive (i-PSA) and another form is the B-PSA found in patients with the BPH. The Pro-PSA

may reduce the unnecessary biopsy procedures for men with PSA levels in the gray zone [40, 49].

Prostate cancer biomarkers are not limited to blood serum; Some PC markers are discovered from prostate tissue, like Glutathiones-transferase π (GSTP1), which is unmethylated in normal human tissue and hypermethylated in prostate cancer samples [40, 70].

1.3   Previous Work

Label-free optical sensors based on anodic aluminum oxide (AAO) technology apply to several fields, such as environmental studies (gas sensors) and biosensing applications. In general, this method is easy to maintain, has a low cost and is simple to operate. The operating principle is based on detection of changes in light interference within the sensor's Fabry-Perot cavity. The sensor's surface changes (analyte binds to AAO surface) due to chemical reactions which take place and change the effective index of refraction and the surface reflection coefficient (Figure 1-9) [71, 72].

Reflective interference spectroscopy is a label-free optical sensing method based on interference of white light over a thin film, and it depends on the product of the effective refractive index and accumulated layer thickness. When an analyte binds to the sensor surface, a change in the refractive index of the surface layer is detected by measuring the shift in the interference pattern [72]. Reflective interference spectroscopy usually uses a microfluidic cell to confine the liquid.
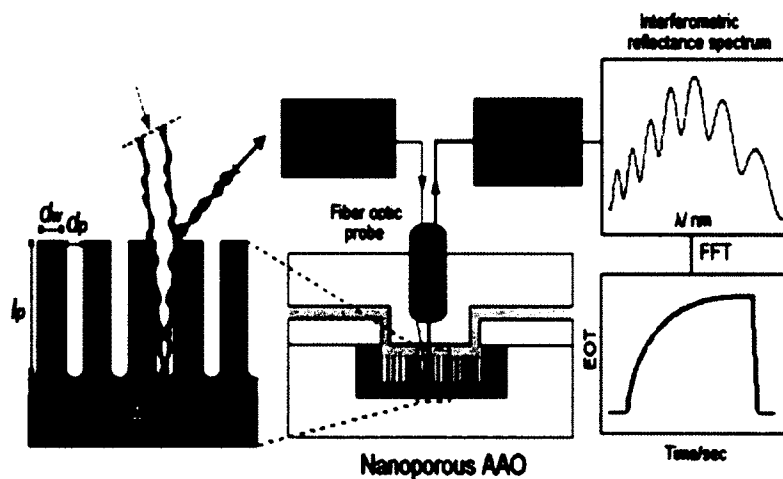
Figure 1-9. Schematic of reflective interference spectroscopy. White light from tungsten lamp transmitted and received by fiber optic probe, the reflected signal processed by spectrometer appeared on display as fringes, when fast Fourier transform applied to the reflected signal, effective optical thickness vs. time graph generated [72].

Many studies showed and approved high AAO sensitivity, according to G. Wang et al. [73]. An AAO sensor is precise and able to detect small concentrations of biomolecules, and this advantage will help in detecting certain diseases that have very low biomarker levels [73]. They detected biotin diluted in the buffer at different concentrations by using electrochemical impedance spectroscopy. This device has two electrodes submerged in a buffer solution. The working electrode was made of AAO (see Figure 1-10), and Ag/AgCl was a reference electrode. When small amplitude of AC signal is applied to the electrodes that are submerged in a buffer solution, the impedance is measured as the actual system's response. After biotin is added to the buffer solution and the same AC signal is used, it is found that system impedance increased with increasing biotin concentration, and the lowest level measured by the sensor is 4 ng/ml [73]. The same group also used that device to detect dust mite antigen Der-P2. Der-P2 activates respiratory epithelial cells innate in Toll-like receptors (TLRs), which cause acute respiratory disease. The dust mite monoclonal antibodies (IgG) were immobilized over the AAO sensor by

making a self-assembled monolayer. The sensing range was from 1 pg/ml up to 5 μg/ml [74].
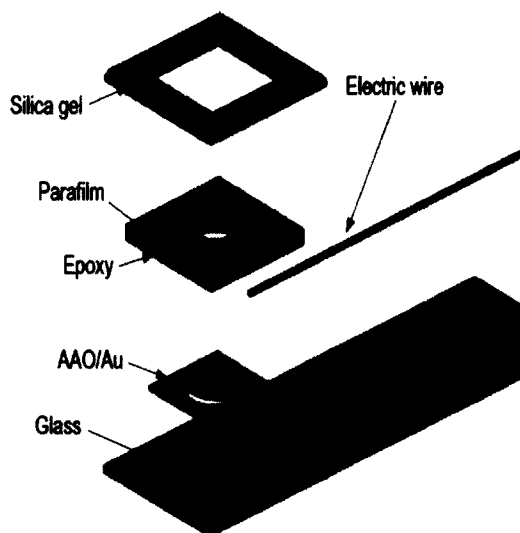
Figure 1-10. Schematic of working electrode that is made of AAO, The electrode are used in the detection of the dust mite antigen Der-P2 [74].

The 16-nucleotide DNA oligomers were detected by using the optical nanopore sensor [28]. This method showed a high efficiency in detecting both single and multiple layers of molecules immobilized over the sensor. When a white light is reflected from the sensor surface, interferometric reflectance spectra is detected as Fabry-Perot fringes (see Figure 1-11). When biomolecules attached to the sensor surface, Fabry-Perot fringes shift due to a change in the effective optical thickness of the porous silicon surface [28].
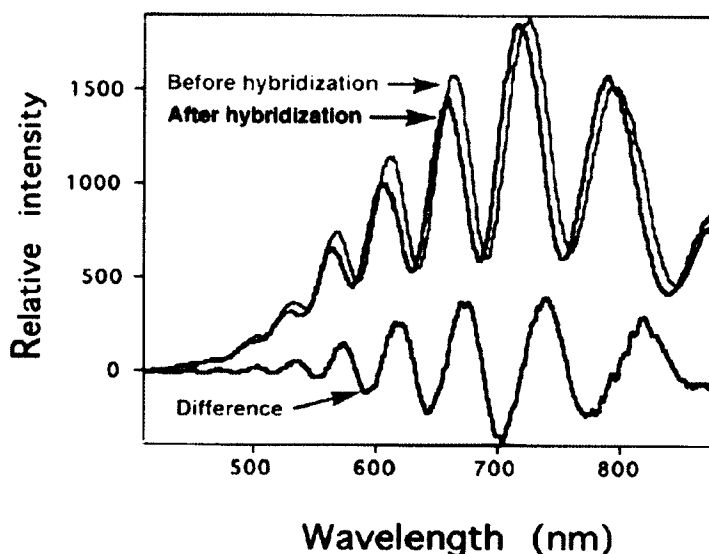
Figure 1-11. The Fabry-Perot fringes before (red line) and after (blue line) applying DNA over nanoporous sensor [28].

The optical nanopore sensor is efficient in real-time monitoring, especially for gas detection. Volatile sulfur compounds (VSCs) causes halitosis, or, in other words, oral malodor. VSCs generated when oral cavity proteins disintegrated by bacterial activity. Detecting gasses by using a nanoporous optical sensor is less complicated than a traditional method of UV-visible and fluorescence spectrophotometry, and it is not as expensive as listed methods [75].

1.4   Objectives

The primary goal of this research is to develop a fast, low cost, simple to operate, sensitive, specific, and selective PC detection device by using a nanopore thin-film sensor biased on nanoporous Anodic Aluminum Oxide (AAO) label-free biosensor, and to test the novel biomarker known as neuroendocrine marker (NEM) in parallel with prostate-specific antigen (PSA) in PC serum samples.

To reach our goal, we will test nanoporous thin film sensor sensitivity, specificity, and accuracy, and then compare human blood serum PSA and NEM levels results from

nanopore thin-film biosensor with ELISA test results. Finally, we will use the nanosensor

to determine the levels of NEM and PSA of pathologically confirmed PC human blood

serum samples.

CHAPTER 2

MATERIALS, INSTRUMENTS, AND METHODS

2.1 Materials

To detect prostate cancer biomarkers by using nanopore thin film, we need concrete materials that match experimental protocol [71], which includes 11-Mercaptoundecanoic acid (HSC10COOH,99%), N-(3-Dimethylaminopropyl)-N'-ethyl carbodiimide hydrochloride (EDC), N-Hydroxysuccinimide (NHS), bovine serum albumin (BSA), and glycine. All the materials were purchased from Sigma-Aldrich (Milwaukee, WI) and used without further purification. Mouse anti-human prostate-specific antigen (PSA) monoclonal antibody (detector mAb) (cat. # ABIN969369, clone#5A11E9) was purchased from Antibod-Online Inc., Atlanta, GA. The synthetic PSA peptide containing the middle region of PSA,was purchased from AVIVA Systems Biology, San Diego, CA.

2.1.1 11-Mercaptoundecanoic Acid

Eleven-Mercaptoundecanoic acid (MUA) (Figure 2-1) is an alkanethiol commonly used as a foundation for layer-by-layer coatings on gold surfaces. The protocol is straightforward and inexpensive. Adsorption to a gold surface requires approximately 18 hours [76]. Several parameters control MUA adsorption, such as incubation time, the type of the solvent, and MUA concentration. Due to a low toxicity and solubility, ethanol is the universal solvent for alkanethiols. Several studies show that

we can use other solvents instead of ethanol to reduce incubation time, such as hexane.

However, the results also show that the layer formed is not as organized as the layer

formed when using ethanol as the solvent [77].

MUA
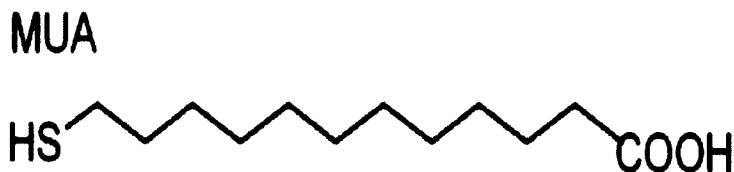
Figure 2-1. Structure of 11-mercaptoundecanoic acid (MUA) [78].

2.1.2 Phosphate Buffered Saline (PBS)

Phosphate buffered saline (PBS) is the most common buffer solution used in

biologically related research. This balanced salt solution keeps solution osmolarity and

pH constant. The primary function of PBS is to maintain biological molecules in perfect

condition while they are outside their normal growing environment by maintaining pH

between 7 to 7.6, which is a typical biological range.

To prepare one liter of PBS, start with 800 ml of distilled water, then add 8 g of

NaCl, 0.2 g of KCl, 1.44 g of Na_2HPO_4, and 0.24 g of KH_2PO_4. To adjust the pH to 7.4,

use aliquots of HCl as needed. Finally, add distilled water to make up a total volume of 1

liter.

PBS is non-toxic and has identical osmolarity to human fluidics. It is commonly

used as a wash solution for protein and cell culture experiments [79].

2.1.3 Bovine Serum Albumin (BSA) and Glycine

Bovine serum albumin (BSA) is a protein prepared from serum albumin obtained

from cow's blood. It is a large protein comprising 607 amino acids and has a molecular

weight of 66.5 kDa. Many biological research protocols use BSA due its stability and

weak affinity during biochemical reactions. It is also used to mimic human fluids. BSA

plays an essential role in blocking nonspecific immunoglobulins during

immunohistochemical reactions [80, 81].

2.1.4   N-(3-Dimethylaminopropyl)-N'-ethyl Carbodiimide Hydrochloride (EDC) and N-ydroxysuccinimide (NHS) Carbodiimide Crosslinkers

Two methods can be used to connect proteins or biomolecules over a gold

surface: passive absorption and covalent bonding using crosslinkers. Passive absorption

does not provide a stable connection, and biomolecules continuously disconnect from the

surface and occasionally lose their properties after surface absorption. On the other hand,

covalent bonding via crosslinkers provides a strong and stable connection that results in a

controllable protein coat layer. Carbodiimide compounds connect the amino or carboxyl

groups on antibodies to the free carboxyl or amino groups on bioanalytical platforms.

EDC is the carbodiimide compound used as a crosslink layer in this study. EDC is

a water-soluble, zero-length carboxyl-to-amine crosslinker. It reacts at biological pH, but

is most active at pH 4.5. When a protein comes into contact with EDC, an unstable

reactive o-acylisourea ester bond is formed. To improve EDC efficiency in physiological

pH media, we add NHS to EDC (Figure 2-2).
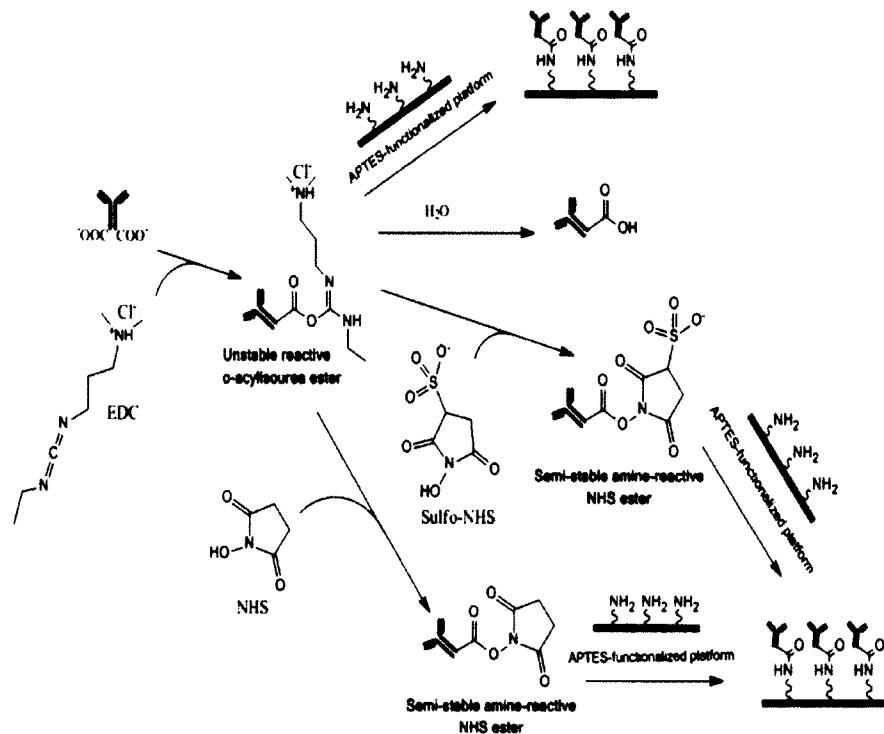
Figure 2-2. EDC linked to the carboxyl group on an antibody in aqueous solution generates an unstable, short-lived o-acylisourea ester bond. This bond breaks down in the presence of water. The addition of NHS stabilizes the amine-reactive intermediate by converting it to an amine-reactive NHS ester, thus increasing the efficiency of EDC coupling reactions [82].

NHS is a water-soluble compound that increases EDC workability by providing a more stable bond between the protein and crosslinker, called an amine-reactive NHS ester bond [82].

2.1.5 SU8

SU8 is a negative photoresist epoxy-based polymer. SU8 (Figure 2-3) is used in applications such as electroplating molds, sensors, actuators, micro-to milli-scale structures, microfluidic channels, and microelectromechanical systems (MEMS) and it is prepared by soft lithography [83, 84].
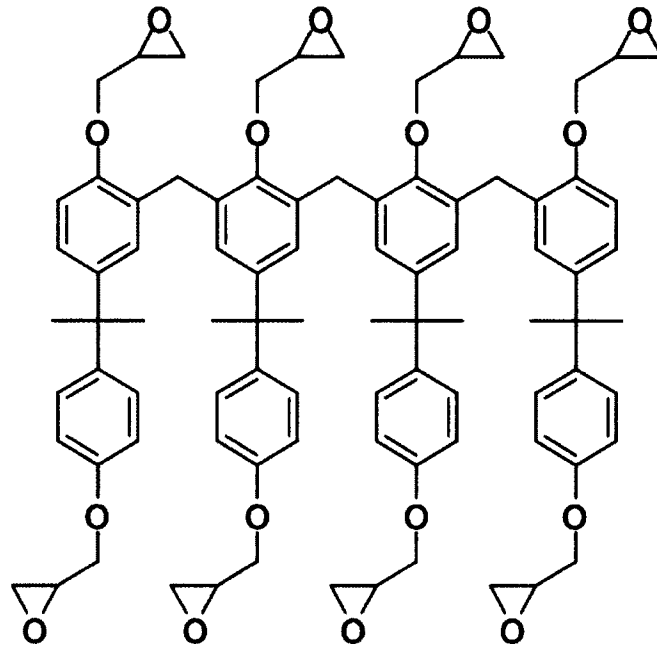
Figure 2-3. Chemical structure of SU8 comprising eight reactive epoxy functional groups [85].

The numeric eight in SU8 refers to the eight epoxy groups. Upon exposure to UV light, this polymer undergoes a photochemical reaction to produce an acid. The acid formed in the photochemical reaction acts as a catalyst in the exposed regions during post-baking exposure, thus promoting the crosslinking reaction. During crosslinking, a zipping process occurs between the epoxy groups that creates a three-dimensional network. A broad range of thicknesses (750 nm to 500 mm) with high aspect ratios can be obtained from a spin coater [86].

2.1.6   Polydimethylsiloxane (PDMS)

Polydimethylsiloxane (PDMS) is a bio-compatible silicon-based organic polymer used for fabricating and prototyping microfluidic chips, food additives (e.g., E900), contact lenses, medical devices, shampoos, and as an anti-foaming agent in beverages and lubricating oils. The PDMS is non-toxic, non-flammable, and inert,and thus useful for many biomedical applications [87, 88]. The PDMS empirical formula is $(C_2H_6OSi)n$

and its fragmented formula is $CH_3[Si(CH_3)2O]nSi(CH_3)_3$, where n is the number of

monomer repetitions (Figure 2-4). PDMS is hydrophobic, with contact angles from 90°–

120° with a melting point over 40 °C. PDMS is synthesized from dimethylchlorosilane

and water by the following reaction:

$$n \ Si(CH_3)_2Cl_2 + n \ H_2O \rightarrow [Si(CH_3)2O]n + 2n \ HCl.$$
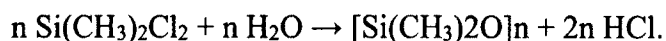
Besides biocompatibility, PDMS has many advantages, such as low cost and easy

fabrication, especially for micro-channel modeling [89, 90]. Microfluidic applications of

PDMS are challenged by aging; that is, the mechanical properties of PDMS can change

after a few years; thus, it is difficult to permanently deposit this material over metals or

electrodes. This issue is minimized by attaching the metal to glass, then bonding PDMS

over the glass after plasma treatment [91].
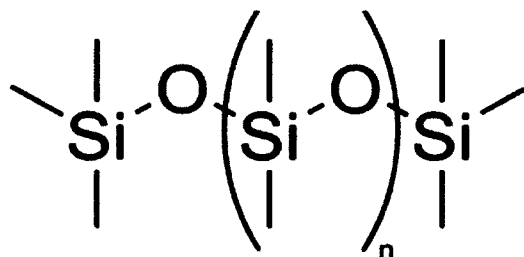
Figure 2-4. The chemical formula of PDMS [92].

2.2   Instruments

Figure 2-5 displays the experimental setup for the optical biosensor testing that

includes a white light source, optical probe, stage, spectrometer, and data analysis

system.

Data analysis
system

Probe holder

White light
source

Spectrometer

Nanopore thin film
sensor
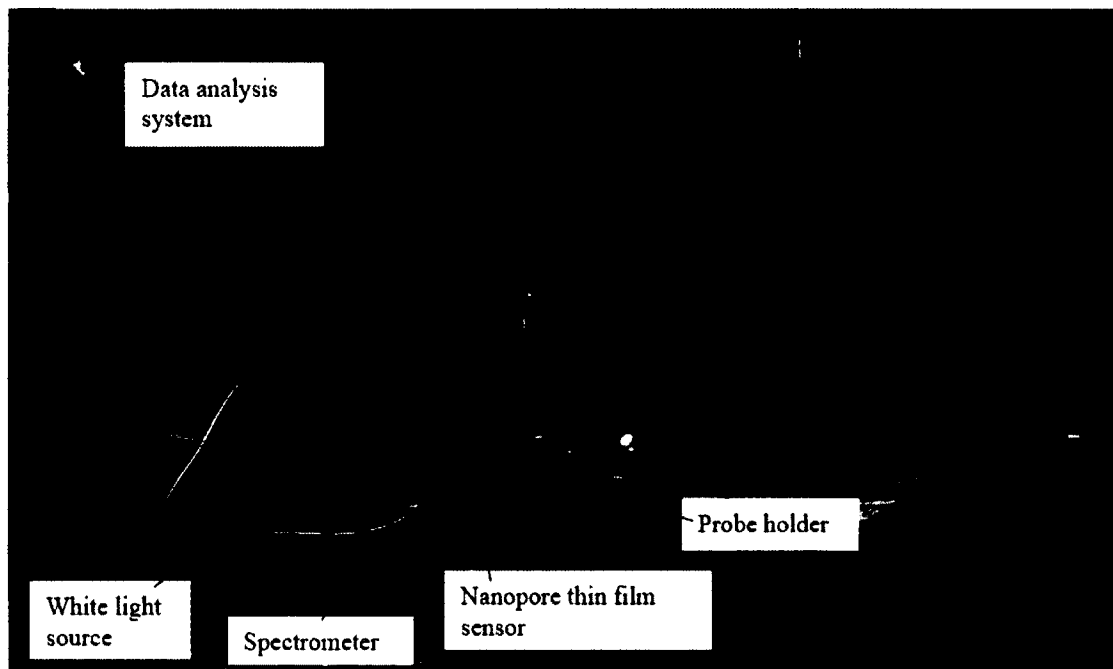
Figure 2-5. Experimental setup for optical testing on nanoporous thin-film biosensors.

2.2.1   White Light Source

A versatile tungsten white light source (Figure 2-6) LS-1 model, purchased from

Ocean Optics, Inc. was optimized for use in the visible and near-IR (NIR) range (360

nm–2500 nm). This light source offers high color temperature (3100 K bulb), efficient

output, and extended bulb life (around 900 hours). The LS-1 is connected to Teflon®

diffusion discs from the inside to create a diffuse light source optimized for coupling

fibers as well as for attenuating the source when spectrometer saturation is an issue.

To enhance the spectral envelope in the blue region relative to the red and NIR

regions (Figure 2-7), we attach a 12.7 mm blue filter called BG-34. The LS-1 is

distinguished with an SMA 905 connector for simple coupling to the optical fiber and

spectrometer.

Figure 2-6. LS-1 white light source.
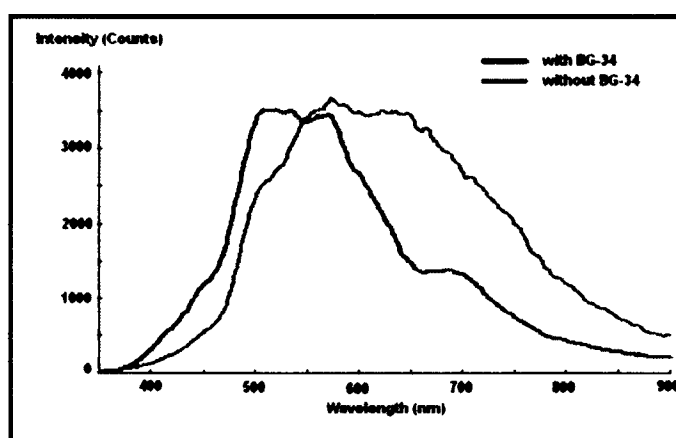
Figure 2-7. LS-1 white light source signal output with (blue line) and without (red line) the BG-34 filter.

2.2.2 Spectrometer

The USB 4000 (Figure 2-8) used in our experiments was purchased from Ocean Optics, Inc. (USA). Its 3,648-element CCD array detector has powerful high-speed electronics support for high spectral response and optical resolution in a single package. The resolution of the spectrometer is 0.21 nm and the smallest integration time is 3 ms. This model is perfect for experiments that need enhanced electronics, high resolution, and fast integration times.

USB 4000 is connected to an optical fiber probe by an SMA 905 connector and coupled to the computer via USB 2.0 or serial port. The spectrometer is controlled by a

Java-based spectroscopy software platform called *Ocean View*, which works on a range

of operating systems, such as Macintosh, Windows, and Linux.
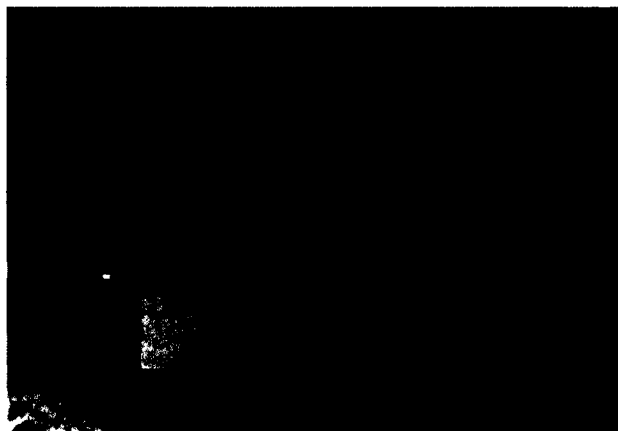
Figure 2-8. Photograph of USB 4000 spectrometer.

2.2.3   Probe Holder

To make sure that the angle of the probe and the distance between the probe and

the sensor is fixed, optomechanical components like a probe holder (Panavise Inc, USA,

model number PV-301) (Figure 2-9) are needed.

Figure 2-9. Probe holder.

2.2.4 Optical Probe

The optical probe is connected to the light source and to the spectrometer via an SMA 905 connector. The model used in our experiments is QR400-7-VIS-NIR (Figure 2-10) and the optical probe was purchased from Ocean Optics, Inc. (USA).

This probe is useful for applications that need fast measurements for small sample size. The bottom side of the probe is in charge of illuminating and detecting light from the same spot. The illumination probe stage has active cooling to minimize the overheating risk, which makes this probe suitable for bio-applications and especially for molecules with low melting points.

The reflection probe collects light at the same angle as it illuminates and can be used for both specular and diffuse reflection applications. The QR400-7-VIS-NIR has six illumination fibers around a single collector fiber and a 25° field of view angle (Figure 2-11). Each illumination fiber generates a cone-shaped light that overlaps at the center of the sample and is accurately perpendicular to the read fiber.
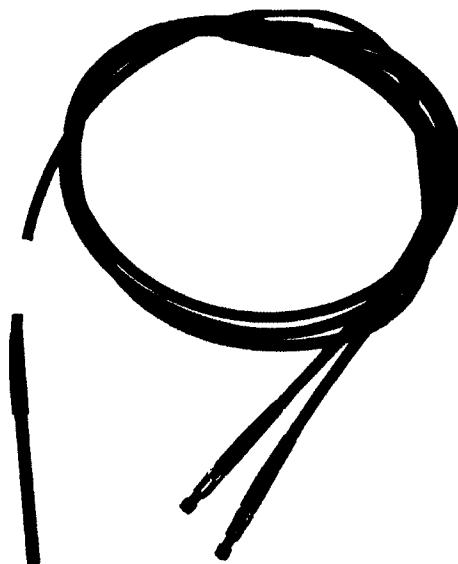
Figure 2-10. Photograph of the optical probe.
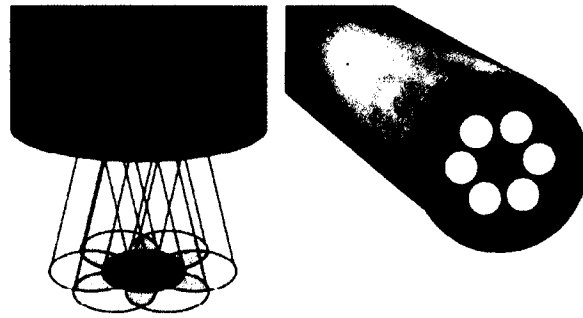
Figure 2-11. Schematic of illumination stage of the QR400-7-VIS-NIR probe and the cross-section of the optical probe.

2.2.5 Oxygen Plasma Cleaner

The oxygen plasma cleaner (Figure 2-12) uses an oxygen plasma to strip organic films (grease, oil, and photoresist materials) from substrate surfaces. By applying the oxygen plasma for a short period of time (15 min), any unwanted materials or thin layers of photoresist are removed from the sensor top surface and edges.

The oxygen plasma cleaner removes unwanted materials by applying low-pressure; in addition, heating over the sensor surface causes partial evaporation of contaminants. After that, plasma-abundant energy particles break down unwanted particles into smaller sizes that can be sucked off the surface.

Figure 2-12. Photograph of oxygen plasma cleaner.

2.2.6   Sputter Coating Machine

A sputter coating device is used to coat the sensor with gold. The one used in this experiment was manufactured by Cressington Scientific Instruments, Inc. (UK). This model has two operating modes: automatic and manual. The automatic mode has two options: time controller mode and multi-thickness mode.

2.3   Methods

These experiments are based on optical, biological, statistical, and signal processing principles. For optical methods, we describe Fabry–Perot interference from a thin nanopore film. In the biological part, the relation between antibody and antigen will be noted. Statistical methods, such as linear regression, Person's coefficent, and the coefficient of variation (CV), will be explained. Finally, we further elucidate on cross correlation signal processing technique.

2.3.1 Optical Methods

Fabry–Perot interfernometer (FPI) works on the principle of multiple beam interference (Figure 2-13) [93]. FPI is used in other sensing application as well (ultrasonic, chemical, biomolecules, and gas) [94, 95]. FPI can also be coupled with thermal and electrostatic actuators invested in optical communications by multiplexing wavelength division [96], surface plasmon resonance [97], and spectral endoscope optical imaging [98].
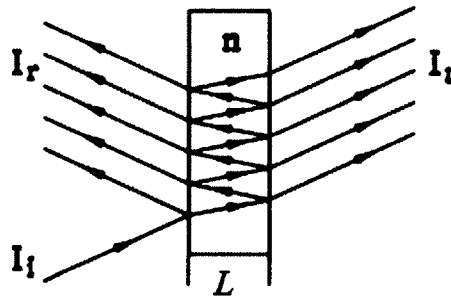
Figure 2-13. Schematic of Fabry–Perot interferometer work principle [35].

Emitted light I_i is the input signal, I_r is the reflected light signals, and I_t is the transmitted signal. A fiber probe is used to emit and collect the reflected light, and the same probe sends the signal to the spectrometer. As a result of light interference, fringes can be observed in different shapes, such as rings, strips, and curves [93]. This method is effective in measuring and monitoring changes in optical thickness.

If the wavelength of applied light is larger than the pore size of nanofilm, then optical interference of emitted light will be generated [99, 100]. Assuming that the film is optically transparent, and using the Fabry–Perot effect, the optical reflectivity spectrum model is as follows [101]:

$$I_r = \frac{2}{\pi}\left(\cos\frac{2nL\pi}{\lambda}\right)^3\left(\sin\frac{2nL\pi}{\lambda}\right) + \frac{1}{\pi}\left(\cos\frac{2nL\pi}{\lambda}\right)^2\left(4\pi - \sin\frac{4nL\pi}{\lambda}\right), \qquad \textbf{Eq. 2-1}$$

where I_r is the intensity of reflected light of wavelength λ, L is the thickness of the film, and n is the refractive index of the film.

When light is applied perpendicularly to the nanopore film surface (Figure 2-14), each fringe will have the following relation [36, 101-107]:

$$2n_{\text{eff}}L = m\lambda, \qquad \textbf{Eq. 2-2}$$

where n_{eff} is the effective refractive index of all the layers of nanopore substrate with thin biological films on top of it, L is the optical thickness of the film, m is the spectral order of the optical fringe, and λ is wavelength.

From **Eq. 2-2**, the term $2n_{eff}L$ is called the effective optical thickness (EOT). EOT is a function of optical thickness as well as effective refractive index.

The effective refractive index n_{eff} is a unitless number and is a function of the materials and the porosity (P) of the nanopore thin film structure [108]. Using Bruggeman's equation, n_{eff} can be calculated as follows [109]:

$$(1 - P)\frac{n_{Al_2O_3}^2 - n_{eff}^2}{n_{Al_2O_3}^2 + n_{eff}^2} + P\frac{1 - n_{eff}^2}{1 + n_{eff}^2} = 0, \qquad \textbf{Eq. 2-3}$$

where $n_{Al_2O_3}$ is the refractive index of alumina with a value of 1.67.
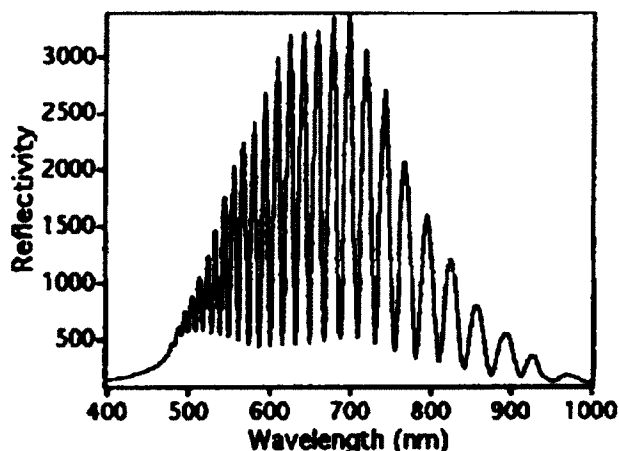
Figure 2-14. Interference fringes when the light is applied perpendicularly to the silicon nanopore film [101].

Localized surface plasmon resonance (LSPR) is a useful method to detect small changes that accrue to the sensor surface refractive index [110]. When an analyte is applied over a sensor surface, the refractive index and optical thickness will change. As a result, in comparison with the original signal (I_{r1}), the reflected Fabry–Perot fringe signal is shifted (I_{r2}) due to changes in the surface characteristics (Figure 2-15) [28].

We can measure the changes in nanopore thin film surface characteristics using three different methods [111]. The first uses the nanopore thin film as a waveguide, with the congruous modes as transduction variables [112-114]. The second method finds optical changes by measuring the shift that occurs at the Fabry–Perot fringes peaks [110].

The last method measures the effective optical thickness (EOT) by applying Fourier transform to the reflected spectrum [115-117].
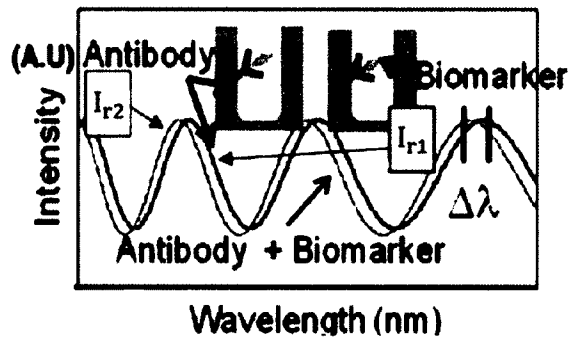
Figure 2-15. Wavelength shift ($\Delta\lambda$) due to change of surface characteristics of nanopore thin film. I_{r1} represents the reflected fringe signal after applying antibody. I_{r2} represents the reflected fringe signal after biomarker attached to antibody. $\Delta\lambda$ is the difference between I_{r1} and I_{r2} [65].

2.3.2 Antigen-Antibody (Ag-Ab) Relation

An antibody is a large molecular weight protein that has a Y-shape and relates to the family of globular proteins called immunoglobulins (Figure 2-16). Antibodies can attach to and mark foreign targets (antigens) like viruses and bacteria for destruction by the immune system [118].

Antibodies (Ab) generated by an individual for a specific antigen have the same structure, but they are unique in function since they comprise different amino acid sequences. Antibodies are the most diverse proteins known [118]. They are composed of three fragments, two of which are identical and used as antigen (Ag) binding sites.

These identical fragments consist of one heavy chain and one light chain polymer connected to form the paratope, which is the antigen binding site. The two identical fragments are called the antigen-binding fragments (F_{ab}). The third fragment (F_c) forms the base of the Y-shaped macromolecular structure and is crystallized during low-temperature storage [116, 118].
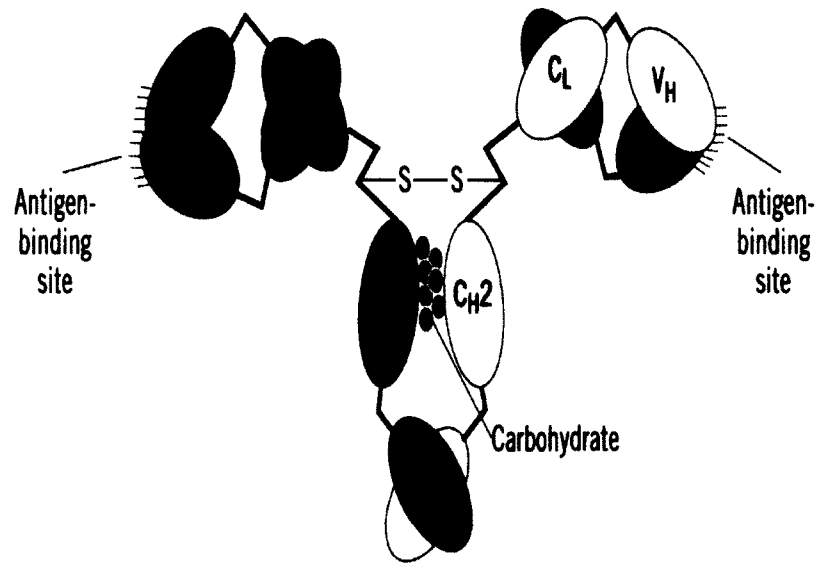
Figure 2-16. Schematic 3D model of an antibody [118].

The antigen–antibody reaction can be described as follows [119, 120]:

$$A_g + A_b \leftrightarrows A_g A_b.$$

Eq. 2-4

The association rate (v_a) of the antigen–antibody reaction is calculated as:

$$v_a = k_a[A_g][A_b],$$

Eq. 2-5

where k_a is the association rate constant, $[A_g]$ is the concentration of the antigen, and $[A_b]$ is the concentration of the antibody.

At equilibrium, the mass action law states:

$$\frac{[A_g][A_b]}{[A_g A_b]} = k_d,$$

Eq. 2-6

where k_d is the dissociation constant and $[A_g A_b]$ is the concentration of the antigen–antibody complex. This simplifies to:

$$k_d = \frac{1}{k_a}.$$

Eq. 2-7

The lower that magnitude of k_d, the higher the affinity of antigen–antibody binding.

The total concentration of antibody $[A_b]_T$ is the summation of $[A_b]$ and $[A_g A_b]$:

$$[A_b]_T = [A_b] + [A_g A_b].$$

<div align="right">Eq. 2-8</div>

As a result, the mass action law can be rewritten as:

$$[A_g A_b] = \frac{k_a [A_b]_T [A_g]}{1 + k_a [A_g]}.$$

<div align="right">Eq. 2-9</div>

When $[A_g]$ equals k_d, half the antibody binding sites are saturated (Figure 2-17).
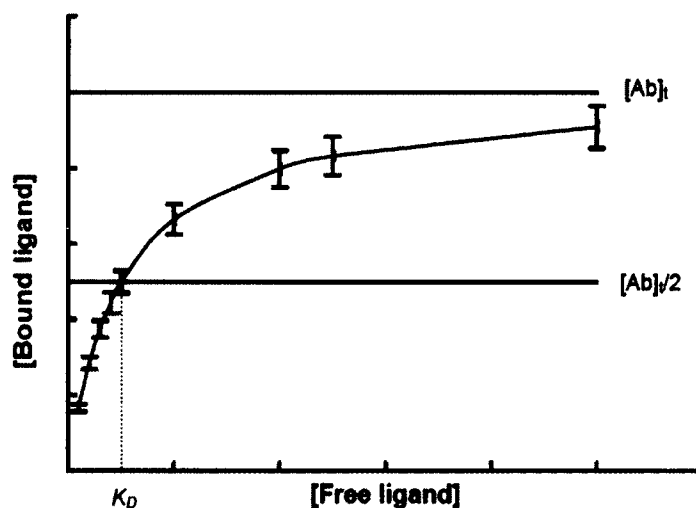
Figure 2-17. Antigen–antibody saturation binding curve [119].

2.3.3 Statistical Methods

Linear regression is one of the most commonly used statistical methods. Using linear regression to find Pearson's coefficient, we can find the relation between two variables and their closeness of fit [121].

In this research, we plot a linear regression curve to find the relation between levels of prostate cancer markers (PSA and NEM), detected using a nanopore thin film

method, and marker levels, detected using the enzyme-linked immunosorbent assay

(ELISA). Mathematically, we perform a linear regression as:

$$y = B_0 + B_1 x,$$ **Eq. 2-10**

where B_0 is the y intercept and B_1 is the slope. This is rewritten as:

$$B_0 = Y - B_1 X,$$ **Eq. 2-11**

$$Y = \sum_{i=1}^{n} \frac{y_i}{n},$$ **Eq. 2-12**

$$X = \sum_{i=1}^{n} \frac{x_i}{n},$$ **Eq. 2-13**

$$B_1 = \frac{\sum_{i=1}^{n} x_i y_i - \frac{(\sum_{i=1}^{n} x_i)(\sum_{i=1}^{n} y_i)}{n}}{\sum_{i=1}^{n} x_i^2 - \frac{(\sum_{i=1}^{n} x)^2}{n}}.$$ **Eq. 2-14**

We also use confidence of determination (R^2) to find how close the data points

are to a line of best fit:

$$R^2 = \frac{SSR}{SST},$$ **Eq. 2-15**

where SSR is the sum squared regression and SST is the sum squared total. Pearson's

coefficient is the square root of confidence of determination.

To validate nanopore thin film precision, we use the coefficient of variation

method (CV) [121], which assesses the performance of the assays.

The CV is a dimensionless numeric calculated by dividing the standard deviation

of duplicate measurements of biomolecules over a sensor at certain concentrations, i.e.,

PSA prostate cancer serum marker at concentration 160 pg/ml divided by the mean of the

duplicate measurements. If we have a poor coefficient of variation, then the error may be

caused by poor experimental techniques, such as pipetting [122], thawing and freezing,

vortexing, or centrifugation.

2.3.4 Signal Processing Techniques

To find the diffemce between two reflected signals from porous AAO sensor

surface we measured the shift that occurred on the Fabry–Perot fringes peaks (Figure 2-

18), and we compared them (Figure 2-19) with the results that generated by using cross-

correlation MATLAB code (Appendix).

The cross-correlation between two signals x and y is given by:

$$C_{xy}(\tau) = \int_{-\infty}^{\infty} x(t)\, y(t - \tau)\, dt \,,$$

<div align="right">Eq. 2-16</div>

where τ is the time shift between signals x and y.

Figure 2-18 shows the difference between the signal generated when white light is

reflected from the porous AAO nanosensor after PSA antibody immobilized (red signal),

and the signal that is generated when white light reflected from the porous AAO

nanosensor after PSA biomarker attached to PSA antibody (blue signal). The difference

between fringe peaks maxima are $\Delta\lambda1 = 7.62$ nm, $\Delta\lambda2 = 7.02$nm and $\Delta\lambda3 = 7.29$ nm. The

average of $\Delta\lambda1$, $\Delta\lambda2$, and $\Delta\lambda3$ is 7.312 nm. (The standard deviation of $\Delta\lambda1$, $\Delta\lambda2$, and $\Delta\lambda3$

= 0.3, CV= 0.041). From the cross-correlation method, the difference between both

signals is 7.4405 nm. The average wavelength shift calculated as the difference between

maxima and was highly correlated with that calculated from the cross-correlation method

(Person's coefficient = 0.901).
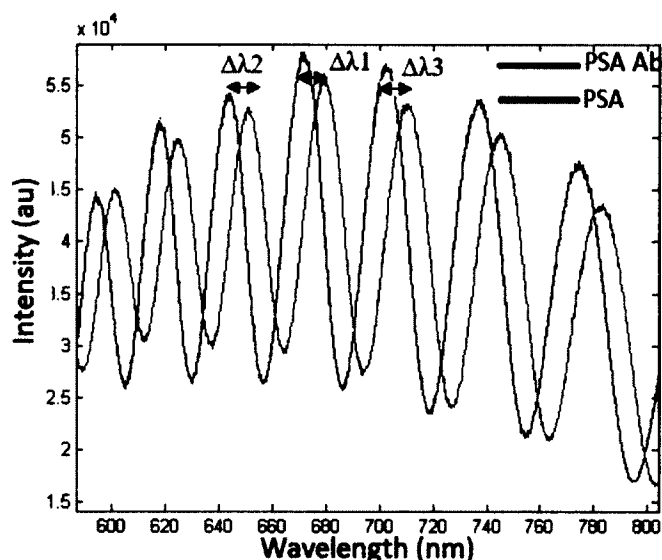
Figure 2-18. The wavelength shift between Fabry–Perot fringes (PSA antibody (red signal)) and PSA biomarker (blue signal). The average of wavelength shifts ($\Delta\lambda1$, $\Delta\lambda2$, and $\Delta\lambda3$) = 7.31 nm.
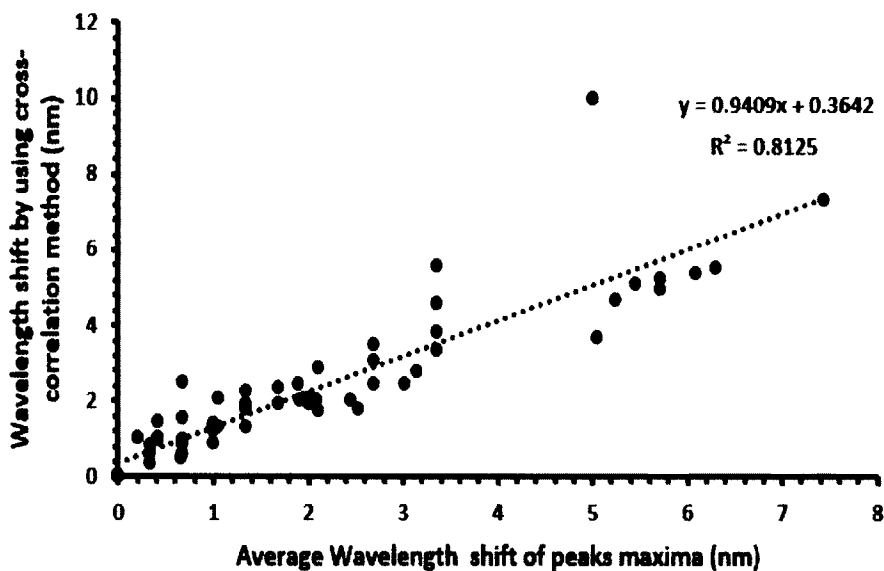
Figure 2-19. Comparison between the cross-correlation method and the peak estimating method for finding the wavelength shift between two signals (Pearson's coefficient = 0.901).

CHAPTER 3

SENSOR DESIGN AND FABRICATION

3.1   Sensor Design

Figure 3-1 shows the block diagram for the entire sensor construction process.
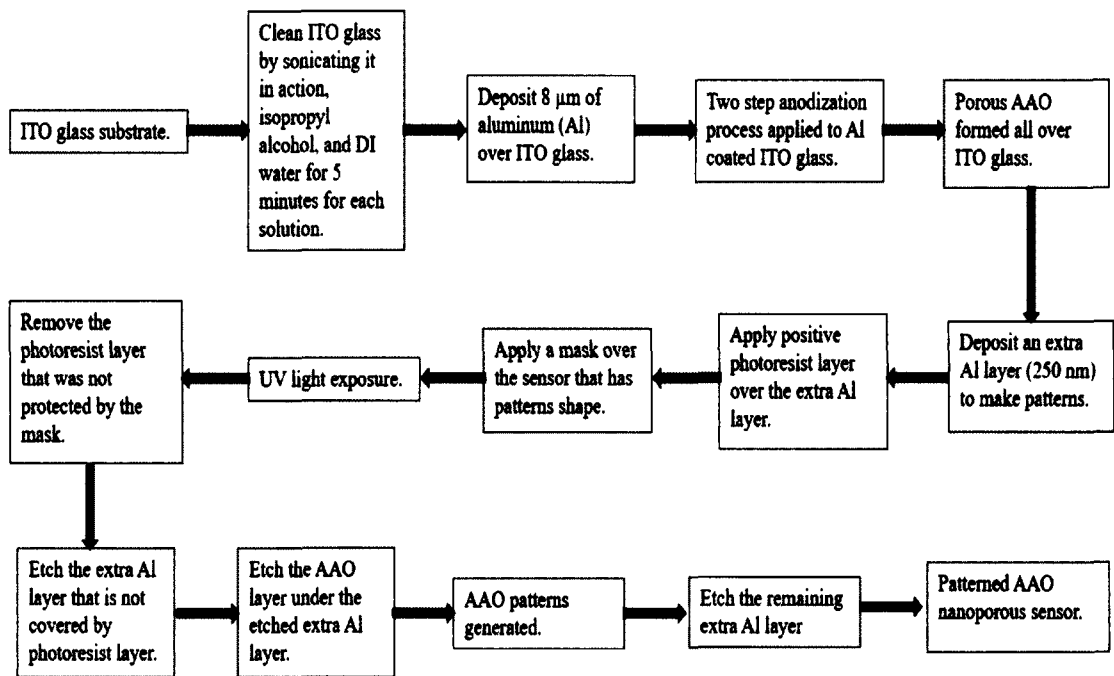
Figure 3-1. The block diagram for patterned AAO nanoporous sensor fabrication.

Anodic aluminum oxide (AAO) nanopore thin films are used in many applications, such as energy conservation and storage devices (due to its high surface area structure), nanomaterials, biosensors, and gas sensors [108]. Porous silicon surfaces with AAO thin films are used as label-free optical biosensors, although many studies show that porous silicon sensors have drawbacks, such as, rapid degradation and poor stability [72]. AAO

nanopore sensors have a vertically organized and highly ordered pore structure in a nearly hexagonal pattern [123]. AAO pore diameter is controllable and has a range of 20 nm-300 nm. Other surface characteristics, such as pore distance and pore depth, are controllable as well, with a range of 25 nm-500 nm and 1 μm-200 μm, respectively [72]. Compared with porous silicon, porous AAO sensors have greater thermal and pH stability, and greater flexibility in controlling pore structure [72, 116].

When porous AAO is used as an optical biosensor, we apply white light over the sensor surface. The reflected interference signal depends on the pore characteristics, such as diameter, length, surface adjustment, and pore wall thickness [72].

In general, an AAO membrane can have one of two morphologies that have been established based on the chemical nature of electrolytes (Figure 3-2) [124, 125]. For example, electrolytes with a pH range between 5 and 7, like oxalate, generate nonporous AAO [126]. However, acidic electrolytes, such as oxalic acid, will form porous AAO [127].
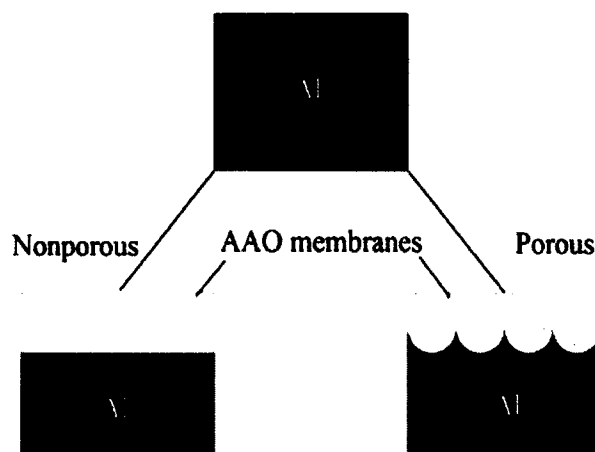
Figure 3-2. Two different AAO morphologies formed by an acidic electrolyte (porous) and a natural electrolyte (nonporous) [108].

An anodic oxide layer over aluminum has a uniform thickness and does not degrade in the electrolyte solution. During anodic oxide layer formation under constant voltage, the current density of anodization (J) decreases with time (t) in an exponential manner.

The term (J) is the summation of ionic current (J_i) and electronic current (J_e). When high electrical field (E) is applied over the oxide layer, J approximately equals J_i. As a result, the relation between J_i and E can be written as [108, 128]:

$$J_i = J_o e^{(E\beta)},$$

Eq. 3-1

where J_o and β are temperature-dependent material constants. E is a function of anodization voltage (V) and is inversely proportional to barrier thickness (t_b) as in the following relation [129]:

$$E \approx \frac{V}{t_b}.$$

Eq. 3-2

The anodic oxide layer thickness does not depend on applied anodization voltage (V) and can reach several micrometers [108]. At constant V the current density–time curve can be split into four major phases (Figure 3-3). Phase one starts directly after applying constant voltage V over an aluminum sample. At the moment V is applied, J immediately reaches a maximum value and a thin layer of oxide barrier begins to establish on the aluminum surface that has contact with the electrolyte solution.

Then, the thickness of the oxide layer increases quickly. As a result, surface resistance increases and the value of J decreases to reach its minimum value [130].
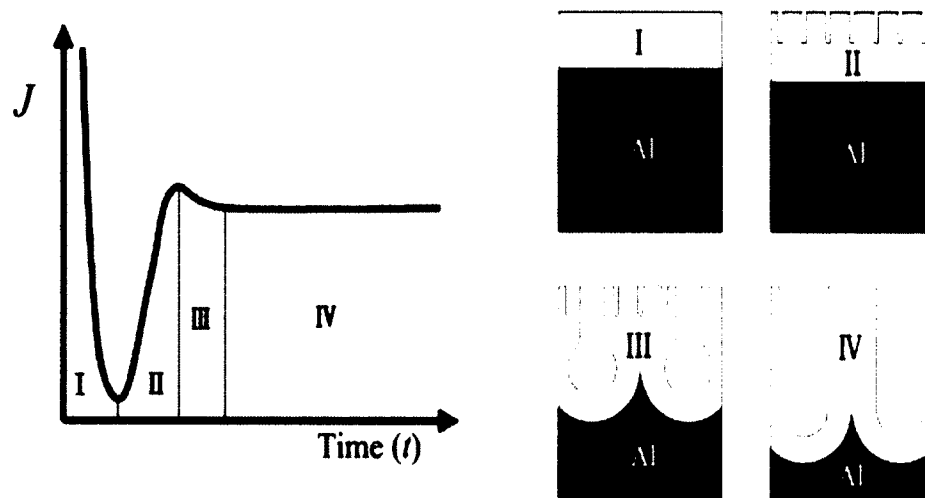
Figure 3-3. Current density of anodization versus time curve for the four phases of AAO formation under constant voltage [108].

In phase two, straight parallel-aligned initial pores form in the oxide barrier layer [130]. The mechanism of primary pore formation can be described by showing that the current density of anodization, J, attacks the weak positions at the oxide layer surface caused by cumulative tensile stress [126, 131, 132].

During phase two, some initial pores continue to grow while others stop growing. Additionally, the total surface resistance decreases in phase two, which leads to progressively increasing values of J to the regional maximum [108].

In Phase 3, pores continue growing. Finally, in Phase 4, the current density of anodization J decreases from the local maximum to a stable value and a dynamic equilibrium of a forming and dissolving anodic oxide layer is established [108, 132].

The AAO membrane has a unique unit cell structure that consists of three major parts (Figure 3-4). The first part is the skeleton of the hexagonal inner layer. This part is made by the mutual internal walls between the unit cells. The second part, which is located between the inner layer and the central pore, is called the outer layer. The last part is the internal rod, which is located inside the inner layer [108].

Porous AAO unit cell structure parameters, such as pore diameter D_p, pore wall thickness d_w, pore length l_p, pore density ρ_p, interpore distance D_{int}, barrier layer thickness t_b, and porosity P have relationships as follows:

$$D_{int} = D_p + 2d_w,$$

Eq. 3-3

$$\rho_p = \left(\frac{2}{\sqrt{3}\, D_{int}^2}\right),$$

Eq. 3-4

$$P\,(\%) = \left(\frac{\pi}{2\sqrt{3}}\right)\left(\frac{D_p}{D_{int}}\right)100\%\,.$$

Eq. 3-5

These parameters primarily depend on anodization voltage, V, anodization time, electrolyte type, and anodization process temperature [108, 133, 134].
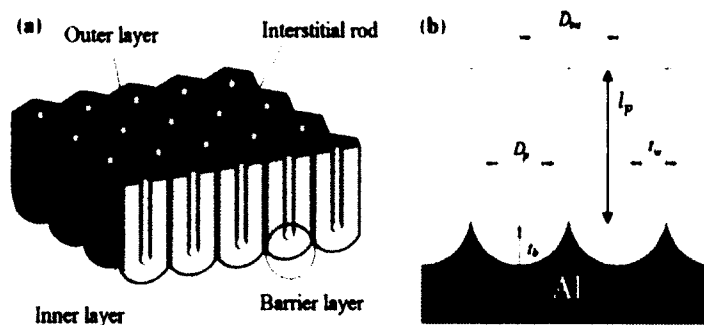
Figure 3-4. a) Porous AAO unit cell structure major parts; (b) cross-sectional view of porous AAO that shows unit cell structure parameters [108].

Pore diameter D_p, pore wall thickness t_w, and pore length l_p are the most important parameters of porous AAO and have a strong impact on reflectometric interference spectroscopy (RIfS) signals [72]. Pore diameter D_p is controlled by changing the anodization voltage [135, 136]; for example, anodization voltage of 30 V-70 V generates AAO pore diameter of 20 nm-60 nm, with pore distance ranging from 60 nm-100 nm. The relationship between D_p and the anodization voltage is linear (Figure 3-5) [72].

Pore length l_p can be adjusted by changing anodization time since pore growth is a time-dependent process. Nonetheless, the rate of AAO pore growth is not fixed at different anodization voltages; however, we can find the rate of pore length growth at constant anodization voltage (Figure 3-5) [136].
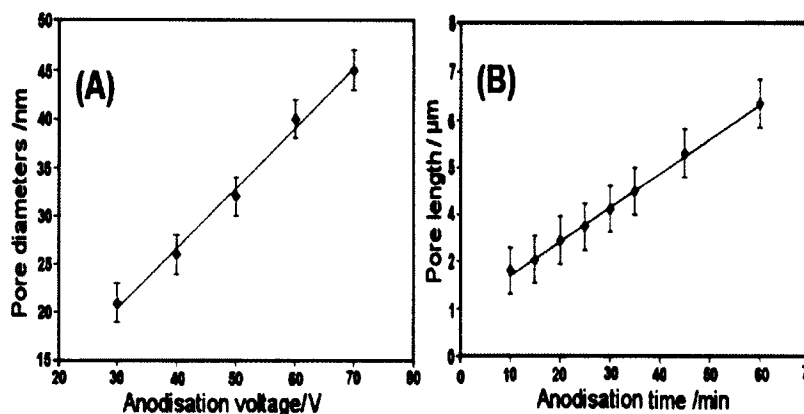
Figure 3-5. (A) Pore diameter is controlled by anodization voltage with a linear relation. (B) The impact of anodization time over pore length at constant voltage (50 V) [72].

3.1.1 The Effect of AAO Pore Diameter (D_p) on the White Light Reflected Signal

To find the relation between pore diameter and white light reflected signal, we must eliminate other parameters, such as pore length, by keeping it at a constant value.

The significant impact found was the number of Fabry–Perot fringes obtained from AAO surfaces (Figure 3-6).

The increments in the number of fringes due to pore diameter increase are measured as the increments in the number of reflected light beams from the AAO surface.

There is no typical pore diameter for a porous AAO sensor, and D_p depends on

the size of molecule to be detected. For small molecule detection, a higher shift in Fabry–

Perot fringes is expected, with better sensitivity when a small D_p is used.
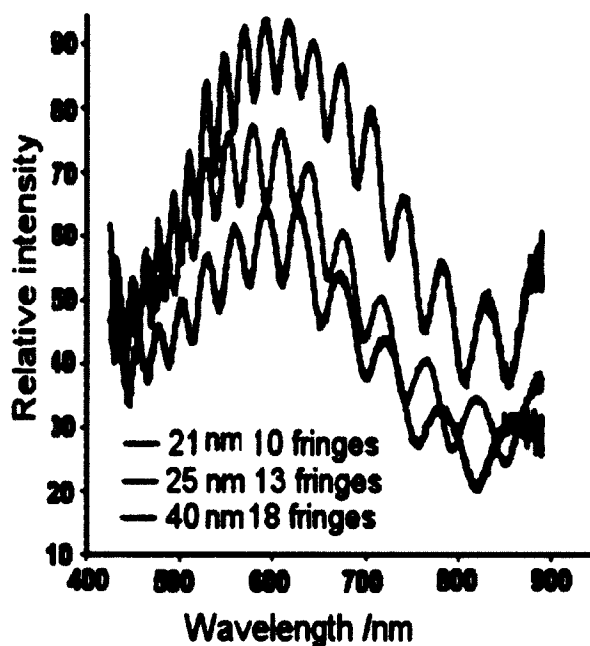
Figure 3-6. Increase in fringes as the AAO pore diameter D_p is increased from 21-40 nm [72].

Controlling D_p by changing anodization voltage affects pore wall thickness d_w and

interpore distance D_{int}. As a result, it is hard to evaluate the effect of those parameters

separately. Pore wall thickness is decreased by applying 10% wt phosphoric acid over the

AAO surface in a process called "pore widening," which is time-controlled.

Reducing the value of d_w leads to increasing in D_p (Figure 3-7). Experiments show

that after applying a widening solution over AAO for more than 65 mintues, the pore walls

are completely removed [72]. As a result, no fringes can be detected from such types of

AAO sensor surfaces.
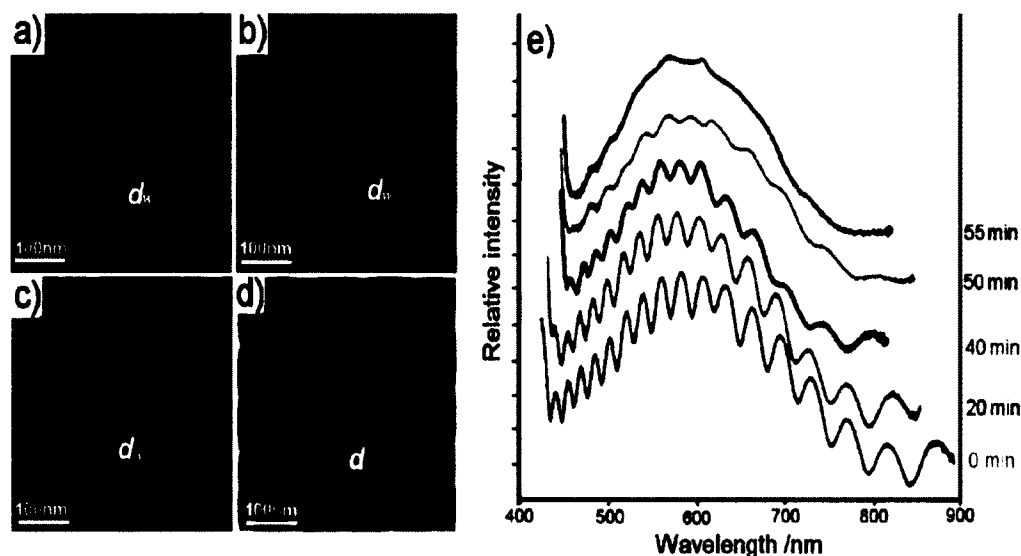
Figure 3-7. SEM images of AAO nanoporous sensor. (a) AAO sensor with $D_p = 30$ nm. d_w is decreased after applying 10%wt phosphoric acid over AAO surface for (b) 20 minutes, (c) 40 minutes, and (d) 50 minutes. (e) Obtained Fabry–Perot fringes during the pore-widening process [72].

3.1.2 The Effect of AAO Pore Length (l_p) on the White Light Reflected Signal

Pore length l_p of AAO has the same effect on the white light reflected signal as AAO pore diameter D_p. The Fabry–Perot interference fringe patterns increase as l_p increases (Figure 3-8). AAO, with l_p less than 2.5 µm, shows few or no Fabry–Perot interference fringe patterns. The best l_p range to have significant number of fringes with high intensity is 2.5 µm–5 µm. When l_p is more than 5 µm and less than 10 µm, the number of fringes increases; however, this increase affects the intensity of the signal by decreasing amplitude intensity, thus making it hard to analyze the generated signal. If l_p is more than 10 µm, then fringes will be very small ("baby fringes"). For AAO with l_p more than 12 µm, no fringes are observed using RIfS. The relation between the increasing number of fringes and changes to intensity by increasing l_p can be clarified by the increment in the number of reflected light within AAO pore, which leads to more

fringes. However, the light intensity is reduced due to lost energy caused by multiple

light-trapping inside the AAO pore [72].
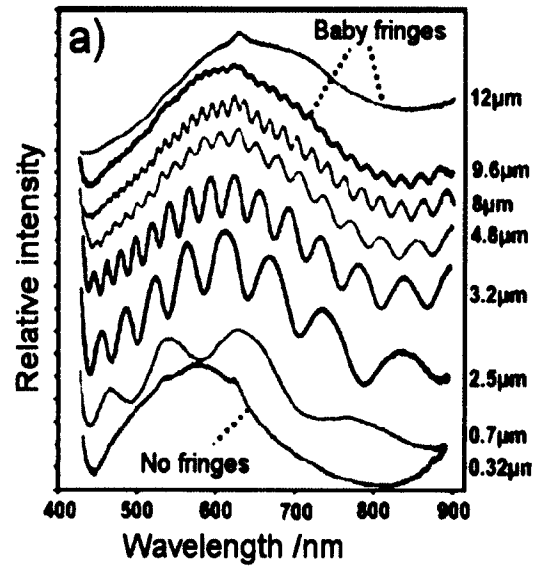
Figure 3-8. Relation between pore length l_p and the white light reflected signal over the AAO sensor surface. At l_p less than 2.5 μm, few fringes are generated. With increased l_p, the number of fringes is increased with decreasing reflected signal intensity [72].

3.1.3   The Effect of AAO Pore Surface Modifications

The reflectivity of the AAO sensor surface affects both the light reflectance from

the surface and the interference signal [137]. Coating our sensor surface with ultra-thin

metal modifies the fringe shape and the reflected signal intensity (Figure 3-9).
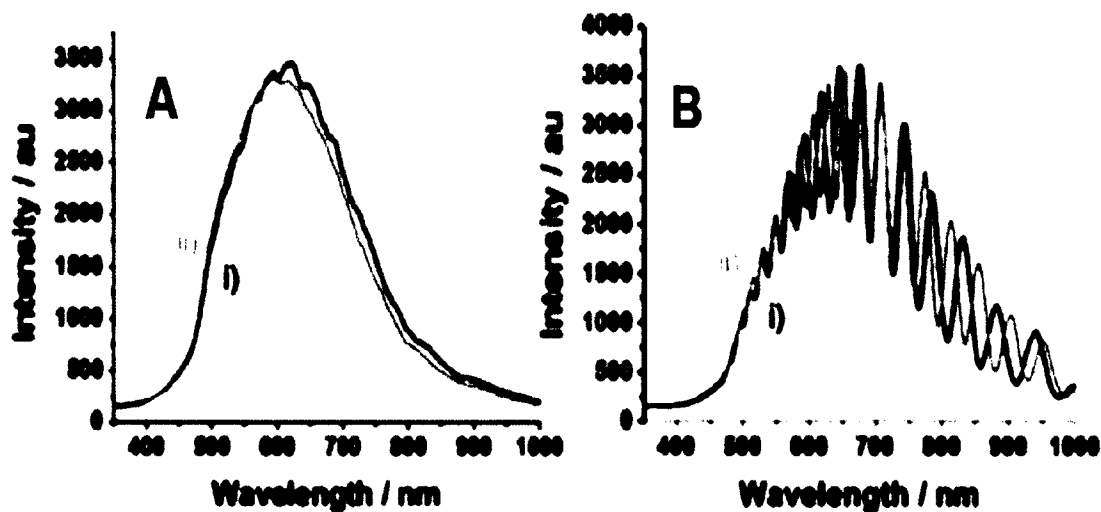
Figure 3-9. Improvement of reflected signal before and after coating AAO sensor with gold. (A) Reflected signal from non-gold-coated AAO sensor surface before (black line) and after (red line) applying biomolecules. (B) Reflected signal from gold-coated AAO sensor surface before (black line) and after (red line) applying biomolecules. Compared with B, it is hard to find the difference between the two reflected signals from the gold and non-gold-coated AAO sensors [108].

Many metals are used as a coating layer over AAO top surfaces, such as gold, silver [78, 138], platinum [72], and copper [139, 140]. Gold (Au) is the most common metal used to make a thin layer AAO sensor surface [78] because it is inert and does not form any oxide layer below its melting temperature [141], Au provides excellent chemical stability to the sensor surface.

One more advantage that makes Au more attractive as a surface coating is the ability to make extraordinary contact with alkanethiols, which are the building blocks of the self-assembled monolayer [101, 142, 143].

The best enhancement of the reflected signal occurs when the thickness of the gold surface coating is between 4 nm and 10 nm. A gold layer with a thickness of more than 10 nm will not enhance the signal.

After the AAO is coated with gold, the pore diameter is reduced. Au thickness,

therefore, is optimized to ensure the gold does not block the sensor pores. This research

uses an AAO sensor with the following characteristics:

Pore diameter D_p = 55 nm, pore length l_p = 5 μm, pore density = 5.5 × 10^9 pores per cm^2,

pore period = 145 nm, poricity = 34.4%, and Au coat thickness = 5 nm.

3.2   AAO Sensor Fabrication

We use indium tin oxide (ITO) glass (Nanocs, Inc., IT100-111-25) to fabricate a

patterned AAO sensor (Figure 3-10). ITO glass is used because it is a conductive material

(sheet resistance value100 Ω/square) and helps transport electrical current through the

surface smoothly [144]. Patterned AAO sensor fabrication goes through three major

steps: anodization, photolithography, and etching.
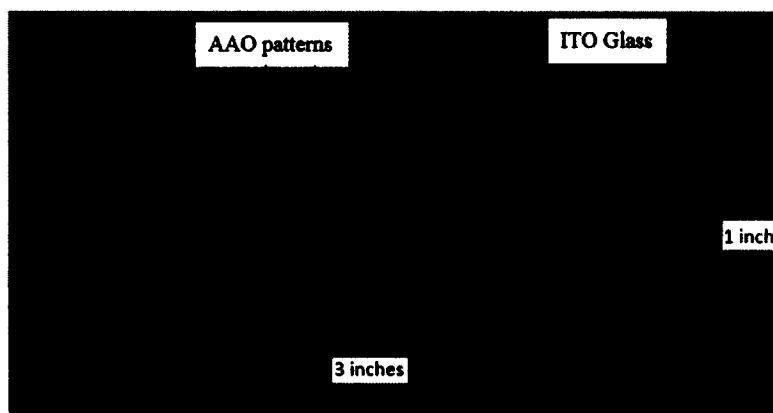
Figure 3-10. Fabricated AAO patterns over ITO glass.

3.2.1   AAO Sensor Fabrication

The first step in the anodization process is to wash the ITO glass by sonication for

five minutes in deionized (DI) water, then five minutes in acetone, followed by five

minutes in isopropyl alcohol, and finally, sonication for five minutes in DI water again. Then we bake the cleaned ITO glass for five minutes.

In the next step, we deposit an aluminum layer with a thickness of 8 μm over the ITO glass surface using an E-beam evaporation device. We consider surface smoothness after the aluminum layer is deposited, since it is a significant factor in the fabrication process [145, 146].

After that, two anodization processes (Figure 3-11) are applied to the aluminum-coated ITO glass.
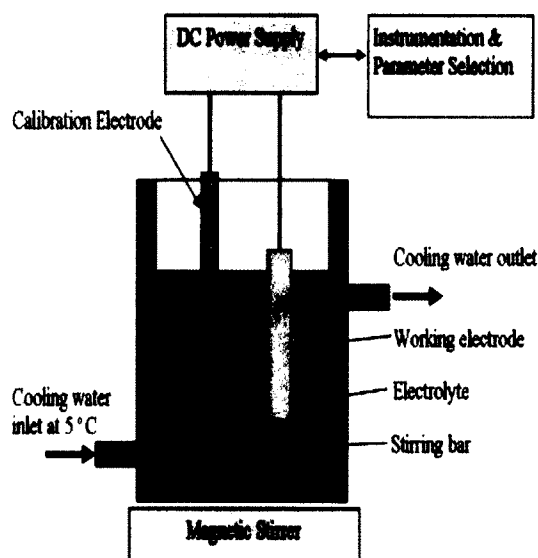
Figure 3-11. Schematic of two-step anodization instrument [147].

During anodization, a chemical reactions take place. The chemical reaction during alumina (Al_2O_3) formation is:

$$2Al + 3H_2O \leftrightarrows Al_2O_3 + 6H^+ + 6e^-.$$ **Eq. 3-6**
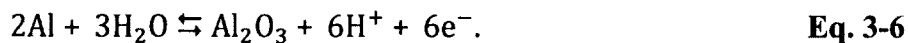
Part of Al_2O_3 at the alumina—electrolyte interface is dissolved by the following reaction:

$$Al_2O_3 + 6H^+ \rightarrow 2Al^{+3} + 3H_2O.$$ **Eq. 3-7**

At the barrier layer, aluminum will dissolve:

$$2Al \rightarrow 2Al^{+3} + 6e^-.$$ **Eq. 3-8**
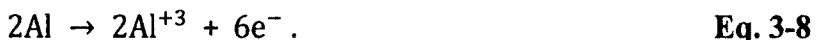
At the cathode, hydrogen gas (H_2) will develop:

$$6H^+ + 6e^- \rightarrow 3H_2.$$ **Eq. 3-9**
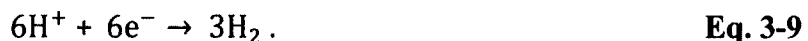
The two-step anodization process procedure is as follows. First, we apply the Al-coated ITO glass inside the anodization device (Figure 3-11) for 10 minutes with 0.3 M oxalic acid as the electrolyte and apply DC voltage (45 V) at 2 °C. This process is called step-one anodization. Second, we etch the sample using 0.2 M chromic acid and 0.4 M phosphoric acid at 65 ◻ . At this stage, no voltage is applied. Finally, the nanopores are developed in step two anodization and etched in 0.3 M oxalic acid for 40 minutes under the same conditions applied in step one anodization. After the two-step anodization process is complete, we rinse the achieved AAO sensor (Figure 3-12) with DI water.

Figure 3-12. SEM of porous AAO sensor surface.

3.2.2 Photolithography

Since the whole surface of the ITO glass will be covered by a porous AAO layer by the end of the two-step anodization, photolithography is applied to make a patterned AAO device.

We start the photolithography process by depositing a thin film of aluminum (150 nm thick) over the porous AAO surface by thermal evaporation. Then, a positive photoresist (AZ 1512) is applied to the sensor surface and spin-coated at 4,000 rotations per minute (rpm), followed by soft-baking for 50 seconds at 95 °C.

Afterwards, patterns are transferred to the photoresist layer by applying a 416 nm light at an exposure dose of 70 mJ/cm^2 through a photomask, followed by baking for 50 seconds at 105 °C.

The photoresist layer not covered by the photomask during light exposure is removed by submerging the sample in an AZ developer for 25 seconds. By this step, patterns are implanted over the AAO sensor surface at the spots protected by the photomask.

3.2.3 Etching

The etching process starts when we apply the sample in an aluminum etching solution for 35 seconds. This step removes the unprotected Al layer. The etching solution consists of H_3PO_4: CH_3COOH: HNO_3: H_2O (80:5:5:10 by weight %).

Then, the unwanted AAO layer is etched out by submerging the sample in a mixture of 0.2 M chromic acid and 0.4 M phosphoric acid for 1.5 hours.

Finally, we remove the remaining photoresist using acetone and etch out the deposited aluminum layer using an aluminum etching solution. The patterned AAO fabrication process is showen in Figure 3-13.
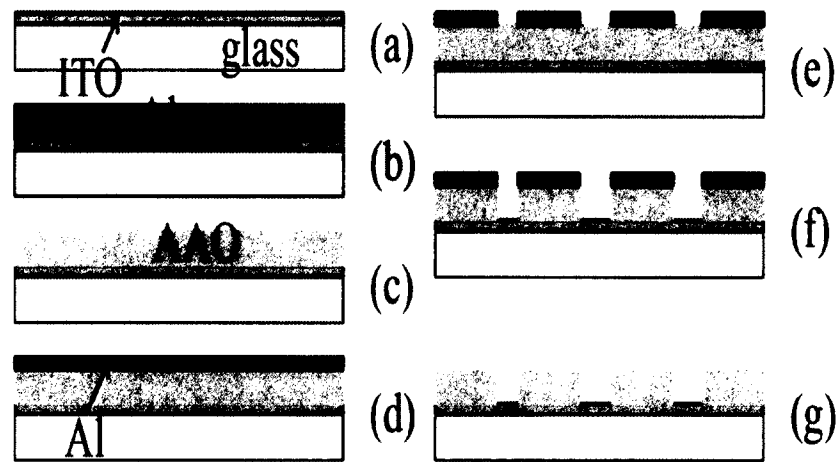
Figure 3-13. Patterned AAO fabrication process. (a) Clean ITO glass. (b) Deposit aluminum thin film. (c) AAO generated after two-step anodization process. (d) Deposit another aluminum layer to create patterns and apply photoresist layer and light exposure through a photomask. (e) Etch unprotected aluminum layer using an aluminum etching solution. (f) Etch unwanted AAO layer. (g) Remove photoresist layer by action and etch the second deposited aluminum layer.

After the fabrication process is completed, we coat the sensor with a 50-Å gold layer. To evaluate if our sensor is fabricated precisely, we apply white light over the sensor surface and observe the reflected signal generated (Figure 3-14). A poorly fabricated sensor generates low-intensity fringe signals and sometimes no fringe signal, whereas a well-fabricated sensor will produce bright fringes with high amplitude.
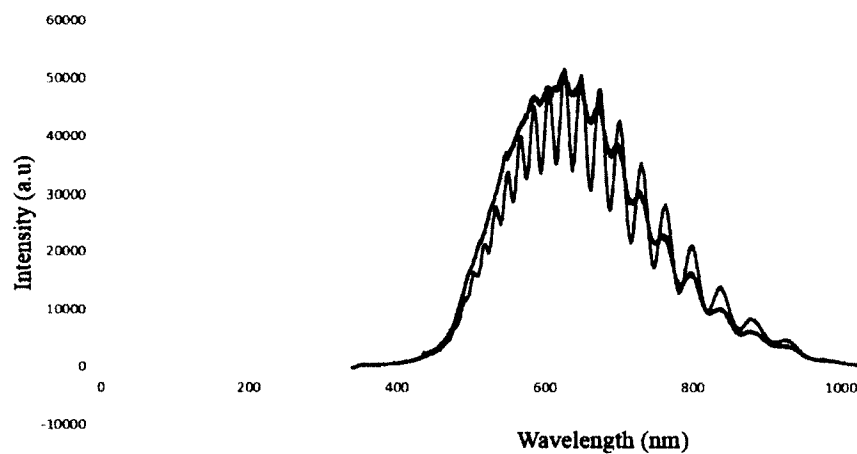
Figure 3-14. Well-fabricated AAO sensor (red line) versus poorly fabricated AAO sensor (blue line). Fringes generated by a well-fabricated sensor have better reflected intensity than those produced by a poorly fabricated sensor.

CHAPTER 4

PROSTATE CANCER BIOMARKERS DETECTION

4.1   Experiment Protocol

The flow chart of the experimental setup is shown in Figure 4-1.

Emitted light through
optical probe

| White light source | → | Nanopore thin-film sensor (the specimen to be tested is immobilized over sensor surface) |

Reflected light
collected by
optical probe

| Data analysis system | ← | Spectrometer |

Optical
transducing
signal
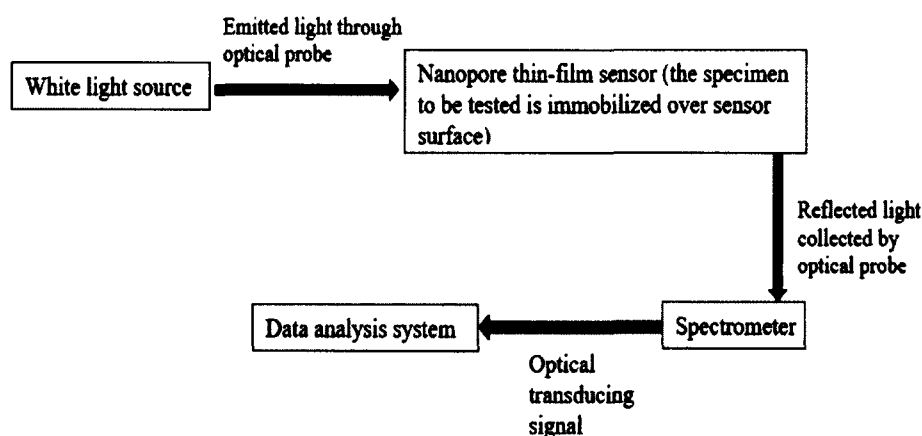
Figure 4-1. Flow chart of the experimental setup.

4.1.1   Antibody Immobilization and Antibody Detection

The gold-coated AAO surface was first cleaned with O_2 plasma for 15 minutes.

This step was followed by a self-assembled monolayer (SAM) process (Figure 4-2), in

which the sensor is incubated in a mixture of 1 mM HSC10COOH and HSC8OH with a

molar ratio of 1:10 in absolute ethanol solution overnight. The SAM was activated by

incubation in phosphate buffer solution (PBS; 10 mM, pH 7.0) containing 0.5 mM of

EDC/NHS for 2 hours. The activated SAM was rinsed with the 10 mM PBS, and then

incubated with a freshly prepared 10 mM PBS solution containing 10 µg/ml of the

detector mAb for 18 hours at 4 °C. The device was then rinsed with the PBS, followed by

0.2 M glycine-PBS solution for 10 minutes to deactivate the remaining active sites at the

SAM. This step avoided non-specific binding between the SAM and the antigens. It was

followed by measuring the reflected single from the sensor surface after the antibody

immobilized. Then, different concentrations of biomarker solution was applied to the

antibody-coated AAO sensors and incubated for 60 minutes at room temperature. Then,

the sample was rinsed with PBS to wash away unbounded biomarker molecules. This

step was followed by measuring the reflected single from the sensor surface after

biomarkers applied. Finally, we measured the shift of the optical fringes for each sensor.
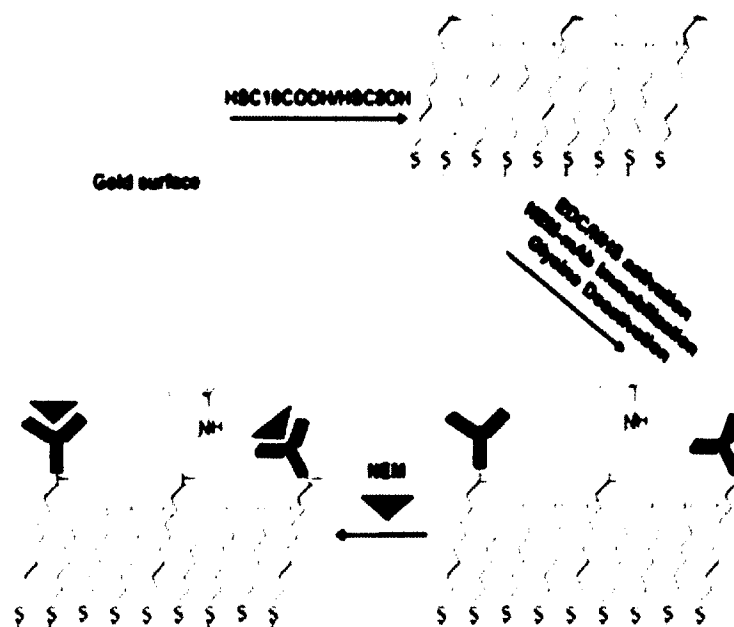
Figure 4-2. Illustration of the protocol for the self-assembled monolayer (SAM) formation on the Au-coated AAO surface, antibody (Ab) immobilization and NEM detection.

4.1.2   Nanosensor Surface Functionalization and Characterization

The nanosensor was subjected to a step-by-step surface functionalization

procedure of the Au-coated AAO surface. This well-established method allows the

formation of a mixed SAM of alkanethiols by the adhesion reaction of the thiol group on

the Au-coated surface [148]. After EDC/NHS is added on the surface, the carboxylic

groups of amine-reactive intermediate is formed. Due to their positive charge at

physiologic conditions, primary amines are usually the outward-facing components of the

proteins. Hence, they are generally accessible for conjugation without denaturing the

protein structure. As a result, the detector mAbs for NEM or PSA can be covalently

attached to the top of the mixed SAMs. In order to eliminate or mitigate the non-specific

biological binding, the remaining active amine-reactive intermediate groups are

deactivated by the amino acid glycine. Thereafter, the mAbs are conjugated to the

nanosensor surface and ready for detecting NEM or PSA.

4.2   Nanosensor Validation

For the validation of the nanosensors, key assay parameters such as specificity,

sensitivity, accuracy, and precision were critically evaluated as per the requirements of

international guidelines [149, 150]. First, we tested whether the presence of a high

concentration of unrelated protein(s) influences the binding between the detector

antibody and the sensor. We compared the binding of NEM mAb or PSA mAb with the

sensor in the presence/absence of BSA (0.15 mg/ml). Second, multiple sensors were used

to determine the standard curve for NEM or PSA, and the results of different batches of

sensors were compared to ascertain the reproducibility of the sensors. Third, aliquots of

human serum samples were tested in multiple dilutions to determine the upper and the

lower serum volume detection limits. All samples were tested in duplicate and only the

results with a coefficient of variation (CV) <20% were accepted.

Sensor efficiency: To determine the accuracy of nanosensor measurements, known amounts of NEM or PSA antigens were added into pooled serum aliquots. The amount of the antigen(s) determined by nanosensors was compared with the expected amounts of antigen.

Comparison of nanosensors with ELISA: The serum samples left over from an earlier study [115] that used ELISA to detect the antigens were used in nanosensor assays. The results from both studies were compared by using Pearson's correlation method.

Comparison of the detection ability of NEM and PSA by using nanosensor tests applied to pathologically confirmed prostate cancer blood serum samples (cancer blood serum samples and negative control blood samples were provided from ULM College of Pharmacy).

We used one site-specific binding (Y) equation to generate standered curves (Figure 4-3) for antibodies and biomarkers. To use this equation, we must have already subtracted off any nonspecific binding. At high biomarker concetration, all of the binding sites become occupied. As a result, the standard curve reached the saturation point.

$$Y = \frac{B_{max}X}{k_d + X},$$ Eq. 4-1

where X is the concentration of the ligand, B_{max} is the maximum binding in the same units as Y, and k_d is the dissociation constant.

After we generated the standered curves, we converted the x-axis into a logarithmic (Log_{10}) scale to find the linear region of the curve.
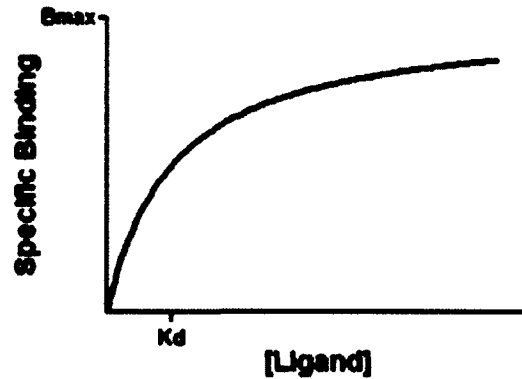
Figure 4-3. One site-specific binding saturation curve.

4.2.1 Antibody Optimization

Before we start detecting biomarkers, we selected the antibody concentration that we are going to immobilize over porous AAO sensor surface. This step is important because all experiments should be applied under the same conditions.

To optimize NEM antibody (Figure 4-4), we immobilized different NEM antibody concentrations over different porous AAO sensors, and we measured the reflected signal from porous AAO sensor; then we applied fixed concentration of NEM biomarker (8 pg/50 μl) over the sensors. After 60 minutes of incubation, we measured the reflected signal again and calculated the wavelength shift between antibody signal and biomarker signal.
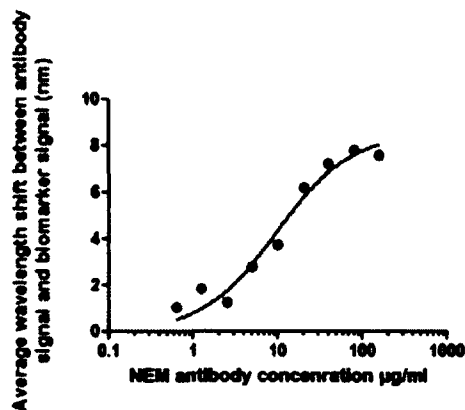
Figure 4-4. NEM antibody optimization.

To optimize the PSA antibody (Figure. 4-5), we used the same method of NEM antibody optimization.
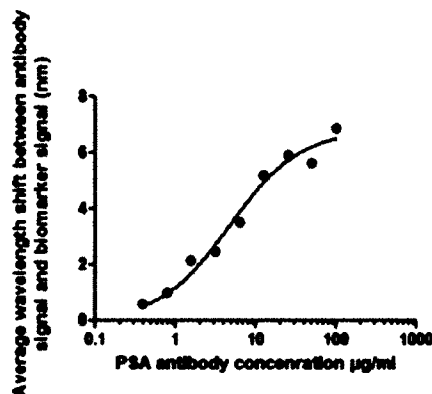
Figure 4-5. PSA antibody optimization.

When the concentration of antibody is increased, the shift between antibody signal and biomarker signal is increased. The selected concentration of PSA and NEM antibodies is 10 μg/ml.

4.2.2 Porous AAO Nanosensor Detecting Limits

After we selected the concentrations of PSA and NEM antibodies, we will measure the lowest and the highest concentration of NEM (Figure 4-6) and PSA (Figure 4-7) biomarkers that porous AAO sensor can detect. NEM biomarker concentrations tested were 0, 0.025, 0.05, 0.1, 0.2, 0.4, 0.8, 1.6, 3.2, 6.4, 12.8, 25.6, 51.2 and 102.4 pg/50 μl. The lowest concentration of NEM detected by AAO porous nanosensor was 0.1 pg/50 μl (2 pg/ml), and the curve reaches the saturation point at 25.6 pg/50 μl (0.512 ng/ml). For PSA, the lowest concentration detected by AAO porous nanosensor was 1 pg/50 μl (20 pg/ml), and the curve reaches the saturation point at 50 pg/50 μl (1 ng/ml).
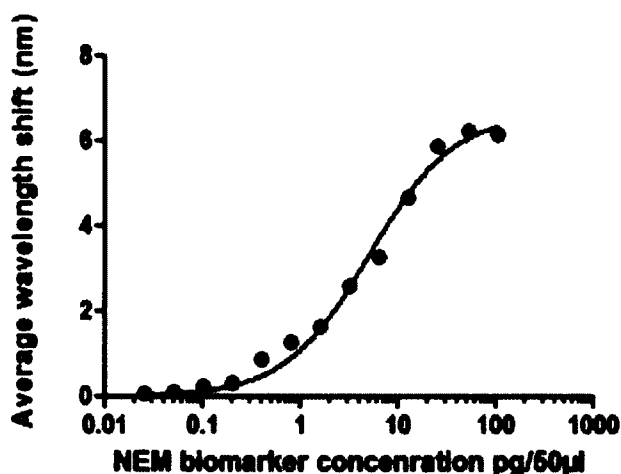
Figure 4-6. NEM biomarker detection limits by using porous AAO nanosensor. The lowest concentration and the highest concentration detected were 0.1 pg/50 μl and 25.6 pg/50 μl, respectively.
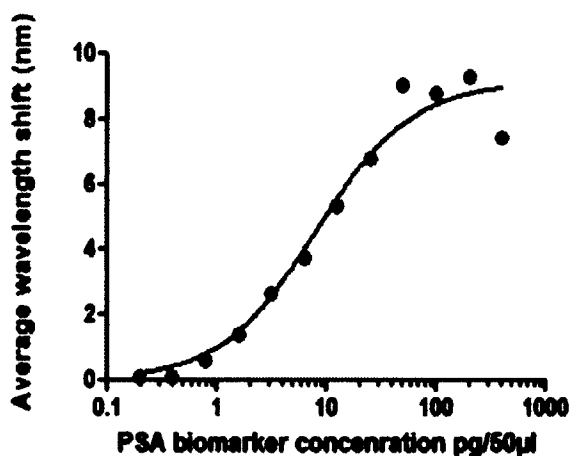
Figure 4-7. PSA biomarker detection limits by using porous AAO nanosensor.

4.2.3 Biomarkers Standard Curves

To generate a standard curve for NEM and PSA biomarkers, different concentrations of NEM and PSA were prepared from stock solution. NEM and PSA concentrations in stock solution are 5 mg/ml and 1 mg/ml, respectively.

The concentrations that we prepared to generate standard curves were 32, 16, 8, 4, 2, 1 and 0 pg/50 μl for PSA (see Figure 4-8), and 16, 8, 4, 2, 1, 0.5 and 0 pg/50 μl for NEM (see Figure 4-9). All diluted solutions were prepared by using serial dilution

method. PSA and NEM standard curves show the relationship between biomarker

concentration and wavelength shift between the signal that generated from antibody

coated sensor surface and the signal that generated after antigen-antibody complex

formed. The relation between biomarker concentration and wavelength shift is nonlinear;

to approximate it as a linear relationship, the x-axis scale is changed to a logarithmic

(Log_{10}) scale.
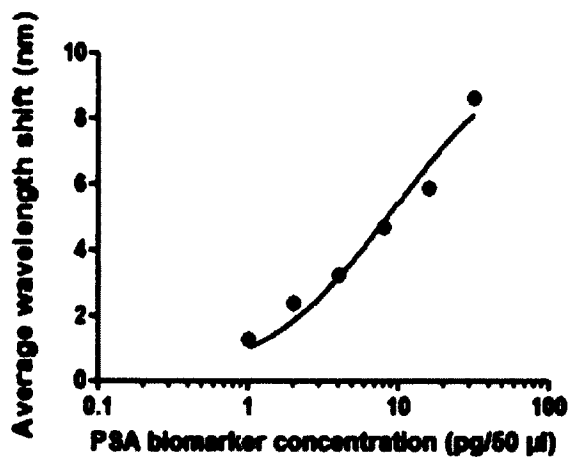
Figure 4-8. PSA standard curve.
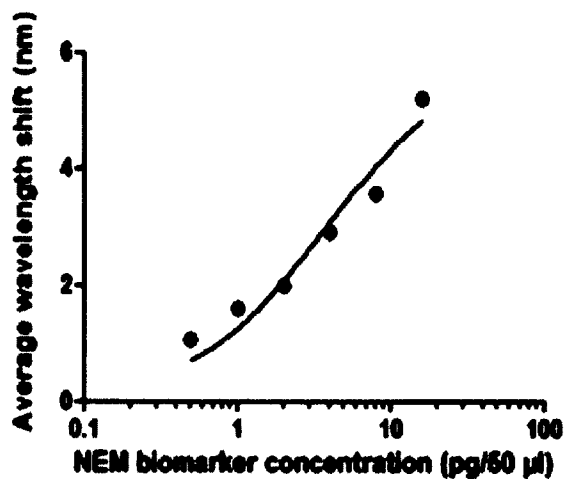
Figure 4-9. NEM standard curve.

4.2.4 Reproducibility

To test the reproducibility of the nanosensors, the assays with normal standard

curves were performed on three randomly selected sets of chips and run under the same

conditions on three different days. Figure 4-10 demonstrates the reproducibility of the

response. The standard deviation over the mean of each point were 0.08 at 1 pg, 0.12 at 2

pg, 0.09 at 4 pg and 0.13 at 8 pg for NEM.
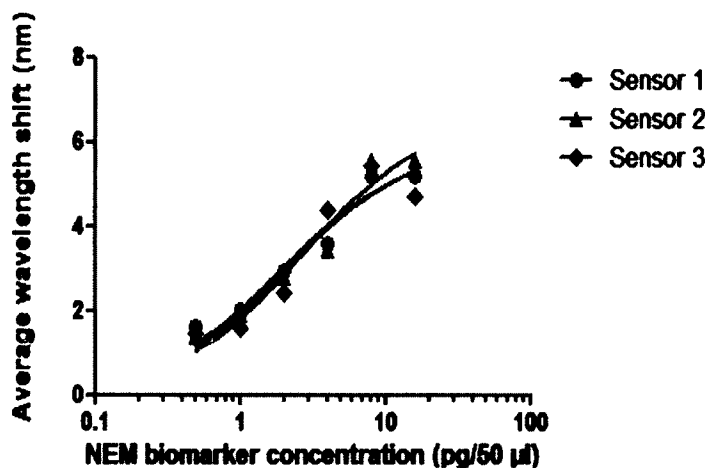
Figure 4-10. NEM standard curves using three separate sets of sensors on different days.
Sensors 1, 2, and 3 were the fabricated AAO nonporous thin film (Figure 3-9).

4.2.5 Specificity

To test the specificity of this detection method, we compared the shift of the

fringes when NEM solution was applied to the sensor versus concentrated bovine serum

albumin (BSA) solution (15 mg/ml). After 1 hour incubation, the sensor was rinsed with

PBS buffer. The measurements in Figure 4-11B demonstrate no clear shift of the

transducing signals before and after the BSA applied. In contrast, NEM solution gave a

clearly observable shift (Figure 4-11A), demonstrating that the sensor can specifically

detect the antigen even in the presence of large protein concentrations as long as the

antibody is specific. Also, we applied NEM biomarker over PSA mAb and PSA over

NEM mAb to check if any unspecific binding occur (Table 4-1).

The results indicated no shift of the fringes when NEM biomarker was applied

over PSA mAb, or when we applied PSA biomarker over NEM mAb.

Table 4-1. Specificity test.

Sample tested	Average wavelength shift (nm)
PSA antibody (5 µg/ml) + NEM biomarker (8 pg/50 µl)	0.14
PSA antibody (2.5 µg/ml) + NEM biomarker (8 pg/50 µl)	0.067
NEM antibody (10 µg/ml) +PSA biomarker (2 pg/50 µl)	0
NEM antibody (10 µg/ml) +PSA biomarker (4 pg/50 µl)	0.047
NEM antibody (10 µg/ml) + BSA (1.5 mg/ml)	0.107
NEM antibody (10 µg/ml) + BSA (0.15 mg/ml)	0.075
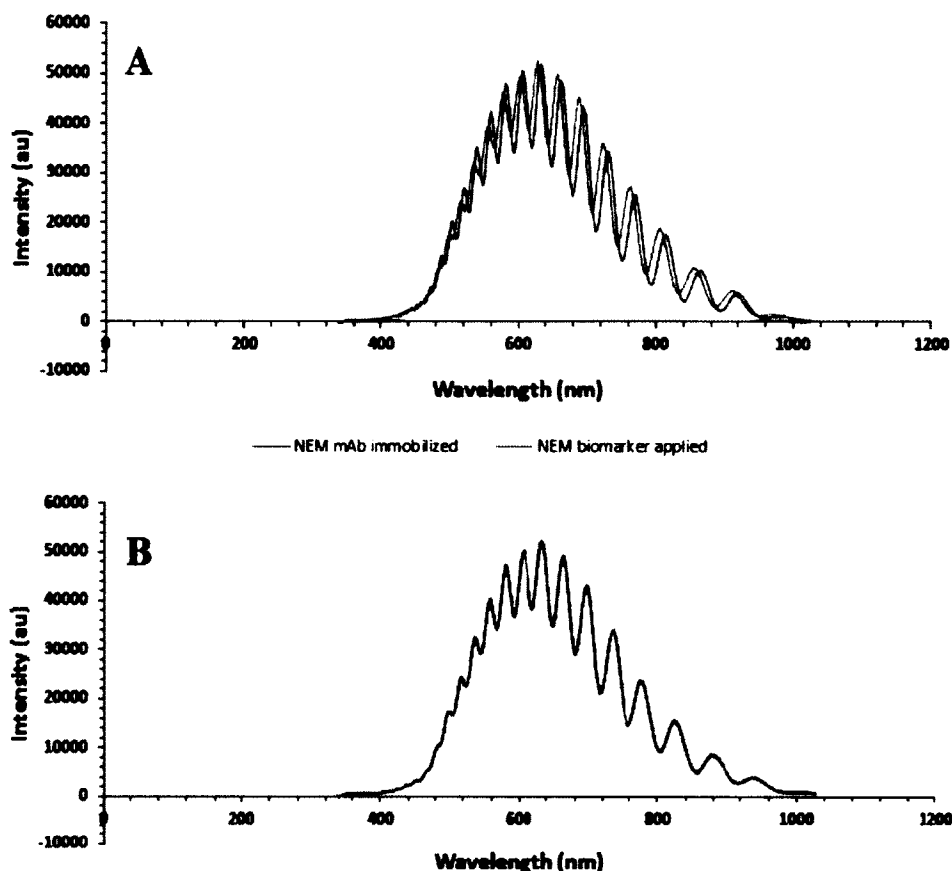
Figure 4-11. (A) Typical transducing signals (average shift of interference fringes 4.81 nm) from the optical sensor after the NEM (16 pg/50 µl) is applied, incubated, and then rinsed using the buffer solution PBS in the sensor. (B) Specificity and selectivity test: transducing signal from the sensor after BSA solution is flowed, incubated, and then rinsed using buffer solution PBS in the sensor is negligible (average shift 0.017nm).

4.2.6 Accuracy

To test the accuracy of nanosensor, we prepared pools of sera obtained from normal subjects and added known amounts of antigen (either NEM or PSA). We then measured the concentrations of NEM or PSA in all pooled sera in the same assay (Table 4-2). The detected value of added antigen was determined. The accuracy (the ratio of measured amount to calculated amount) of the detection of the known amounts of added antigen varied from 93% at the lowest added concentrations (1 pg added PSA) to 76.7% at the highest added concentration (4 pg added PSA).

Table 4-2. Accuracy test.

Tested sample	Average wavelength shift (nm)	Calculated PSA amount (pg)	Measured PSA amount (pg)	Accuracy %
0.5µl serum + 49.5µl PBS	0.504	0.978	0.978	
0.5µl serum + 1pg PSA + 48.5µl PBS	0.898	1.978	1.84	93
0.5µl serum + 2pg PSA + 47.5µl PBS	1.215	2.978	2.64	88.6
0.5µl serum + 4pg PSA + 45.5µl PBS	1.565	4.978	3.82	76.7

4.2.7 Comparison of NEM Nanosensor Assay with NEM ELISA

We then compared our earlier NEM ELISA standard curve (Figure 4-12a) with

the NEM nanopore thin-film sensor standard curve (Figure 4-12b). To generate NEM

ELISA standard curve ELISA microtiter plates were coated with 23 ng NEM antibody

per well overnight at 4 °C, followed by washing of the plates and the addition of BSA

solution (2%) as blocking solution. Then the samples were added and incubated for one

day. The next day, the biotinylated NEM was added to the wells and incubated for 3

hours at 37 °C. After that, we added and incubated streptavidin-horseradish peroxidase

conjugate [164] for an hour at 37 °C. Finally, chemiluminiscence was read on a plate

reader. The results suggest that the nanopore thin-film was approximately 50 fold more

sensitive than the corresponding non-equilibrium ELISA. When considered together with

the simplicity of the method, label-free assay, and a very short incubation period of 60

minutes, the nanopore thin-film sensor offers significant advantages over the ELISAs for

biomarker measurements.
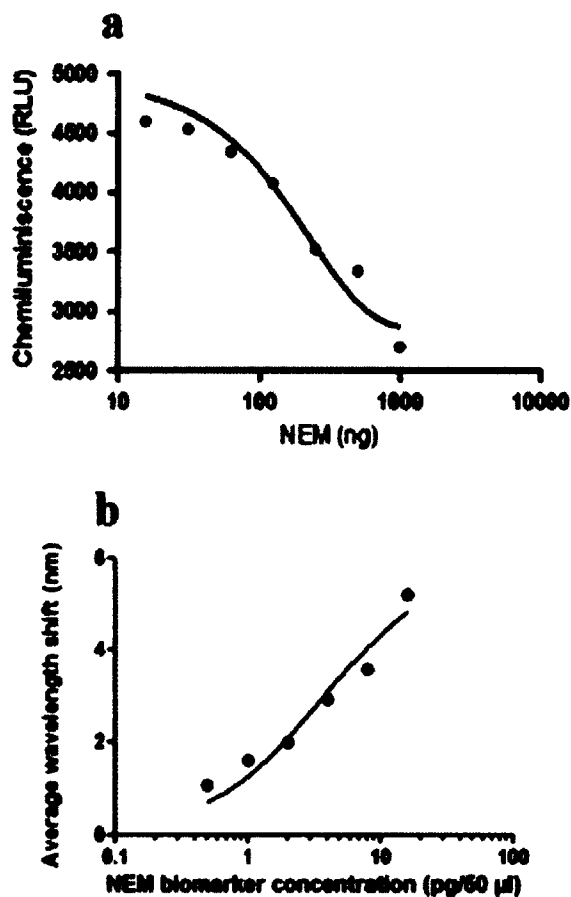
Figure 4-12. Comparison between immunosensor assay and ELISA: (a) a typical standard curve of NEM in an ELISA assay [65]; (b) a typical NEM standard curve by using porous AAO nanosensor.

4.2.8 Blood Serum Dilution Curve

Before we tested human blood serum, we found out the minimum and the

maximum serum volume that porous AAO sensor can detect (Figure 4-13). The serum

volumes tested were 0.3, 0.6125, 1.25, 2.5, 5, 10, and 20 μl of blood serum in total buffer

solution with volume of 50 μl. The minimum blood serum volume detected was 0.125 μl

and the saturation point was approximately at 4 μl.
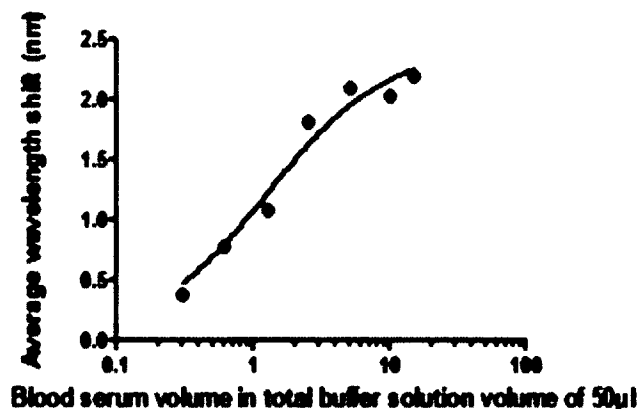
Figure 4-13. Human Blood serum dilution curve. The saturation point is at 4 μl blood serum volume.

4.2.9 Assay Validation with Human Serum Samples

We then analyzed 10 different serum samples from 10 different patients who visited the urology clinic for either BPH or PC leftover from the earlier study [151]. The protocol for the use and analysis of the sera was approved by the Institutional Review Boards (IRB) at University of Louisiana at Monroe (ULM).

The freezed blood serum samples were thawed in an ice bath; then, we vortexed the samples and centrifuged them for 20 seconds, followed by taking 2 μl of the serum by using micropipette and adding it into 398 μl of PBS. The serum NEM and PSA results obtained by the porous AAO nanosensors were then compared with those obtained by NEM and PSA ELISA (Figure 4-14). Serum NEM/PSA values determined by the sensor were highly correlated with those determined by the ELISA (for NEM, Pearson Coefficient: 0.9507, for PSA, Pearson Coefficient: 0.9431). More importantly, all PC samples with > 4 ng/ml PSA (PSA < 4 ng/ml serum are considered non-cancer whereas PSA > 4 ng/ml serum are considered as potentially cancer) were also predicted to be the same by the current porous AAO nanosensor. Then, the NEM and PSA levels measured by the sensors in these samples were compared with the clinicopathological status of the

patients (Figure 4-15). As expected, confirmed PC patients (Sample numbers #4, #6, #9) displayed high PSA (>4 ng/ml) as well as NEM (>4 ng/ml) levels (see Table 4-3). Among the remaining patients, we observed some divergences between NEM and PSA levels. For example, patients #7 and #10 displayed 4.59 and 4.39 ng PSA/ml respectively (Table 4-3). Based on the current cut-off, these patients are considered as potential cancer patients. However, their NEM levels were low (1.762 and 2.096 ng/ml respectively) (Table 4-3). In contrast, patients #1 and #2 displayed normal PSA levels (2.46 and 2.20 ng/ml respectively). However, their NEM levels were high (6.523 and 13.187 ng/ml respectively). Although these results are very preliminary, and a much larger number of patients needs to be evaluated, the results raise a possibility that NEM may detect PC earlier than PSA (perhaps in cases of #1 and #2) or may detect indolent PC (in the case of #7 and #10).
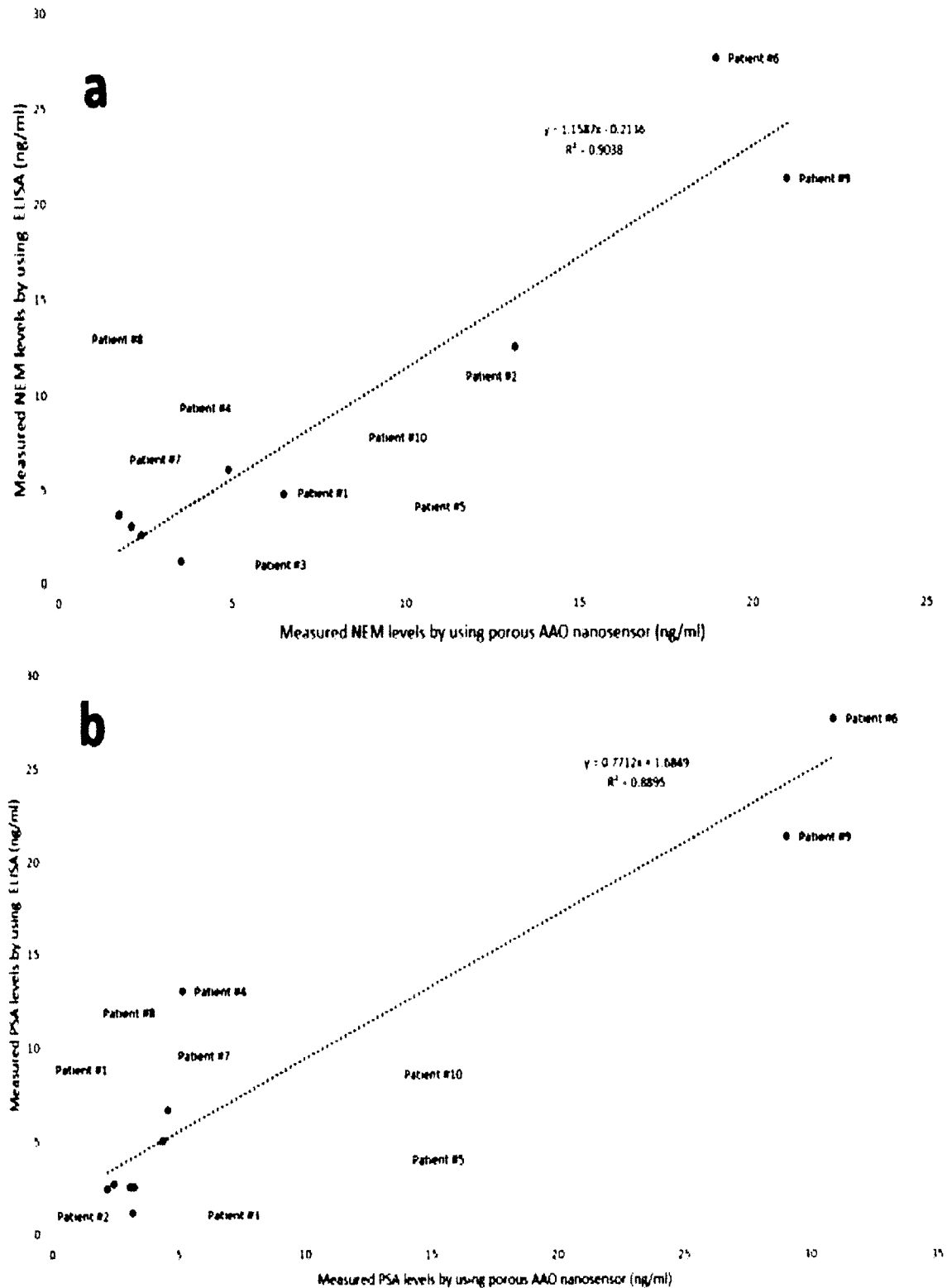
Figure 4-14. Comparison between porous AAO nanosensor and ELISA assay; (a) linear
regression curve between porous AAO nanosensor vs. ELISA for NEM (Pearson
Coefficient: 0.9507; P<0.0001); (b) linear regression curve between porous AAO
nanosensor vs. ELISA for PSA (Pearson Coefficient: 0.9431; P<0. 0001).

Table 4-3. NEM and PSA levels in 10 different human serum samples measured by using porous AAO sensor and ELISA.

Patient number	PSA level by using AAO nanopore sensor	ELISA PSA level	NEM level by using AAO nanopore sensor	ELISA NEM level
1	2.46	2.73	6.52	4.73
2	2.2	2.47	13.19	12.47
3	3.21	1.15	3.54	1.15
4	5.18	13.03	4.91	6.03
5	3.28	2.57	2.39	2.57
6	31	27.6	19	27.6
7	4.59	6.66	1.76	3.66
8	3.1	2.57	1.74	3.57
9	29.13	21.3	21.03	21.3
10	4.39	5.05	2.1	3.05
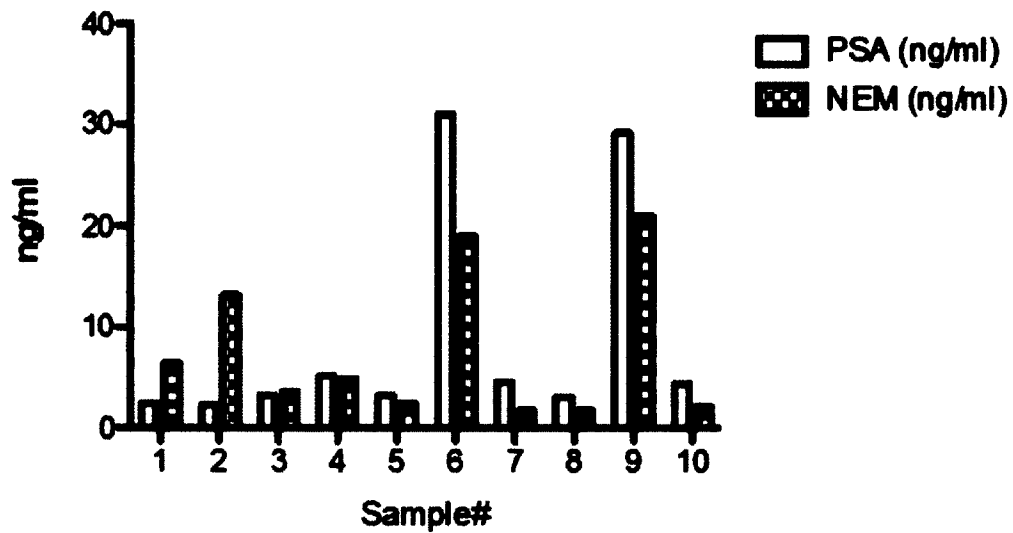
Figure 4-15. Analysis of NEM and PSA in serum samples of 10 urology patients as given in Table 4-3: Correlation between NEM and PSA in same samples (Pearson Co-efficient $r=0.8557$; $p<0.0016$).

4.2.10 PC Detection Validation with Clinicopathological PC
         Confirmed Human Serum Samples

After assay validation, we analyzed the levels of NEM and PSA of 28 blood

samples of humans who were confirmed to have the PC. The protocol for the use and

analysis of the sera was approved by the Institutional Review Boards (IRB) at University

of Louisiana at Monroe (ULM).

More importantly, all test results with PSA serum levels < 10 ng/ml are

considered as a failed to detect, and all samples with NEM serum levels < 4 ng/ml are

considered as a failed to detect as well. Any sample with serum levels more than 10

ng/ml for PSA or 4 ng/ml for NEM is considered as a pass to detect (Table 4-5) and we

generated a dot plot of tested PC serum samples (by using NEM and PSA biomarkers)

with negative controls, listed in Table 4-4 (Figure 4-16). The dot plot shows that when

we used NEM as the tested biomarker, the overlap between negative controls NEM and

PC NEM serum levels was small. On the other hand, PSA shows higher overlap with

negative controls. ROC curves (Figure 4-17) also showed that NEM is more sensitive

than PSA as PC biomarkers.

The combined use of NEM as PC biomarker led to detection of 23 out of 28 PC

cases, a success rate of 82%. On the other hand, by testing samples with PSA as PC

biomarker, we were able to detect 19 out of 28 PC cases with a success rate of 68%.

Interestingly, three samples (4, 7, and 23) showed low NEM serum levels, but

high PSA serum levels, and seven samples (9, 12, 13, 16, 17, 19, and 22) showed low

PSA serum levels with high NEM serum levels. Only two samples (3, 15) gave low

serum level readings. If we combined PSA test with NEM test, we were able to detect 26

out of 28 PC cases (93% success).

Table 4-4. Negative controls PSA and NEM levels measured by porous AAO nanosensor.

Negative control number	NEM levels	PSA levels
1	2.418	2.270
2	1.73	2.553
3	0.999	0.822
4	13.877	1.627
5	1.217	2.656
6	1.762	5.221
7	0.874	1.612
8	2.404	2.242
9	2.762	1.998
10	1.527	5.976
11	1.709	4.958
12	2.873	1.889
13	3.817	1.288
14	2.345	1.671
15	2.822	1.301
16	2.341	1.801
17	2.512	13.576
18	1.557	14.877
19	0.98	16.289
20	1.288	14.751
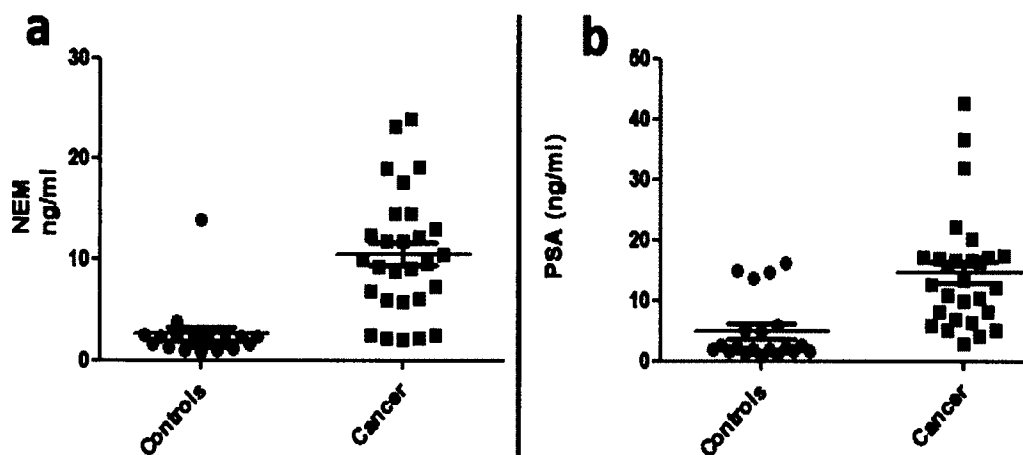
Figure 4-16. Dot plot for cancer and negative controls. (a) NEM showed little overlap between PC samples and negative controls. (b) The overlap between PC samples and the negative control is higher when samples were tested by using PSA as a biomarker.
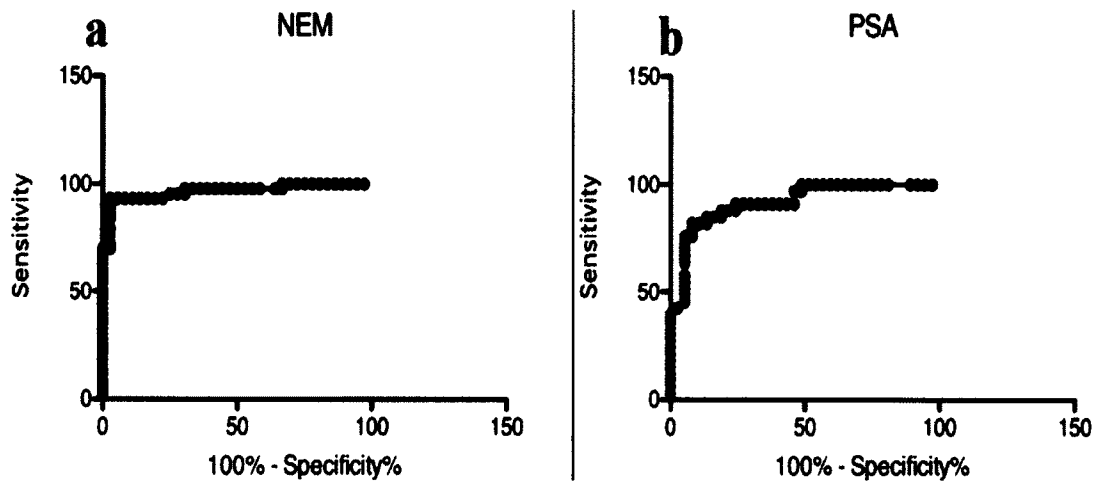
Figure 4-17. ROC curves for NEM and PSA. (a) NEM ROC curve shows that NEM biomarker is a specific and sensitive as PC biomarker. (b) PSA ROC curve shows that PSA is less specific than NEM as PC biomarker.

Table 4-5. NEM and PSA levels in PC samples tested by using porous AAO nanosensor.

PC patient number	NEM levels by using Nanosensor (ng/ml)	NEM Nanosensor test result	PSA levels by using Nanosensor (ng/ml)	PSA Nanosensor test result
1	18.967	Pass	17.053	Pass
2	5.758	Pass	10.541	Pass
3	2.129	Failed	6.310	Failed
4	2.082	Failed	17.278	Pass
5	8.755	Pass	32.548	Pass
6	9.315	Pass	22.113	Pass
7	2.449	Failed	42.770	Pass
8	10.04	Pass	10.855	Pass
9	12.461	Pass	8.247	Failed
10	7.231	Pass	12.686	Pass
11	23.926	Pass	16.771	Pass
12	14.570	Pass	6.962	Failed
13	5.982	Pass	8.115	Failed
14	17.604	Pass	10.009	Pass
15	1.432	Failed	5.061	Failed
16	6.044	Pass	3.013	Failed
17	11.738	Pass	4.249	Failed
18	11.786	Pass	16.990	Pass
19	9.612	Pass	5.953	Failed
20	12.313	Pass	12.065	Pass
21	14.495	Pass	16.398	Pass
22	10.434	Pass	5.198	Failed
23	2.245	Failed	36.750	Pass
24	6.865	Pass	15.752	Pass
25	9.087	Pass	16.586	Pass
26	23.212	Pass	17.488	Pass
27	19.205	Pass	20.252	Pass
28	13.061	Pass	13.417	Pass

4.3 Discussion

Present results demonstrate that the porous AAO nanosensor can reliably detect prostate cancer biomarkers in ultra low volume of serum samples. The nanosensor offers several advantages over the traditional ELISAs. First, the nanosensor displayed low detection limits (2 pg/ml for NEM and 20 pg/ml for PSA) and the detection range for both markers (for NEM the range is from 2 pg/ml to 0.512 ng/ml, for PSA the range is from 20 pg/ml to 1ng/ml) was 50-100-fold lower than that achieved by traditional ELISAs (μM to nM range) (see Figure 4-12). We could have achieved even higher sensitivity. Since we could detect both NEM and PSA biomarkers even in non-cancer individuals in as little as 0.25 μl of serum, we felt that achieving higher sensitivity will not provide any real benefits. The second major advantage is the technology to measure antibody-bound protein by optical interference signals coupled with localized surface plasmon resonance. This method completely eliminates the need for an enzyme-labeled antigen, or the requirement for efficient competition between labeled antigen and native molecules.

We had serious difficulties in labeling NEM peptide with an enzyme conjugate that was a thousand times larger than the NEM peptide. The labeled NEM was highly unstable, denatured rapidly, and had difficulty competing with the native protein for antibody binding sites, leading to unacceptably high non-specific binding. In addition, the technology offers several advantages, such as simplicity of the procedure, a significant reduction in the number of processing steps, and completion of the assay in the short time of fewer than two hours.

For any new detection technique, it is critical to demonstrate that the technology measures the native molecules accurately, specifically, and precisely in a complex mixture of potentially interfering proteins normally found in biological fluids. We have tested the accuracy of nanosensors in multiple ways. First, we examined whether high protein concentrations found in biological fluids such as serum would interfere with the measurement of biomarkers. We found that high levels of albumin did not interfere with biomarker measurements.

Also, we observed that the dilution curve of the serum reached the saturation point at 4 μl serum volume (see Figure 4-13). Next, we added known concentrations of biomarkers in a serum sample, and tested whether the sensor can measure the added biomarker accurately. Again, the results show we could recover 76.7% to 93% of added antigens in a serum sample at multiple concentrations (see Table 4-2). We measured PSA and NEM levels in ten patient samples of PC and benign urological diseases by the nanosensor as well as the ELISA. The results showed that by both methods were similar (Figure 4-14).

Next, we examined the correlation between NEM with PSA in same samples. In eight out of ten specimens (except #1 and #2, which exhibited a significant diversion), we observed high correlation between PSA and NEM (Pearson Coefficient 0.987; p<0.0001). We also observed divergence between NEM and PSA in some samples. For example, Patients #1 and #2 displayed normal levels of PSA but elevated NEM levels. Since the number of cases examined is extremely low and we do not have access to the current status of the patients, we cannot say whether NEM can detect PCs with low PSA levels. However, it is a possibility since it is known that PCs with high neuroendocrine

differentiation or metastatic PC generally display low PSA but are aggressive [160, 161].

On the other hand, patients #7 and #10 showed borderline PSA levels (4.6 and 4.4 ng/ml

respectively) but low NEM levels (1.76 and 2.1 ng/ml respectively).

Finally, we compared the serum PSA and NEM levels of the patients with their

clinical diagnosis based on physical examination and pathology (Table 4-5). As expected,

confirmed PC patients displayed high levels of both markers. Based on these

observations, it appears that the nanosensor is reliable, accurate and precise in typical

analytical conditions for clinical measurements.

Since PSA is known to overestimate the number of PC patients, these results

raise a possibility that one can be more certain of cancer diagnosis when both PSA and

NEM are elevated, rather than an increase in only one biomarker. This can significantly

reduce the number of false positive diagnoses and, consequently, the number of biopsies

[158, 159]. Indeed, the present study is preliminary and is designed to test the validity of

an immuno-nanosensor for the measurement of PC biomarkers. Moreover, the current

cohort of patients is extremely small and is not sufficient to draw any clinical

conclusions. However, these preliminary results provide a strong rationale for further

investigation of PSA/NEM in a larger patient cohort with well-defined statistical

objectives.

Although these studies are preliminary, they demonstrate that this novel device,

which is fabricated by a low-cost standard micro- and nano-fabrication process [162], can

be a viable prototype for future prostate cancer diagnostics in the clinic. The device's low

cost, suitability of mass production, and long shelf life can contribute to significant

acceptability in a marketplace. Thus, considering the ease of fabrication, utilization of

commonly available commercial components (the typical life time of the white lamp is 10000 hours), and the simplicity and sensitivity of the method make this system accessible to virtually any biomedical laboratory at a small cost. The fabricated sensor is disposable and we can fabricate more sensors when we need more.

To summarize: a novel, low-cost nanosensor has been optimized for the detection of two biomarker proteins (NEM and PSA) for prostate cancer. The study presents the preliminary proof of principle for the reliable platform for developing clinically useful protein detection devices that could, in the future, be translated to point-of-care in prostate cancer diagnostics and therapeutics.

CHAPTER 5

CONCLUSIONS AND FUTURE WORK

5.1 Conclusions

In this dissertation, we tested different PC biomarkers (PSA and NEM) in buffer as well as in human serum by using optical label-free biosensor based on anodic aluminum oxide (AAO) nanopore thin film. Label-free biosensors provide less cost and didn't affect the properties of the analyte. It is a minimally invasive method and it has no connection to any external compound, like fluorescent dye.

The operating principle of our porous AAO label-free biosensor is biased on detecting the phase difference that applied to the reflected light from the sensor surface due to the change of the refractive index caused by the presence of an analyte over the sensor surface.

Porous AAO nanosensor was fabricated by using a two-step anodization method. By using this method, we can control AAO pore geometry by changing anodization time and anodization voltage. For example, pore diameter is directly proportional to anodization voltage. Also, pore geometry affects the number of reflected fringes and fringe intensity.

Coating porous AAO nanosensor surface with gold enhanced the the fringe shape as well as the reflected signal intensity. Also, a gold coated nanosensor was able to make

extraordinary contact with alkanethiols, which are the building blocks of the self-assembled monolayer.

In this project we used porous AAO nanosensor with the following characteristics: Pore diameter D_p = 55 nm, pore length l_p = 5 μm, pore density = 5.5 * 10^9 pores per cm^2, pore period = 145 nm, poricity = 34.4%, and Au coat thickness = 5 nm.

Optimizing antibody experiments were performed before we start generating biomarkers standerd curves. It is important to find the appropriate antibody concentration and to keep it constant for all experiments.

After that, we generated standered curves for NEM and PSA, and we found the upper and lower concentrations, detection limits for these proteins (for NEM the range is from 2pg/ml to 0.512 ng/ml, for PSA the range is from 20 pg/ml to 1ng/ml). Accuracy is an important factor in this project; a porous AAO nanosensor was highly accurate and detected small changes in tested samples (as low as 1pg).

Specificity experiments were performed before we started measuring biomarker levels in human samples. We found that porous AAO nanosensor is highly specific and can detect only antigens that are specific to antibody. Then we measured the lowest and highest voulumes of human blood serum that porous AAO nanosensor can measure; this nanosensor can measure the levels of PC biomarker even in very low serum volume (0.25μl).

Then we measured the levels of PC markers (NEM and PSA) in healthy, as well as PC, patients and we compared the nanopore sensor results with ELISA; the results showed high correlation between serum NEM and PSA values determined by the sensor and those by the ELISA.

Finally, we tested the levels of PC NEM and PSA markers in pathologically confirmed PC patients serum. NEM detected PC in 82% of PC tested samples and PSA detected 68% of PC tested samples. The results were promising and gave us an indication to improve the ability to detect PC by combining NEM with PSA test (PC detection rate of 93%).

5.2   Future Work

We describe the addition of a microchannel system that can be applied to AAO patterns (Figure 5-1). The major challenge in using a microchannel system for biomolecule detection is the need for multiple fluid inlets and outlets to make sure the different solutions do not overlap and react.

Figure 5-1. Microchannel system fabricated over 15 AAO patterns.

The process of adding a microchannel system involves two parts: fabrication of the PDMS microfluidic chip and the chip assembly.

The PDMS fabrication process uses a soft lithography [163]. The fabrication process (Figure 5-2) starts by spinning the SU8 coat onto a silicon wafer with a diameter of 10 mm. The thickness of the SU8 mold will generate a cavity between the PDMS and AAO sensor patterns.

Then, we will apply a mask over the SU8 mold, and we will expose UV light to

transfer the patterns. Then we coat the mold with PDMS. After coating, the sample is

heated at 65⊡ for 90 minutes. After this, we will disconnect the PDMS layer from its

mold. Finally, the inlet and outlet spaces will be created using a 1.5 mm diameter hole

puncher.
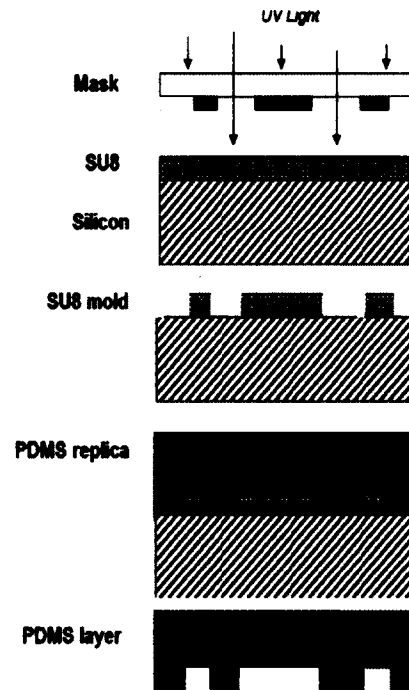
Figure 5-2. PDMS microchannel system fabrication process.

After the fabrication is completed, we will attach the resulted PDMS layer to the

patterned AAO sensor to assemble the final product (Figure 5-3). PDMS layer thickness

should be optimized, since layer thickness affects Fabry-perot fringe shape (Figure 5-4).

Figure 5-3. Cross sectional view of the PDMS microchannel attached to gold coated (Au)
AAO nanopore thin film [38].
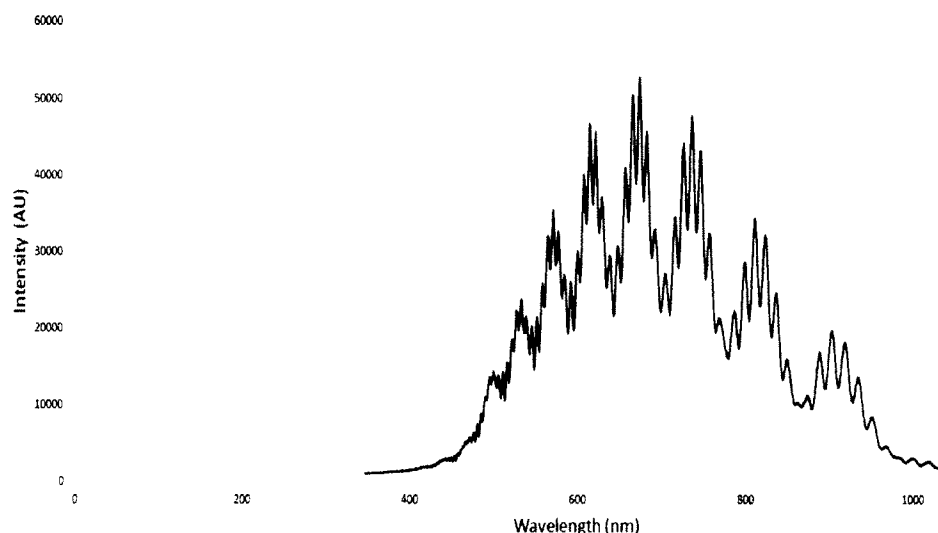
Figure 5-4. Not optimized PDMS layer thickness, which affects Fabry-perot fringes shape.

By adding microchannel system, the sensor can be developed as a smart PC

detection system (Figure 5-5). To develop that device, disposable cartridge-type sensor,

optical detection, electronics for wireless transmission, and control panel, a liquid-crystal

display is needed.
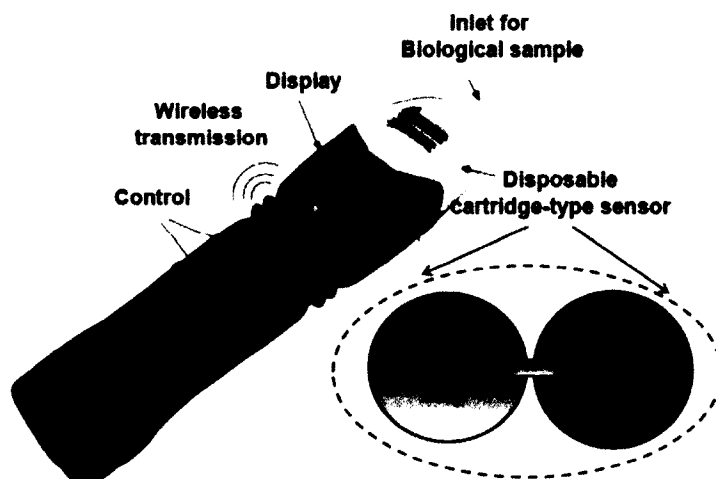
Figure 5-5. Schematic of smart PC detection system with main components: disposable cartridge-type sensor that consists of two parts; sample preparation chip and detection chip, wireless communication interface to transmit patient measurement data to a clinic, measurement system and display, control panel for all the components & functions.

The disposable cartridge-type sensor consists of two connected chips. One chip at the upstream is for biological/medical sample preparation, the other at the downstream is for PC screening and monitoring. Biomarker standard curve will be used as positive control.

The white light source is collimated by a lens and perpendicularly illuminates on the disposable cartridge-type sensor. A white light source, a microfluidic control network, a liquid-crystal display (LCD) and wireless transmission will be connected to and operated by a microcontroller. The battery-operated microcontroller is a one-chip unit, which includes CPU (central process unit), RAM, analog to digital (A/D) and digital to analog (D/A) converter, and interrupt controller.

The reflected signal will appear on the LCD display. Three LED lights (red, yellow, and green) will give us an indication if we have to increase or decrease the applied white light intensity to make sure that the reflected signal doesn't reach the saturation level. The red LED light is going to be an indication for high intensity reflected signal, while the yellow light will show that the reflected signal intensity is low; the green light will be a mark for a suitable intensity reflected signal. The intensity of the reflected signal will be controlled by increasing and decreasing the integration time by using the side buttons.

APPENDIX

CROSS-CORRELATION MATLAB CODE

```
uiopen('file location\file name.file type',1)

x1=VarName1(1:2048);

x2=VarName4(1:2048);

y1=VarName2(1:2048);

y2=VarName5(1:2048);

[c,j]=xcorr(y1,y2);

plot(x1,y1);

hold on; plot(x2,y2,'r');hold off

l=(length(xcorr(y1,y2))-1)/2;

figure;plot(-l:l,c,'.-');

[p,i]=findpeaks(c,'SORTSTR','descend'); % sorting peaks in descending order

pk_idx=j(i(1)); % Peak Index

shift=pk_idx*(max(x1)-min(x1))/2048;
```

The University of Louisiana at Monroe
Institutional Review Board
Notice of Determination for Projects using Human Subjects

Protocol ID#:   344 -2012

Principal Investigator: Girish Shah

Collaborator(s):

Project Title: Calcitonin in Prostate Growth and Neoplasia

Date Approved: 12/9/2011

Expiration Date:

☑ 1) In accordance with the ULM Policy for the Protection of Human Subjects, the ULM Institutional Review Board reviewed and APPROVED this project on the above date. Note: The project is subject to continuing review and any conditions listed in the comments section below.

    ☐ a. This project has received FULL COMMITTEE REVIEW.

    ☑ b. This project has received EXPEDITED REVIEW.

    ☑ c. This project is exempt based on the following part and sections(s) of the ULM Policy for the Protection of Human Subjects:

☐ 2) In accordance with the ULM Policy for the Protection of Human Subjects, the ULM Institutional Review Board reviewed this project and have determined that this project does not meet IRB standards and is therefore DEFICIENT for the reasons listed in the comments section below.

Exempt because: Exempt based on section III.B.5 of the ULM IRB Handbook.

Comment: This project's "APPROVED" start date is determined according to the date listed above in this notification. Any research conducted, prior to this date, must cease and all data collected destroyed.

Thank you for your submission. Please contact the Office of Sponsored Programs and Research if you require any further assistance.

Connie Smith

Connie Smith, Pharm. D.
Interim Chair, ULM's IRB

cc: PI's Department Head
    IRB protocol file

Wednesday, December 14, 2011

REFERENCES

[1]   J. D. Enderle and J. D. Bronzino, *Introduction To Biomedical Engineering*: Academic press, 2012.

[2]   T. Vo-Dinh and B. Cullum, "Biosensors and biochips: advances in biological and medical diagnostics," *Fresenius' Journal of Analytical Chemistry,* vol. 366, pp. 540-551, 2000.

[3]   W. Morris, *American Heritage Dictionary Of The English Language*: American heritage, 1969.

[4]   M. Mascini and S. Tombelli, "Biosensors for biomarkers in medical diagnostics," *Biomarkers,* vol. 13, pp. 637-657, 2008.

[5]   C. Yao, T. Zhu, Y. Qi, Y. Zhao, H. Xia, and W. Fu, "Development of a quartz crystal microbalance biosensor with aptamers as bio-recognition element," *Sensors,* vol. 10, pp. 5859-5871, 2010.

[6]   N. G. Durmuş, R. L. Lin, M. Kozberg, D. Dermici, A. Khademhosseini, and U. Demirci, "Acoustic-Based biosensors," in *Encyclopedia Of Microfluidics And Nanofluidics,* ed: Springer, 2015, pp. 28-40.

[7]   S. Nie and S. R. Emory, "Probing single molecules and single nanoparticles by surface-enhanced Raman scattering," *Science,* vol. 275, pp. 1102-1106, 1997.

[8]   R. S. Gaster, D. A. Hall, C. H. Nielsen, S. J. Osterfeld, H. Yu, K. E. Mach, et al., "Matrix-insensitive protein assays push the limits of biosensors in medicine," *Nature Medicine,* vol. 15, pp. 1327-1332, 2009.

[9]   M. S. Wilson and W. Nie, "Multiplex measurement of seven tumor markers using an electrochemical protein chip," *Analytical Chemistry,* vol. 78, pp. 6476-6483, 2006.

[10]   N. Sinha, J. Ma, and J. T. Yeow, "Carbon nanotube-based sensors," *Journal Of Nanoscience and Nanotechnology,* vol. 6, pp. 573-590, 2006.

[11]   P. Malik, V. Katyal, V. Malik, A. Asatkar, G. Inwati, and T. K. Mukherjee, "Nanobiosensors: concepts and variations," *ISRN Nanomaterials,* vol. 2013, 2013.

[12]   C. L. Haynes, A. D. McFarland, and R. P. V. Duyne, "Surface-enhanced Raman spectroscopy," *Analytical Chemistry,* vol. 77, pp. 338 A-346 A, 2005.

[13]   H. Mukundan, H. Xie, A. S. Anderson, W. K. Grace, J. E. Shively, and B. I. Swanson, "Optimizing a waveguide-based sandwich immunoassay for tumor biomarkers: evaluating fluorescent labels and functional surfaces," *Bioconjugate Chemistry,* vol. 20, pp. 222-230, 2009.

[14]   V. Espina, E. C. Woodhouse, J. Wulfkuhle, H. D. Asmussen, E. F. Petricoin, and L. A. Liotta, "Protein microarray detection strategies: focus on direct detection technologies," *Journal Of Immunological Methods,* vol. 290, pp. 121-133, 2004.

[15]   P. S. Cremer, "Label-free detection becomes crystal clear," *Nature Biotechnology,* vol. 22, pp. 172-173, 2004.

[16]   Y.-H. Yun, E. Eteshola, A. Bhattacharya, Z. Dong, J.-S. Shim, L. Conforti, et al., "Tiny medicine: nanomaterial-based biosensors," *Sensors,* vol. 9, pp. 9275-9299, 2009.

[17]   M. Iqbal, M. A. Gleeson, B. Spaugh, F. Tybor, W. G. Gunn, M. Hochberg, et al., "Label-free biosensor arrays based on silicon ring resonators and high-speed optical scanning instrumentation," *Selected Topics in Quantum Electronics, IEEE Journal,* vol. 16, pp. 654-661, 2010.

[18]   C. Huh, B. K. Kim, W. J. Kim, J. C. Hong, and G. Y. Sung, "Label-free biosensor," ed: Google Patents, 2011.

[19]   K. De Vos, I. Bartolozzi, E. Schacht, P. Bienstman, and R. Baets, "Silicon-on-Insulator microring resonator for sensitive and label-free biosensing," *Optics Express,* vol. 15, pp. 7610-7615, 2007.

[20]   G. Zheng, F. Patolsky, Y. Cui, W. U. Wang, and C. M. Lieber, "Multiplexed electrical detection of cancer markers with nanowire sensor arrays," *Nature Biotechnology,* vol. 23, pp. 1294-1301, 2005.

[21]   B. D. Malhotra and A. Chaubey, "Biosensors for clinical diagnostics industry," *Sensors and Actuators B: Chemical,* vol. 91, pp. 117-127, 2003.

[22]   R. L. Millen, *Giant magnetoresistive sensors and magnetic labels for chip-scale detection of immunosorbent assays*: ProQuest, 2005.

[23]   T. Zhang, *A nanostructured Fabry-Perot interferometer for label-free biodetection*: LOUISIANA TECH UNIVERSITY, 2012.

[24]   K. Maehashi and K. Matsumoto, "Label-free electrical detection using carbon nanotube-based biosensors," *Sensors,* vol. 9, pp. 5368-5378, 2009.

[25]   C. Boero, J. Olivo, G. De Micheli, and S. Carrara, "New approaches for carbon nanotubes-based biosensors and their application to cell culture monitoring," *Biomedical Circuits and Systems, IEEE Transactions,* vol. 6, pp. 479-485, 2012.

[26]   J. Wang, "Carbon-nanotube based electrochemical biosensors: A review," *Electroanalysis,* vol. 17, pp. 7-14, 2005.

[27]   J. Arlett, E. Myers, and M. Roukes, "Comparative advantages of mechanical biosensors," *Nature Nanotechnology,* vol. 6, pp. 203-215, 2011.

[28]   V. S.-Y. Lin, K. Motesharei, K.-P. S. Dancil, M. J. Sailor, and M. R. Ghadiri, "A porous silicon-based optical interferometric biosensor," *Science,* vol. 278, pp. 840-843, 1997.

[29]   S. Pan and L. J. Rothberg, "Interferometric sensing of biomolecular binding using nanoporous aluminum oxide templates," *Nano letters,* vol. 3, pp. 811-814, 2003.

[30]   D. Ahuja and D. Parande, "Optical sensors and their applications," *Journal of Scientific Research and Reviews,* vol. 1, pp. 60-68, 2012.

[31]   K. Fidanboylu and H. Efendioglu, "Fiber optic sensors and their applications," in *5th International Advanced Technologies Symposium (IATS'09),* 2009.

[32]   J. Canning, "Optical sensing: the last frontier for enabling intelligence in our wired up world and beyond," *Photonic Sensors,* vol. 2, pp. 193-202, 2012.

[33]   M. A. Cooper, "Optical biosensors in drug discovery," *Nature Reviews Drug Discovery,* vol. 1, pp. 515-528, 2002.

[34]   S. V. Pham, M. Dijkstra, A. J. Hollink, R. M. de Ridder, M. Pollnau, and H. J. Hoekstra, "Compact integrated optical sensors based on a Si3N4 grated waveguide optical cavity," in *The European Conference on Lasers and Electro-Optics,* 2011.

[35]   K. Betzler, "Fabry-perot interferometer," *KB20020122, Universitat Osnabruck, Fachbereich Physik,* 2002.

[36]   P. J. Ko, R. Ishikawa, T. Takamura, H. Sohn, and A. Sandhu, "Porous silicon based protocol for the rapid and real-time monitoring of biorecognition between human IgG and protein A using functionalized superparamagnetic beads," *Magnetics, IEEE Transactions,* vol. 48, pp. 2846-2849, 2012.

[37]   C. Pacholski, M. Sartor, M. J. Sailor, F. Cunin, and G. M. Miskelly, "Biosensing using porous silicon double-layer interferometers: reflective interferometric Fourier transform spectroscopy," *Journal of the American Chemical Society*, vol. 127, pp. 11636-11645, 2005.

[38]   T. Zhang, Z. Gong, R. Giorno, and L. Que, "A nanostructured Fabry-Perot interferometer," *Optics Express*, vol. 18, pp. 20282-20288, 2010.

[39]   T. Zhang, S. Karandikar, Z. Gong, R. Giorno, and L. Que, "Label-free biosensing using a nanostructured Fabry-Perot interferometer," in *Sensors, 2010 IEEE*, pp. 2065-2068.

[40]   M. K. Brawer, "Prostate-specific antigen: Current status," *CA: A Cancer Journal for Clinicians*, vol. 49, pp. 264-281, 1999.

[41]   R. L. Siegel, K. D. Miller, and A. Jemal, "Cancer statistics, 2015," *CA: A Cancer Journal for Clinicians*, vol. 65, pp. 5-29, 2015.

[42]   F. H. Schröder and M. J. Roobol, "Defining the optimal prostate-specific antigen threshold for the diagnosis of prostate cancer," *Current Opinion in Urology*, vol. 19, pp. 227-231, 2009.

[43]   S. W. Marcella, G. G. Rhoads, J. L. Carson, F. Merlino, and H. Wilcox, "Prostate-specific antigen screening and mortality from prostate cancer," *Journal of General Internal Medicine*, vol. 23, pp. 248-253, 2008.

[44]   T. Pickles, "Current status of PSA screening. Early detection of prostate cancer," *Canadian Family Physician*, vol. 50, pp. 57-63, 2004.

[45]   D. A. Lacher and T. D. Thompson, "Total, free, and percent free prostate-specific antigen levels among US men, 2001–04," *Population*, vol. 3, p. 5, 2006.

[46]   W. Sakr, G. Haas, B. Cassin, J. Pontes, and J. Crissman, "The frequency of carcinoma and intraepithelial neoplasia of the prostate in young male patients," *The Journal of Urology*, vol. 150, pp. 379-385, 1993.

[47]   C. C. Society, N. C. I. o. C. A. C. o. Records, and Registries, *Canadian Cancer Statistics*: Canadian Cancer Society, 1987.

[48]   H. B. Carter, C. H. Morrell, J. D. Pearson, L. J. Brant, C. C. Plato, E. J. Metter, et al., "Estimation of prostatic growth using serial prostate-specific antigen measurements in men with and without prostate disease," *Cancer Research*, vol. 52, pp. 3323-3328, 1992.

[49]   D. V. Makarov, S. Loeb, R. H. Getzenberg, and A. W. Partin, "Biomarkers for prostate cancer," *Annual Review of Medicine*, vol. 60, pp. 139-151, 2009.

[50]   C. R. Pound, A. W. Partin, M. A. Eisenberger, D. W. Chan, J. D. Pearson, and P. C. Walsh, "Natural history of progression after PSA elevation following radical prostatectomy," *Jama*, vol. 281, pp. 1591-1597, 1999.

[51]   S. J. Freedland, E. B. Humphreys, L. A. Mangold, M. Eisenberger, F. J. Dorey, P. C. Walsh, *et al.*, "Risk of prostate cancer–specific mortality following biochemical recurrence after radical prostatectomy," *Jama*, vol. 294, pp. 433-439, 2005.

[52]   D. V. Makarov, E. B. Humphreys, L. A. Mangold, M. A. Carducci, A. W. Partin, M. A. Eisenberger, *et al.*, "The natural history of men treated with deferred androgen deprivation therapy in whom metastatic prostate cancer developed following radical prostatectomy," *The Journal of Urology*, vol. 179, pp. 156-162, 2008.

[53]   U.-H. Stenman, J. Leinonen, H. Alfthan, S. Rannikko, K. Tuhkanen, and O. Alfthan, "A complex between prostate-specific antigen and α1-antichymotrypsin is the major form of prostate-specific antigen in serum of patients with prostatic cancer: assay of the complex improves clinical sensitivity for cancer," *Cancer Research*, vol. 51, pp. 222-226, 1991.

[54]   A. Christensson, T. Björk, O. Nilsson, U. Dahlén, M. Matikainen, A. Cockett, et al., "Serum prostate specific antigen complexed to alpha 1-antichymotrypsin as an indicator of prostate cancer," *The Journal of Urology*, vol. 150, pp. 100-105, 1993.

[55]   A. A. Luderer, Y.-T. Chen, T. F. Soriano, W. J. Kramp, G. Carlson, C. Cuny, et al., "Measurement of the proportion of free to total prostate-specific antigen improves diagnostic performance of prostate-specific antigen in the diagnostic gray zone of total prostate-specific antigen," *Urology*, vol. 46, pp. 187-194, 1995.

[56]   W. J. Catalona, A. W. Partin, K. M. Slawin, M. K. Brawer, R. C. Flanigan, A. Patel, et al., "Use of the percentage of free prostate-specific antigen to enhance differentiation of prostate cancer from benign prostatic disease: a prospective multicenter clinical trial," *Jama*, vol. 279, pp. 1542-1547, 1998.

[57]   M. K. Brawer, G. E. Meyer, J. L. Letran, D. D. Bankson, D. L. Morris, K. K. Yeung, et al., "Measurement of complexed PSA improves specificity for early detection of prostate cancer," *Urology*, vol. 52, pp. 372-378, 1998.

[58]   S. Sharma, "Tumor markers in clinical practice: General principles and guidelines," *Indian Journal of Medical and Paediatric Oncology*, vol. 30, p. 1, 2009.

[59]   G. Shah, "Polypeptide of given sequence that is a biochemical marker for prostate cancer conjugated to an antibody or fragment thereof; treating prostate cancer," U.S. Patent No. 7,026,454. 11 Apr. 2006.

[60]   G. Shah, "Human cancer cell specific gene transcript," U.S. Patent No. 7,713,693. 11 May 2010.

[61]   J. Chien, Y. Ren, Y. Q. Wang, W. Bordelon, E. Thompson, R. Davis, et al., "Calcitonin is a prostate epithelium-derived growth stimulatory peptide," *Molecular and Cellular Endocrinology*, vol. 181, pp. 69-79, 2001.

[62]   A. Panoskaltsis-Mortari and R. Bucy, "In situ hybridization with digoxigenin-labeled RNA probes: facts and artifacts," *Biotechniques*, vol. 18, pp. 300-307, 1995.

[63]   D.-V. Matei, G. Renne, M. Pimentel, M. T. Sandri, L. Zorzino, E. Botteri, *et al.*, "Neuroendocrine differentiation in castration-resistant prostate cancer: a systematic diagnostic attempt," *Clinical Genitourinary Cancer*, vol. 10, pp. 164-173, 2012.

[64]   M. Tarle, B. Spajić, I. Kraljić, and Z. Kusić, "Continuous finasteride therapy for benign prostate hypertrophy upgrades both neuroendorcine differentiation and aggressive prostate cancer," *Anticancer Research*, vol. 29, pp. 1797-1801, 2009.

[65]   S. Alzghoul, M. Hailat, S. Zivanovic, L. Que, and G. V. Shah, "Measurement of serum prostate cancer markers using a nanopore thin film based optofluidic chip," *Biosensors and Bioelectronics*, vol. 77, pp. 491-498, 2016.

[66]   Y. Liang, D. P. Ankerst, N. S. Ketchum, B. Ercole, G. Shah, J. D. Shaughnessy, et al., "Prospective evaluation of operating characteristics of prostate cancer detection biomarkers," *The Journal of Urology*, vol. 185, pp. 104-110, 2011.

[67]   H. Uetsuki, H. Tsunemori, R. Taoka, R. Haba, M. Ishikawa, and Y. Kakehi, "Expression of a novel biomarker, EPCA, in adenocarcinomas and precancerous lesions in the prostate," *The Journal of Urology*, vol. 174, pp. 514-518, 2005.

[68]   E. S. Leman, G. W. Cannon, B. J. Trock, L. J. Sokoll, D. W. Chan, L. Mangold, et al., "RETRACTED: EPCA-2: A highly specific serum marker for prostate cancer," *Urology*, vol. 69, pp. 714-720, 2007.

[69]   J. S. Horoszewicz, E. Kawinski, and G. Murphy, "Monoclonal antibodies to a new antigenic marker in epithelial prostatic cells and serum of prostatic cancer patients," *Anticancer Research*, vol. 7, pp. 927-935, 1986.

[70]   W.-H. Lee, R. A. Morton, J. I. Epstein, J. D. Brooks, P. A. Campbell, G. S. Bova, et al., "Cytidine methylation of regulatory sequences near the pi-class glutathione S-transferase gene accompanies human prostatic carcinogenesis," *Proceedings of the National Academy of Sciences,* vol. 91, pp. 11733-11737, 1994.

[71]   T. Zhang, Y. He, J. Wei, and L. Que, "Nanostructured optical microchips for cancer biomarker detection," *Biosensors and Bioelectronics,* vol. 38, pp. 382-388, 2012.

[72]   T. Kumeria and D. Losic, "Controlling interferometric properties of nanoporous anodic aluminium oxide," *Nanoscale Research Letters,* vol. 7, pp. 1-10, 2012.

[73]   G. Wang and Y. Lin, "A 3-dimensional nanobiosensor based on an anodic aluminum oxide template," *Une,* vol. 13, pp. 15, 2016.

[74]   J.-J. Tsai, I. Bau, H.-T. Chen, Y.-T. Lin, and G.-J. Wang, "A novel nanostructured biosensor for the detection of the dust mite antigen Der p2," *International Journal of Nanomedicine,* vol. 6, pp. 1201-1208, 2011.

[75]   T. Kumeria, L. Parkinson, and D. Losic, "A nanoporous interferometric micro-sensor for biomedical detection of volatile sulphur compounds," *Nanoscale Research Letters,* vol. 6, pp. 1-7, 2011.

[76]   J. C. Love, L. A. Estroff, J. K. Kriebel, R. G. Nuzzo, and G. M. Whitesides, "Self-assembled monolayers of thiolates on metals as a form of nanotechnology," *Chemical Reviews,* vol. 105, pp. 1103-1170, 2005.

[77]   K. A. Peterlinz and R. Georgiadis, "*In situ* kinetics of self-assembly by surface plasmon resonance spectroscopy," *Langmuir,* vol. 12, pp. 4731-4740, 1996.

[78]   J. Kim, "Investigations of Thiolated Self-Assembled Monolayers on Gold Substrates by FTIR with Specular Reflectance," *PIKE Technologies Application Note,* 2007, www.piketech.com.

[79]   R. Dulbecco and M. Vogt, "Plaque formation and isolation of pure lines with poliomyelitis viruses," *The Journal of Experimental Medicine,* vol. 99, pp. 167-182, 1954.

[80]   J. Noujaim, R. L. Andreatti Filho, E. Lima, A. S. Okamoto, R. L. Amorim, and R. T. Neto, "Detection of T lymphocytes in intestine of broiler chicks treated with Lactobacillus spp. and challenged with Salmonella enterica serovar Enteritidis," *Poultry science,* vol. 87, pp. 927-933, 2008.

[81]   S. Alzghoul, M. Hailat, S. Zivanovic, G. V. Shah, and L. Que, "Detection of neuroendocrine marker in blood samples using an optofluidic chip," in *Solid-State Sensors, Actuators and Microsystems (TRANSDUCERS), 2015 Transducers-2015 18th International Conference on*, 2015, pp. 1703-1706.

[82]   S. K. Vashist, "Comparison of 1-ethyl-3-(3-dimethylaminopropyl) carbodiimide based strategies to crosslink antibodies on amine-functionalized platforms for immunodiagnostic applications," *Diagnostics,* vol. 2, pp. 23-33, 2012.

[83]   A. Johansson, G. Blagoi, and A. Boisen, "Polymeric cantilever-based biosensors with integrated readout," *Applied Physics Letters,* vol. 89, p. 173505, 2006.

[84]   J. Greener, W. Li, J. Ren, D. Voicu, V. Pakharenko, T. Tang, et al., "Rapid, cost-efficient fabrication of microfluidic reactors in thermoplastic polymers by combining photolithography and hot embossing," *Lab on a Chip,* vol. 10, pp. 522-524, 2010.

[85]   A. del Campo and C. Greiner, "SU-8: a photoresist for high-aspect-ratio and 3D submicron lithography," *Journal of Micromechanics and Microengineering,* vol. 17, p. R81, 2007.

[86]   J. Liu, B. Cai, J. Zhu, G. Ding, X. Zhao, C. Yang, et al., "Process research of high aspect ratio microstructure using SU-8 resist," *Microsystem Technologies,* vol. 10, pp. 265-268, 2004.

[87]   I. Wong and C.-M. Ho, "Surface molecular property modifications for poly (dimethylsiloxane)(PDMS) based microfluidic devices," *Microfluidics and Nanofluidics,* vol. 7, pp. 291-306, 2009.

[88]   D. Fuard, T. Tzvetkova-Chevolleau, S. Decossas, P. Tracqui, and P. Schiavone, "Optimization of poly-di-methyl-siloxane (PDMS) substrates for studying cellular adhesion and motility," *Microelectronic Engineering,* vol. 85, pp. 1289-1293, 2008.

[89]   B. Wang, J. H. Horton, and R. D. Oleschuk, "Sulfonated-polydimethylsiloxane (PDMS) microdevices with enhanced electroosmotic pumping and stability," *Canadian Journal of Chemistry,* vol. 84, pp. 720-729, 2006.

[90]   S. K. Sia and G. M. Whitesides, "Microfluidic devices fabricated in poly (dimethylsiloxane) for biological studies," *Electrophoresis,* vol. 24, pp. 3563-3576, 2003.

[91]   A. Mata, A. J. Fleischman, and S. Roy, "Characterization of polydimethylsiloxane (PDMS) properties for biomedical micro/nanosystems," *Biomedical Microdevices,* vol. 7, pp. 281-293, 2005.

[92] M. Kučera and J. Lanikova, "Thermal stability of polydimethylsiloxane. II. Formation of stable complexes on basic active centers," *Journal of Polymer Science,* vol. 59, pp. 79-85, 1962.

[93] C. Peucheret, "Note on Fabry-Perot Interferometers," Technical University of Denmark, May 2004.

[94] N. R. Frómeta, "Cantilever biosensors," *Biotecnología Aplicada,* vol. 23, pp. 320-323, 2006.

[95] J. Han, "Fabry–Perot cavity chemical sensors by silicon micromachining techniques," *Applied Physics Letters,* vol. 74, pp. 445-447, 1999.

[96] L. Que, "Two-dimensional tunable filter array for a matrix of integrated fiber optic input-output light channels," ed: Google Patents, 2002.

[97] N.-S. Eum, S.-H. Yeom, D.-H. Kwon, H.-R. Kim, and S.-W. Kang, "Enhancement of sensitivity using gold nanorods—Antibody conjugator for detection of E. coli O157: H7," *Sensors and Actuators B: Chemical,* vol. 143, pp. 784-788, 2010.

[98] T. Dohi, K. Matsumoto, and I. Shimoyama, "The micro Fabry-Perot interferometer for the spectral endoscope," in *Micro Electro Mechanical Systems, 2005, 18th IEEE International Conference,* pp. 830-833, 2005.

[99] V. V. Doan and M. J. Sailor, "Luminescent color image generation on porous silicon," *Science,* vol. 256, pp. 1791-1792, 1992.

[100] C. L. Curtis, V. V. Doan, G. M. Credo, and M. J. Sailor, "Observation of optical cavity modes in photoluminescent porous silicon films," *Journal of the Electrochemical Society,* vol. 140, pp. 3492-3494, 1993.

[101] G. Hodes, *Electrochemistry of nanomaterials*: John Wiley & Sons, 2008.

[102] D. Brodoceanu, R. Elnathan, B. Prieto-Simón, B. Delalat, T. Guinan, E. Kroner, *et al.*, "Dense arrays of uniform submicron pores in silicon and their applications," *ACS Applied Materials and Interfaces,* vol. 7, pp. 1160-1169, 2015.

[103] M. J. Sailor and J. R. Link, ""Smart dust": nanostructured devices in a grain of sand," *Chemical Communications,* vol.11, pp. 1375-1383, 2005.

[104] M. Y. Chen and M. J. Sailor, "Charge-gated transport of proteins in nanostructured optical films of mesoporous silica," *Analytical Chemistry,* vol. 83, pp. 7186-7193, 2011.

[105] K.-P. S. Dancil, D. P. Greiner, and M. J. Sailor, "A porous silicon optical biosensor: detection of reversible binding of IgG to a protein A-modified surface," *Journal of the American Chemical Society,* vol. 121, pp. 7925-7930, 1999.

[106] J.-S. Lee, S.-W. Kim, E.-Y. Jang, B.-H. Kang, S.-W. Lee, G. Sai-Anand, et al., "Rapid and sensitive detection of lung cancer biomarker using nanoporous biosensor based on localized surface plasmon resonance coupled with interferometry," *Journal of Nanomaterials,* vol. 2015, pp. 1-11, 2015.

[107] B. Rossi, "Optics Addison-Wesley," *Reading, MA,* pp. 21, 1957.

[108] D. Losic and A. Santos, *Nanoporous Alumina: Fabrication, Structure, Properties and Applications:* vol. 219, Springer, 2015.

[109] V. D. Bruggeman, "Berechnung verschiedener physikalischer Konstanten von heterogenen Substanzen. I. Dielektrizitätskonstanten und Leitfähigkeiten der Mischkörper aus isotropen Substanzen," *Annalen Der Physik,* vol. 416, pp. 636-664, 1935.

[110] S.-H. Yeom, O.-G. Kim, B.-H. Kang, K.-J. Kim, H. Yuan, D.-H. Kwon, et al., "Highly sensitive nano-porous lattice biosensor based on localized surface plasmon resonance and interference," *Optics Express,* vol. 19, pp. 22882-22891, 2011.

[111] J. Ferré-Borrull, J. Pallarès, G. Macías, and L. F. Marsal, "Nanostructural engineering of nanoporous anodic alumina for biosensing applications," *Materials,* vol. 7, pp. 5225-5253, 2014.

[112] K. Hotta, A. Yamaguchi, and N. Teramae, "Deposition of polyelectrolyte multilayer film on a nanoporous alumina membrane for stable label-free optical biosensing," *The Journal of Physical Chemistry C,* vol. 116, pp. 23533-23539, 2012.

[113] K. Hotta, A. Yamaguchi, and N. Teramae, "Nanoporous waveguide sensor with optimized nanoarchitectures for highly sensitive label-free biosensing," *ACS Nano,* vol. 6, pp. 1541-1547, 2012.

[114] K. H. A. Lau, L.-S. Tan, K. Tamada, M. S. Sander, and W. Knoll, "Highly sensitive detection of processes occurring inside nanoporous anodic alumina templates: A waveguide optical study," *The Journal of Physical Chemistry B,* vol. 108, pp. 10812-10818, 2004.

[115]   A. Santos, V. S. Balderrama, M. Alba, P. Formentín, J. Ferré-Borrull, J. Pallarès, et al., "Tunable Fabry-Pérot interferometer based on nanoporous anodic alumina for optical biosensing purposes," *Nanoscale Research Letters,* vol. 7, pp. 1-4, 2012.

[116]   S. D. Alvarez, C.-P. Li, C. E. Chiang, I. K. Schuller, and M. J. Sailor, "A label-free porous alumina interferometric immunosensor," *ACS Nano,* vol. 3, pp. 3301-3307, 2009.

[117]   A. Santos, G. Macías, J. Ferré-Borrull, J. Pallarès, and L. F. Marsal, "Photoluminescent enzymatic sensor based on nanoporous anodic alumina," *ACS Applied Materials & Interfaces,* vol. 4, pp. 3584-3588, 2012.

[118]   K. D. Elgert, *Immunology: understanding the immune system:* John Wiley & Sons, 2009.

[119]   M. Strandh, *Insights into weak affinity antibody-antigen interactions Studies using affinity chromatography and optical biosensor:* Lund University, 2000.

[120]   R. Reverberi and L. Reverberi, "Factors affecting the antigen-antibody reaction," *Blood Transfusion,* vol. 5, pp. 227-240, 2007.

[121]   J. Devore, *Probability and Statistics for Engineering and the Sciences:* Cengage Learning, 2015.

[122]   O. Shultheiss and S. Stanton, "Assessment of salivary hormones. Methods in Social Neuroscience. Harmon-Jones, E., Beer, JS, Eds," *Guilford Press,* pp. 17-44, New York, 2009.

[123]   M. Lohrengel, "Thin anodic oxide layers on aluminium and other valve metals: high field regime," *Materials Science and Engineering: R: Reports,* vol. 11, pp. 243-294, 1993.

[124]   J. W. Diggle, T. C. Downie, and C. Goulding, "Anodic oxide films on aluminum," *Chemical Reviews,* vol. 69, pp. 365-405, 1969.

[125]   F. Keller, M. Hunter, and D. Robinson, "Structural features of oxide coatings on aluminum," *Journal of the Electrochemical Society,* vol. 100, pp. 411-419, 1953.

[126]   G. Thompson, "Porous anodic alumina: fabrication, characterization and applications," *Thin Solid Films,* vol. 297, pp. 192-201, 1997.

[127]   G. Thompson and G. Wood, "Porous anodic film formation on aluminium", *Nature* (London), vol. 290, pp. 230-232, 1981.

[128] A. Güntherschulze and H. Betz, "Die Bewegung der Ionengitter von Isolatoren bei extremen elektrischen Feldstärken," *Zeitschrift für Physik,* vol. 92, pp. 367-374, 1934.

[129] W. Lee and S.-J. Park, "Porous anodic aluminum oxide: anodization and templated synthesis of functional nanostructures," *Chemical Reviews,* vol. 114, pp. 7487-7556, 2014.

[130] V. Parkhutik and V. Shershulsky, "Theoretical modelling of porous oxide growth on aluminium," *Journal of Physics D: Applied Physics,* vol. 25, p. 1258, 1992.

[131] K. Shimizu, K. Kobayashi, G. Thompson, and G. Wood, "Development of porous anodic films on aluminium," *Philosophical Magazine A,* vol. 66, pp. 643-652, 1992.

[132] G. Thompson, Y. Xu, P. Skeldon, K. Shimizu, S. Han, and G. Wood, "Anodic oxidation of aluminium," *Philosophical Magazine B,* vol. 55, pp. 651-667, 1987.

[133] A. Li, F. Müller, A. Birner, K. Nielsch, and U. Gösele, "Hexagonal pore arrays with a 50–420 nm interpore distance formed by self-organization in anodic alumina," *Journal of Applied Physics,* vol. 84, pp. 6023-6026, 1998.

[134] W. Lee, R. Ji, U. Gösele, and K. Nielsch, "Fast fabrication of long-range ordered porous alumina membranes by hard anodization," *Nature Materials,* vol. 5, pp. 741-747, 2006.

[135] O. Jessensky, F. Müller, and U. Gösele, "Self-organized formation of hexagonal pore arrays in anodic alumina," *Applied Physics Letters,* vol. 72, pp. 1173-1175, 1998.

[136] D. Losic, L. Velleman, K. Kant, T. Kumeria, K. Gulati, J. G. Shapter, et al., "Self-ordering electrochemistry: a simple approach for engineering nanopore and nanotube arrays for emerging applications," *Australian Journal of Chemistry,* vol. 64, pp. 294-301, 2011.

[137] R. Dronov, A. Jane, J. G. Shapter, A. Hodges, and N. H. Voelcker, "Nanoporous alumina-based interferometric transducers ennobled," *Nanoscale,* vol. 3, pp. 3109-3114, 2011.

[138] T. T. Ehler, N. Malmberg, and L. J. Noe, "Characterization of self-assembled alkanethiol monolayers on silver and gold using surface plasmon spectroscopy," *The Journal of Physical Chemistry B,* vol. 101, pp. 1268-1272, 1997.

[139] S. Driver and D. Woodruff, "Adsorption structures of 1-octanethiol on Cu (111) studied by scanning tunneling microscopy," *Langmuir,* vol. 16, pp. 6693-6700, 2000.

[140] H. Rieley, G. Kendall, A. Chan, R. Jones, J. Lu, D. Woodruff, et al., "Surface adsorption structures in 1-octanethiol self-assembled on Cu (111)," *Surface Science,* vol. 392, pp. 143-152, 1997.

[141] C. Yan, A. Gölzhäuser, M. Grunze, and C. Wöll, "Formation of alkanethiolate self-assembled monolayers on oxidized gold surfaces," *Langmuir,* vol. 15, pp. 2414-2419, 1999.

[142] P. Kamat and D. Meisel, "Semiconductor Nanoclusters-Physical, Chemical, and Catalytic Aspects," *Studies in Surface Science and Catalysis,* Elsevier, 1997.

[143] T. Nakanishi, B. Ohtani, and K. Uosaki, "Fabrication and characterization of CdS-nanoparticle mono-and multilayers on a self-assembled monolayer of alkanedithiols on gold," *The Journal of Physical Chemistry B,* vol. 102, pp. 1571-1577, 1998.

[144] Y. He, X. Li, and L. Que, "Fabrication and characterization of lithographically patterned and optically transparent anodic aluminum oxide (AAO) nanostructure thin film," *Journal of Nanoscience and Nanotechnology,* vol. 12, pp. 7915-7921, 2012.

[145] H. Yin, X. Li, and L. Que, "Fabrication and characterization of aluminum oxide thin film micropatterns on the glass substrate," *Microelectronic Engineering,* vol. 128, pp. 66-70, 2014.

[146] X. Li, Y. He, and L. Que, "Fluorescence detection and imaging of biomolecules using the micropatterned nanostructured aluminum oxide," *Langmuir,* vol. 29, pp. 2439-2445, 2013.

[147] A. Santos, T. Kumeria, and D. Losic, "Nanoporous anodic alumina: a versatile platform for optical biosensors," *Materials,* vol. 7, pp. 4297-4320, 2014.

[148] T. Cass, Ligler, F, *Immobilized biomolecules in analysis: A practical Approach.* UK: Oxford University Press, 1998.

[149] H. Rodriguez, Z. Tezak, M. Mesri, S. A. Carr, D. C. Liebler, S. J. Fisher, et al., "Analytical validation of protein-based multiplex assays: a workshop report by the NCI-FDA interagency oncology task force on molecular diagnostics," *Clin Chem,* vol. 56, pp. 237-243, Feb 2010.

[150] WHO, "Validation of analytical assays," WHO, Geneva,1997.

[151] G. Shah, A. Srivastava, and K. Iczkowski, "Neuroendocrine marker: a novel, reliable early stage marker for prostate cancer," in *100th AACR Annual Meeting,* Abstract number 4826, Denver, CO, 2009.

[152] I. M. Shui, S. Lindstrom, A. S. Kibel, S. I. Berndt, D. Campa, T. Gerke, *et al.*, "Prostate cancer (PCa) risk variants and risk of fatal PCa in the National Cancer Institute Breast and Prostate Cancer Cohort Consortium," *Eur Urol,* vol. 65, pp. 1069-1075, Jun 2014.

[153] E. Francini, R. Petrioli, G. Rossi, L. Laera, and G. Roviello, "PSA response rate as a surrogate marker for median overall survival in docetaxel-based first-line treatments for patients with metastatic castration-resistant prostate cancer: an analysis of 22 trials," *Tumour Biol,* vol. 35, pp. 10601-10607, Nov 2014.

[154] F. H. Schroder and M. J. Roobol, "Defining the optimal prostate-specific antigen threshold for the diagnosis of prostate cancer," *Curr Opin Urol,* vol. 19, pp. 227-231, May 2009.

[155] J. Cuzick, M. A. Thorat, G. Andriole, O. W. Brawley, P. H. Brown, Z. Culig, *et al.*, "Prevention and early detection of prostate cancer," *Lancet Oncol,* vol. 15, pp. e484-92, Oct 2014.

[156] C. H. Bangma, M. Bul, T. H. van der Kwast, T. Pickles, I. J. Korfage, C. M. Hoeks, et al., "Active surveillance for low-risk prostate cancer," *Crit Rev Oncol Hematol,* vol. 85, pp. 295-302, Mar 2013.

[157] Y. Kitagawa, S. Ueno, K. Izumi, Y. Kadono, H. Konaka, A. Mizokami, et al., "Cumulative probability of prostate cancer detection in biopsy according to free/total PSA ratio in men with total PSA levels of 2.1-10.0 ng/ml at population screening," *J Cancer Res Clin Oncol,* vol. 140, pp. 53-59, Jan 2014.

[158] L. P. Bokhorst, C. H. Bangma, G. J. van Leenders, J. J. Lous, S. M. Moss, F. H. Schroder, et al., "Prostate-specific antigen-based prostate cancer screening: reduction of prostate cancer mortality after correction for non attendance and contamination in the rotterdam section of the european randomized study of screening for prostate cancer," *Eur Urol,* vol. 65, pp. 329-336, Aug 11 2013.

[159] A. J. Vickers, A. M. Cronin, G. Aus, C. G. Pihl, C. Becker, K. Pettersson, et al., "Impact of recent screening on predicting the outcome of prostate cancer biopsy in men with elevated prostate-specific antigen: data from the European Randomized Study of Prostate Cancer Screening in Gothenburg, Sweden," *Cancer,* vol. 116, pp. 2612-20, Jun 1 2010.

[160] D. K. Lee, J. H. Park, J. H. Kim, S. J. Lee, M. K. Jo, M. C. Gil, et al., "Progression of prostate cancer despite an extremely low serum level of prostate-specific antigen," *Korean J. Urol.,* vol. 51, pp. 358-61, May 2010.

[161] C. Trotz, "Prostate cancer with a normal PSA: small cell carcinoma of the prostate--a rare entity," *J. Am. Board. Fam. Pract.,* vol. 16, pp. 343-4, Jul-Aug 2003.

[162] H. Yin, A. Mu, Y. Sun, G. Yan, H. Wei, C. Ma, et al., "Preparation and evaluation of multifunctional envelope-type nano device loading siRNA," *Artif. Cells Nanomed. Biotechnol.,*vol. 44, pp. 1-7, May 16 2014.

[163] Y. Xia and G. M. Whitesides, "Soft lithography," *Annual Review of Materials Science*, vol. 28, pp. 153-184, 1998.

[164] Cartun, Richard W., and Carl A. Pedersen. "An immunocytochemical technique offering increased sensitivity and lowered cost with a streptavidin-horseradish peroxidase conjugate." *Journal of Histotechnology*, vol. 4, pp. 273-277, 1989.